FISKEN OG HAVET

nr. 7/2007

Ecological consequences of exploration drilling on coral reefs in the Træna Deep

Økologiske konsekvenser av leteboring på korallrev

Pål B. Mortensen and Aivo Lepland

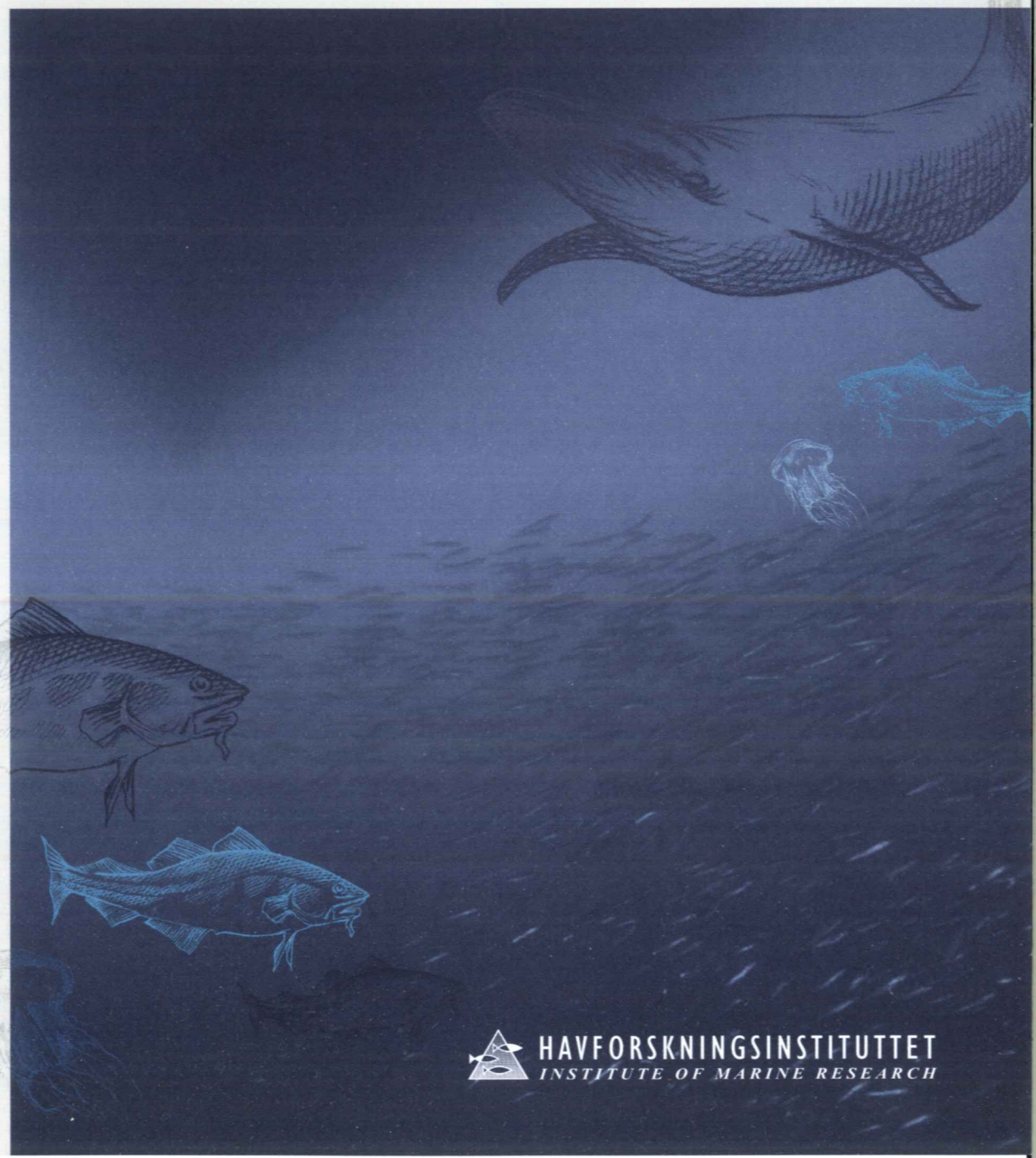

HAVFORSKNINGSINSTITUTTET
INSTITUTE OF MARINE RESEARCH

Ecological consequences of exploration drilling on coral reefs in the Træna Deep

Pål B. Mortensen[1] and Aivo Lepland[2]
[1] **Havforskningsinstituttet,** [2] **Norges geologiske undersøkelse**

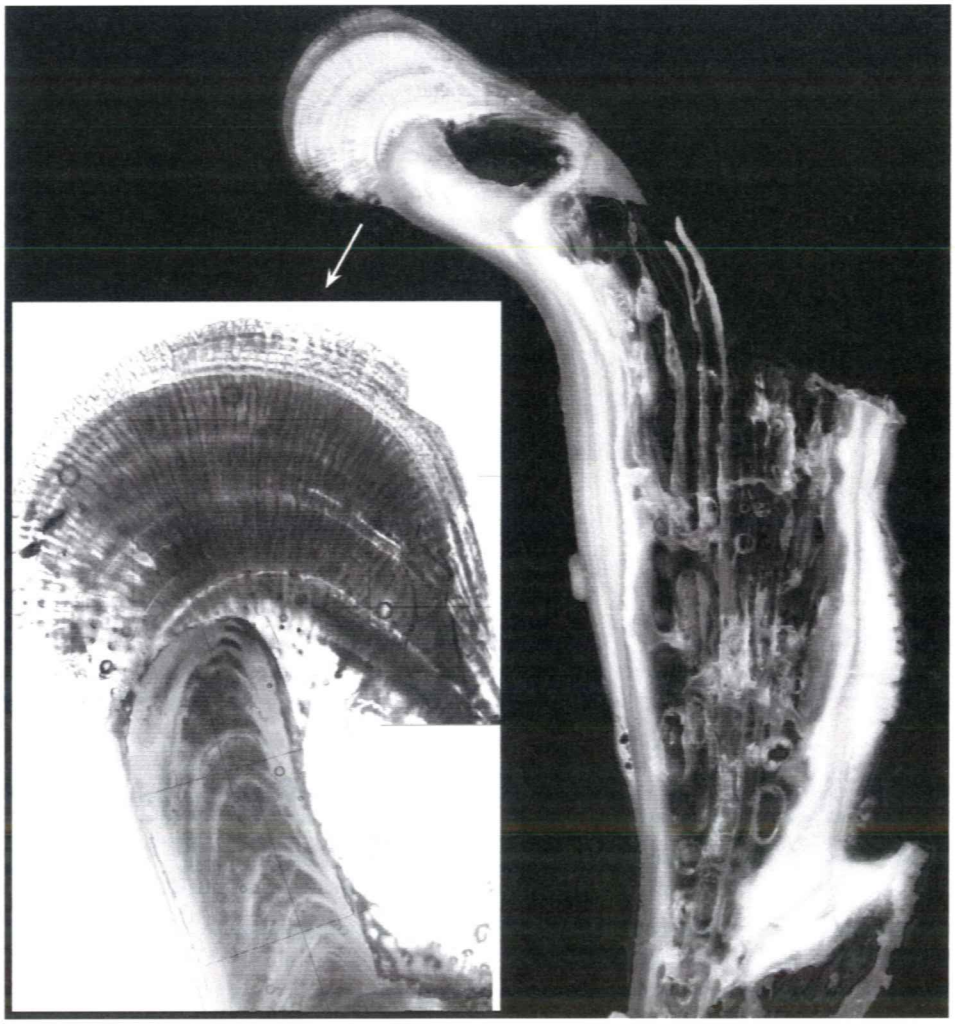

NGU
Norges geologiske undersøkelse

HAVFORSKNINGSINSTITUTTET
INSTITUTE OF MARINE RESEARCH

PROSJEKTRAPPORT

HAVFORSKNINGSINSTITUTTET
INSTITUTE OF MARINE RESEARCH

Nordnesgaten 50, Postboks 1870 Nordnes, 5817 BERGEN
Tlf. 55 23 85 00, Faks 55 23 85 31, www.imr.no

Tromsø 9294 TROMSØ | **Flødevigen** 4817 HIS | **Austevoll** 5392 STOREBØ | **Matre** 5984 MATREDAL

Distribusjon: Åpen

Prosjektnr.: 11229

Oppdragsgiver(e): Norsk Hydro, Eni Norge, Statoil

Oppdragsgivers referanse:

Rapport: Fisken og Havet | **Nr. - År** 7-2007

Dato: 11. februar 2008

Program: Mareano

Faggruppe: Bunnhabitater og skalldyr

Antall sider totalt:

Tittel (norsk/engelsk):
Økologiske konsekvenser av leteboring på korallrev

Ecological consequences of exploration drilling on coral reefs

Forfatter(e):
Pål B. Mortensen og Aivo Lepland

Sammendrag (norsk):

Denne rapporten presenterer resultater fra en undersøkelse av korallrev (*Lophelia pertusa*), korallskjelletter og bunnsedimenter i nærheten av en letebrønn i Trænadypet. Målet for undersøkelsen var å vurdere "helsetilstanden" til *Lophelia*-rev og de økologiske effektene av boreaktiviteter. Feltarbeidet ble utført i juni 2005, med innsamling av skjellett- og sedimentprøver fra 33 lokaliteter, videoopptak fra åtte dykk med fjernstyrt miniubåt (ROV), samt strømmålinger nær bunnen på tre lokaliteter.

Strømhastighet og -retning ble målt over en periode på seks døgn. Hastigheten varierte mellom 0 og 27 cm/s, med svakest strøm nær borestedet, og sterkest på referanselokaliteten 12 km sydøst for borestedet. Strømmønsteret var tydelig tidevannsinfluert med en sterk vestlig komponent. Dette mønsteret ble også gjenspeilet hos korallrevene og sjøtrærne (*Paragorgia arborea*) med en tydelig østlig vokseretning.

Analyser av videoopptak avdekket ingen klare forskjeller i "helstilstanden" til korallrev som vokste oppstrøms eller nedstrøms for borestedet. Revene besto typisk av en levende frontsone mot strømmen, og en "hale" med døde skjelletter som strekte seg opp til 150 m i strømretningen. Analyser av tynnslip fra skjellettene viste at det var mulig å etablere en tidsserie med årringer tilbake til tidspunktet da leteboringen fant sted. De harde sedimentene i området muliggjorde kun prøvetaking av korte sedimentkjerner (5 – 30 cm), men flere av kjerneprøvene inneholdt forhøyede konsentrasjoner av Barium/baritt i sedimentoverflaten, eller rett under. Den geografiske fordelingen av Barium i sedimen-tene indikerte en spredningen av boreslam mot vest fra borestedet, i samsvar med hovedstrømretningen i området. Barittkrystaller fra boreslammet ble også identifisert i sedimenter fanget i hulrom i døde korallpolypper som var eldre enn seks år. Den høyeste konsentrasjonen ble funnet i en død polypp som var eldre enn 13 år.

Forekomst av relativt grovkornete sedimenter og komponenter fra boreslam i korallpolyppene ca 600 m nedstrøms fra borestedet indikerer turbulens og sediment-tilførsel i løpet av boreperioden. Sedimenttilførselen har sannsynligvis hatt en negativ effekt på korallrevene, men på grunn av kort varighet av boreperioden og sterke strømmer som har fortynnet partikkelkonsentrasjonen fra de episodiske boreslam-utslippene har effektene fått et begrenset omfang. Resultatene indikerer små

skader på kaldtvannkorallen *Lophelia pertusa* som følge av spredning av boreslam, men viser også klart at metoden som er utviklet her kan brukes til å spore eksponering av forhøyede partikkelkonsentrasjoner som følge av boreaktivitet.

Summary (English):

Coral reefs, skeleton samples and bottom sediments in the vicinity of the hydrocarbon exploration test well in the Træna Deep have been studied to assess the ecological effects and "health status" of *Lophelia* coral reefs. The fieldwork was carried out in June 2005, providing skeleton and sediment samples from 33 locations, video-records from eight dives with Remotely Operated Vehicle (ROV), and data on water movement from three current meters located at different sites.

Current velocity and direction were recorded over a period of six days. The velocity varied between 0 and 27 cm/s, with the weakest currents in the area close to the exploration drilling site, and the strongest currents at the reference site about 12 km southeast of the drilling site. The current pattern showed tidal influence with a strong westward component. This current pattern was also reflected in the eastward growth of the coral reefs and by the orientation of fan-shaped gorgonian corals facing the same direction.

The analysis of video-records did not reveal clear difference in "health" status between reefs up-current or down-current to the drilling site. The reefs consisted typically of a living "frontal" zone facing the currents, and a dead "tail" extending down-current for up to ca. 150 m. Analysis of skeleton thin sections revealed that it is possible to establish the chronology and track the years in skeletons when the exploration drilling occurred. The relatively coarse-grained sediments in the area made it possible to obtain sediment cores of limited length (5 – 30 cm), but several cores contain elevated Ba/barite concentration at the sediment surface or just below. The geographic distribution of Ba content in sediments allowed the reconstruction of drilling mud dispersal pattern westward from the drilling site, consistent with the prevailing current directions. Barite crystals, derived from the drilling mud, were identified among trapped sediments in the skeleton cavities of dead coral polyps older than six years. Highest barite concentration was found in a polyp older than 13 years.

The presence of relatively coarse-grained sediments and drilling mud components in the coral polyps ca. 600 m down current from the drilling site signals the elevated turbulence and sediment supply during the drilling activity. This elevated sediment dispersion was likely having an influence upon the coral reefs, but due to the relatively short duration of the drilling campaign and strong currents that effectively dilute episodic sediment discharges the damage was apparently not significant. Thus the results provide only minor indications of negative effects of drilling mud discharge on the cold-water coral *Lophelia pertusa*, but demonstrate that the method developed here can be used to trace exposure to elevated particle load originating from drilling activity.

Emneord (norsk):	**Subject heading (English):**
1. Kaldvannskorallrev	**1.** Coldwater coral reefs
2. Oljeboring	**2.** Oil drilling
3. Baritt	**3.** Barite

Prosjektleder

Faggruppeleder

TABLE OF CONTENT

SAMMENDRAG

Denne rapporten presenterer resultater fra en undersøkelse av korallrev (*Lophelia pertusa*), korallskjelletter og bunnsedimenter i nærheten av en letebrønn i Trænadypet. Målet for undersøkelsen var å vurdere "helsetilstanden" til *Lophelia*-rev og de økologiske effektene av boreaktiviteter. Feltarbeidet ble utført i juni 2005, med innsamling av skjellett- og sedimentprøver fra 33 lokaliteter, videoopptak fra åtte dykk med fjernstyrt miniubåt (ROV), samt strømmålinger nær bunnen på tre lokaliteter.

Strømhastighet og -retning ble målt over en periode på seks døgn. Hastigheten varierte mellom 0 og 27 cm/s, med svakest strøm nær borestedet, og sterkest på referanselokaliteten 12 km sydøst for borestedet. Strømmønsteret var tydelig tidevannsinfluert med en sterk vestlig komponent. Dette mønsteret ble også gjenspeilet hos korallrevene og sjøtrærne (*Paragorgia arborea*) med en tydelig østlig vokseretning.

Analyser av videoopptak avdekket ingen klare forskjeller i "helstilstanden" til korallrev som vokste oppstrøms eller nedstrøms for borestedet. Revene besto typisk av en levende frontsone mot strømmen, og en "hale" med døde skjelletter som strekte seg opp til 150 m i strømretningen. Analyser av tynnslip fra skjellettene viste at det var mulig å etablere en tidsserie med årringer tilbake til tidspunktet da leteboringen fant sted. De harde sedimentene i området muliggjorde kun prøvetaking av korte sedimentkjerner (5 – 30 cm), men flere av kjerneprøvene inneholdt forhøyede konsentrasjoner av Barium/baritt i sedimentoverflaten, eller rett under. Den geografiske fordelingen av Barium i sedimentene indikerte en spredningen av boreslam mot vest fra borestedet, i samsvar med hovedstrømretningen i området. Barittkrystaller fra boreslammet ble også identifisert i sedimenter fanget i hulrom i døde korallpolypper som var eldre enn seks år. Den høyeste konsentrasjonen ble funnet i en død polypp som var eldre enn 13 år.

Forekomst av relativt grovkornete sedimenter og komponenter fra boreslam i korallpolyppene ca 600 m nedstrøms fra borestedet indikerer turbulens og sedimenttilførsel i løpet av boreperioden. Sedimenttilførselen har sannsynligvis hatt en negativ effekt på korallrevene, men på grunn av kort varighet av boreperioden og sterke strømmer som har fortynnet partikkelkonsentrasjonen fra de episodiske boreslamutslippene, har effektene fått et begrenset omfang. Resultatene indikerer små skader på kaldtvannkorallen *Lophelia pertusa* som følge av spredning av boreslam, men viser også klart at metoden som er utviklet her kan brukes til å spore eksponering av forhøyede partikkelkonsentrasjoner som følge av boreaktivitet.

SUMMARY

Coral reefs, skeleton samples and bottom sediments in the vicinity of the hydrocarbon exploration test well in the Træna Deep have been studied to assess the ecological effects and "health status" of *Lophelia* coral reefs. The fieldwork was carried out in June 2005, providing skeleton and sediment samples from 33 locations, video-records from eight dives with Remotely Operated Vehicle (ROV), and data on water movement from three current meters located at different sites.

Current velocity and direction were recorded over a period of six days. The velocity varied between 0 and 27 cm/s, with the weakest currents in the area close to the exploration drilling site, and the strongest currents at the reference site about 12 km southeast of the drilling site. The current pattern showed tidal influence with a strong westward component. This current pattern was also reflected in the eastward growth of the coral reefs and by the orientation of fan-shaped gorgonian corals facing the same direction.

The analysis of video-records did not reveal clear difference in "health" status between reefs up-current or down-current to the drilling site. The reefs consisted typically of a living "frontal" zone facing the currents, and a dead "tail" extending down-current for up to ca. 150 m. Analysis of skeleton thin sections revealed that it is possible to establish the chronology and track the years in skeletons when the exploration drilling occurred. The relatively coarse-grained sediments in the area made it possible to obtain sediment cores of limited length (5 – 30 cm), but several cores contained elevated Ba/barite concentration at the sediment surface or just below. The geographic distribution of Ba content in sediments allowed the reconstruction of drilling mud dispersal pattern westward from the drilling site, consistent with the prevailing current directions. Barite crystals, derived from the drilling mud, were identified among trapped sediments in the skeleton cavities of dead coral polyps older than six years. Highest barite concentration was found in a polyp older than 13 years.

The presence of relatively coarse-grained sediments and drilling mud components in the coral polyps ca. 600 m down current from the drilling site, signals the elevated turbulence and sediment supply during the drilling activity. This elevated sediment dispersion was likely to have an influence upon the coral reefs, but due to the relatively short duration of the drilling campaign and strong currents that effectively dilute episodic sediment discharges, the damage was apparently not significant. Thus the results provide only minor indications of negative effects of drilling mud discharge on the cold-water coral *Lophelia pertusa*, but demonstrate that the method developed here can be used to trace exposure to elevated particle load originating from drilling activity.

BACKGROUND

In 1992 -1993 Statoil drilled an exploration well (6610/03-01) in the Træna Deep (Figure 1 - 3). Inspection around the drilling location prior to drilling documented that there were coral reefs on the planned drilling site. These reefs are created by the stone coral *Lophelia pertusa*. The Norwegian shelf, from western Norway to Finnmark, has the largest known concentration of such reefs, and the Træna Deep is one of the rich areas. The location of the drilling site was moved slightly to avoid negative impact on a reef. However, there are several reefs in the vicinity, at different distances to the drilling site (Figure 2). This was indicated by multibeam echosounder mapping performed by the Institute of Marine Research (IMR) in 2003. These multibeam results and analysis of the backscatter data served as a guide to plan the sampling locations for the fieldwork of this study.

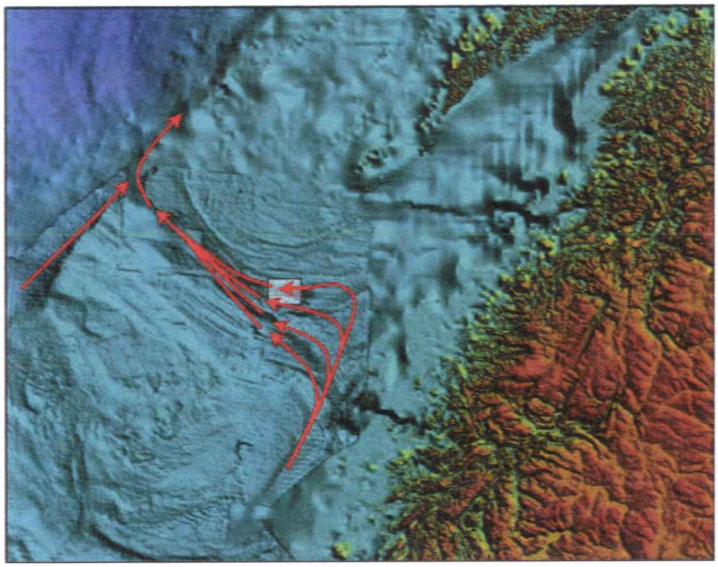

Figure 1. Shaded relief bathymetry map of the Vesterålen-Trænabanken area showing the study area as a grey box. The red arrows indicate the general surface current patterns in the area after Poulain et al. (1996).

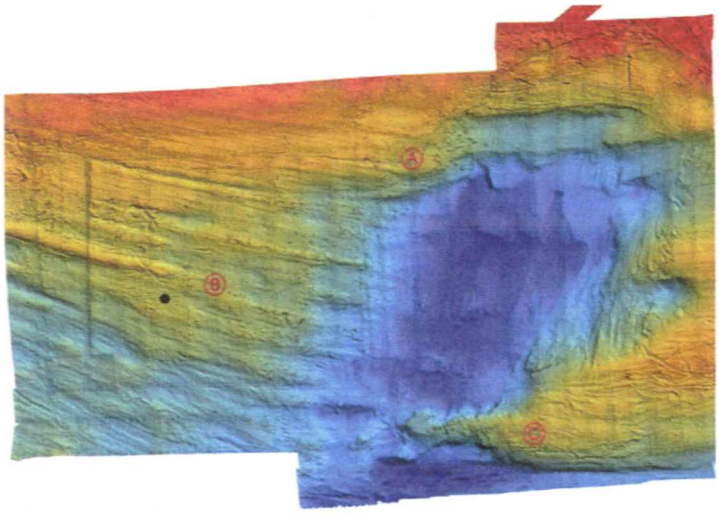

Figure 2. Shaded relief bathymetry map of the Træna Deep area. The deepest (blue) parts are around 400 m deep while the shallowest (red) parts are around 270 m deep. Location of current meters are indicated with letters. The drilling location is shown with a black dot.

The well was drilled during two periods: 24 Oct 1992 – 18 Feb 1993 and 10 Sep – 12 Dec 1993. The well was 3808 m deep (below seabed surface). In total 436 m^3 drilling cutting was deposited to the seabed surface. Barite (2300 t), bentonite (80 t) and gypsum (70 t) were added to the drilling fluid as shale-stabilizers. These are relatively large quantities, which,

according to Statoil were caused by disconnections due to rough weather conditions. The disconnections resulted in increased discharges.

Suspension feeding animals such as corals may be susceptible to increased concentration of inedible particles in the water. *Lophelia pertusa* build long-lived, delicate structures, which also need long time to recover after damage. Therefore, this species has been given special attention regarding needs for protection. The occurrence of reefs at different distances from the well, both up current and down current, provides a perfect setting for studying possible impacts from the drilling activity. This study includes a retrospective analysis of incorporation of impurities in the coral skeleton that can indicate exposure to drilling mud and associated elements.

Skeleton growth lines have been documented to be formed at an annual basis (Mortensen and Rapp 1998). Trace element variations in skeletons of tropical scleractinians (stone corals) have been used as indicators for changes in water quality caused by the production of oil and gas: barium (Trefty et al. 1981; Deslarzes et al. 1995), vanadium (Guzman and Jarvis 1996), hydrocarbons and sterols (Law et al. 1994), and terpenoids (Readman et al. 1996). In the study reported here we focused on the distribution of drilling discharged barite both in skeletons and sediments.

The closest coral reef is located about 200 m to the west of the drilling site (Figure 2 and 3), and the bathymetric data indicated the presence of 21 reefs within a radius of 1.5 km. However, as demonstrated by earlier interpretations of sidescan sonar data (FUGRO, Geoteam), and by the visual inspections in this study, this turns out to be a conservative estimate. The reefs in the area are unusual compared to other reefs in Norway by their elongated shape and alignment parallel to the prevailing near-bottom currents. To test the hypothesis of the current control upon the elongated shape of reefs, and to obtain a better picture of the direction and velocity of bottom currents, three current meters were deployed at different localities around the drilling site.

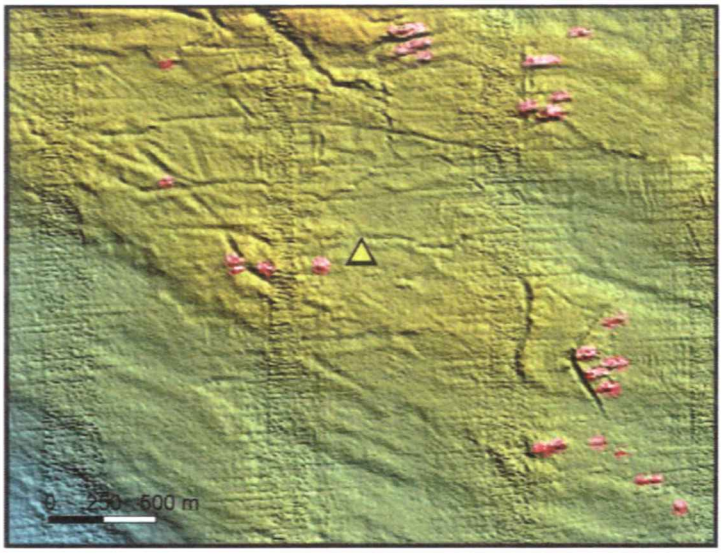

Figure 3. Coral reefs (highlighted in red) close to the drilling site in the Træna Deep, interpreted from multibeam bathymetry.

The goal of this study was to increase the knowledge that is required as a basis for management decisions concerning petroleum exploration in deep-water coral reef areas. We aimed at finding how far from a drilling site potential negative impacts can be traced on the coral reefs. For this purpose, we have analysed coral health status from video records, composition of selected chemical components in the coral skeleton, and the distribution of chemical indicators in the sediments.

The fieldwork was undertaken 18-24 June 2005, as a part of cruise number 2005108 with R/V G.O. Sars, providing bottom samples from 33 locations, video-records from eight ROV dives, and current data from three locations.

MATERIAL AND METHODS

Field methods

Video inspections

The seabed was inspected along the route of eight dives (Figure 7 and 8) using the ROV Aglantha. This ROV has a depth rating of 2000 m, and is equipped with manipiulator and sampling basket. Its position was recorded using Simrad MPT324 transponder used with the ship's Hipap 500 system. The video-records were analysed with respect to composition of different bottom types (soft bottom, pebble, cobble, and boulder) and percentage cover of live corals, dead corals, and coral rubble (coral rubble is defined as small fragments of dead corals, most commonly surrounding the *Lophelia* reefs). The video-records were divided into sequences of 1 min (corresponding to around 10 m, depending on the speed of the ROV).

Current patterns

Three current meters (Aanderaa RCM-7) were deployed at three different sites within the study area (Figure 2 and Appendix 1). These recorded current velocity and direction two meters above the seabed at five minutes intervals for almost six days (18 – 23 June).

Sampling of corals and sediments

Sediment sampling: Sediment cores were obtained with multicorer from 20 sampling stations within ca. 8000 m radius from the drilling site (Figure 4 and 5). Seabed backscatter intensity combined with the bathymetric information were used to select sampling localities. Potential accumulation areas such as small depressions or flat parts of the sea bottom containing relatively fine-grained (low reflectivity) sediments were targeted.

Up to five sediment cores (one 110 mm diameter and four 63 mm diameter) were obtained from each station. These cores were used to study Ba and barite distribution in sediments and to assess the spreading of drilling mud from the drilling site. The 110 mm core was subsampled onboard, whereas the 63 mm cores were capped and stored for transport to NGU (Appendix 2). In the laboratory at NGU the cores were split lengthwise and visually described. The length of sediment cores varied from 3 cm to 30 cm; limited penetration was characteristic for gravel-bearing sediments.

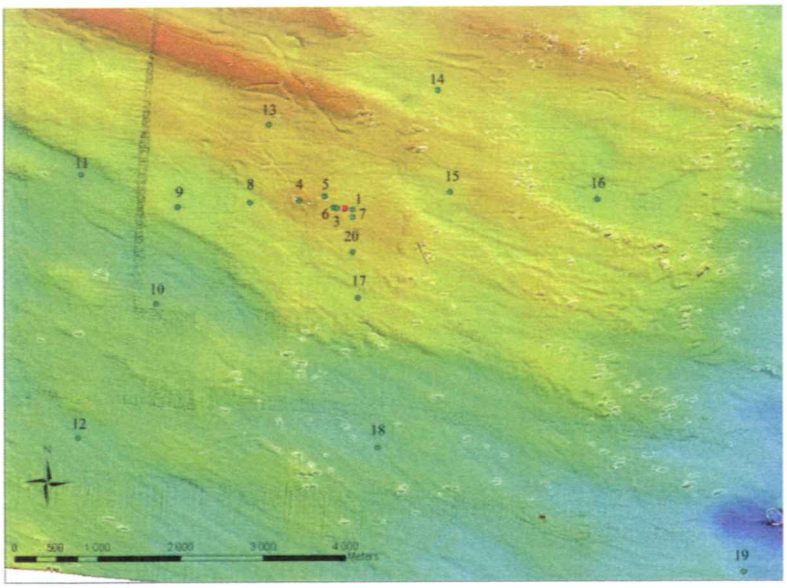

Figure 4. Shaded relief bathymetry map showing sediment sampling locations (green dots with station numbers) in the study area. The drilling site is indicated with a red dot.

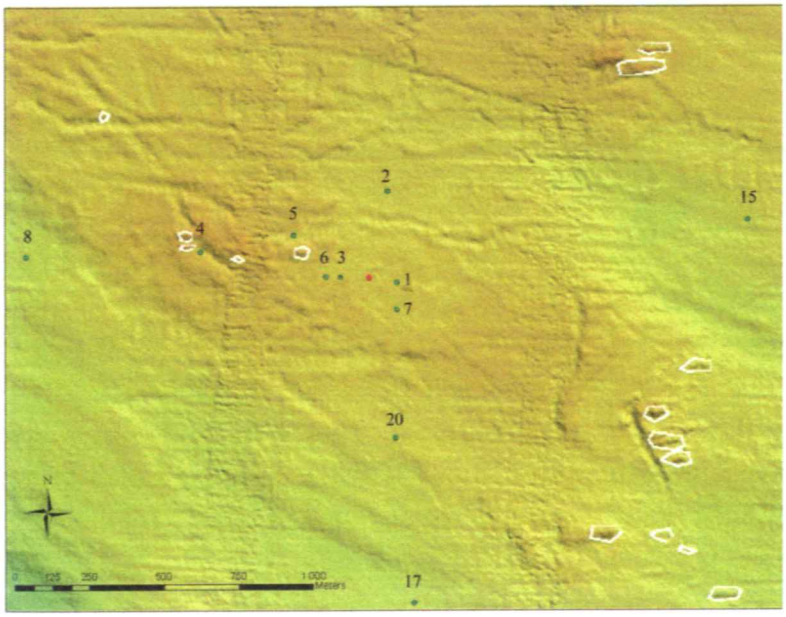

Figure 5. Sediment sampling locations (green dots with sampling numbers) and coral reefs in the vicinity of the drilling site (red dot).

Coral sampling: Eleven samples of corals were obtained with ROV and video assisted grab (0.25 m^2 van Veen grab with colour camera and light, see Mortensen et al. 2000 for description) from five locations near the drilling site and one location situated about 8 km to the northeast of the drilling site. Coral fragments with live polyps were targeted during inspection or slow transit close to the bottom. Only one sample was collected with the ROV per dive. The sample was stored in an open bucket during transit to the surface. The video assisted grab was suspended about 1 m above the seabed while drifting slowly over the targeted area. When a suitable colony was spotted, the grab was lowered to hit it on the top. The grab was slowly lifted from the seabed after it had released. After closing completely, the grab was hauled back at normal speed. Coral skeletons for preparation of thin sections were selected from eight samples.

Laboratory methods

XRF core logging

In contrast to conventional core logging devices (such as GeoTek Multi Sensor Core Logger (MSCL)), the X-ray fluorescence (XRF) core scanner is able to directly measure several parameters that are important for drilling mud discharge interpretations, such as Ba. Lengthwise split cores from seventeen stations (all those longer than 5 cm) were imaged optically and radiographically, and XRF scanned for Ba and other selected major and trace elements using Itrax Core Scanner at the factory in Gothenburg. This system allows imaging and non-destructive, in-situ geochemical analyses on split, wet cores (Croudace et al. 2006). X-rays that in this study were generated by the Cr tube anode at 30 kV and 50 mA, are in the Itrax system focused to a 20 x 0.2 mm rectangular beam (size of irradiated area) with its long axis perpendicular to the axis of the sediment core. The XRF logging was done using 0.5 mm step size and 2 second counting time. The obtained profiles show down-core variations in metal concentrations in relative arbitrary units (counts per second). The radiographic images that are likewise obtained from the 2 cm wide stripe at the centre of the split cores, allow recognition of sedimentary structures and textural variations along the core because various sediment types absorb X-rays differently. The absorption is generally lower for fine-grained sediments compared to coarse-grained sediments. On radiographic images, the lighter areas typically relate to fine-grained, low density sediments and darker areas to coarse-grained, higher density sediments or clasts.

Grain size analyses

Sediment grain size determinations were undertaken on surface samples (typically 0-1 cm) from all 20 sediment stations using wet sieving and laser diffraction (Coulter LS 2000) techniques. The Coulter LS 2000 measured the fractions from 0.4 µm to 2000 µm, while particles larger than 2000 µm have been determined by wet sieving. Prior to analyses the samples were dispersed in an ultrasonic bath. The grain size distribution reflects the volume distribution of various fractions with the assumption of uniform density.

Dating of sediment cores

Radiometric dating of sediments using ^{210}Pb-method was attempted on 10 selected cores by analyzing altogether 87 sub-samples. The typical sub-sampling scheme for dating included intervals 0-1, 1-2, 2-3, 3-4, 4-5, 6-7, 8-9, 10-11, and 14-15 cm. This scheme was, however, occasionally modified depending upon the lithology and length of cores. The samples were analysed for the activity of ^{210}Pb, ^{226}Ra and ^{137}Cs via gammaspectrometry at the Gamma Dating Center, Institute of Geography, University of Copenhagen. The measurements were carried out on a Canberra low-background Ge-detector. ^{210}Pb was measured via its gamma-peak at 46,5 keV, ^{226}Ra via the granddaughter ^{214}Pb (peaks at 295 and 352 keV) and ^{137}Cs via its peak at 661 keV.

Geochemical analyses of sediments

Concentrations of metals, sulphur and carbon were determined on 150 sub-samples from 18 sediment cores. The main focus of the geochemical analyses was to estimate the concentrations of Ba and heavy metals in recent sediments. Depending upon the lithology and

length of cores, the following intervals were typically analysed: 0-1, 1-2, 2-3, 3-4, 4-5, 5-7, 9-11, 14-15 cm.

Inductively Coupled Plasma – Atomic Emission Spectrometry (ICP-AES) and Atomic Absorption (AA): All reported major and trace elements except Hg were analysed using Thermo Jarrell Ash ICP-AES 61. Hg concentrations were measured using the CETAC M-6000A atomic absorption cold vapor Hg Analyser. For all these analyses acidified aqueous sample solutions were obtained by leaching 1 g of freeze-dried sediment in 7N HNO_3 in an autoclave at 120° C for 1 hour (Norsk Standard NS 4770). Note that this nitric acid leach does not attack resistant silicates, hence the metal values given are not total concentrations. Sand-size barite and bio-available fractions of heavy metals in sediments are, however, dissolved in 7N HNO_3 in an autoclave at 120 °C.

Total carbon, organic carbon and total sulphur by Leco SC analyser: The contents of total carbon (C_{tot}), organic carbon (C_{org}) and total sulphur were determined on the Leco SC-444 analyser using 100-350 mg samples. Carbonate was removed by 10% HCl prior to organic carbon measurements. The abundance of carbonate carbon (C_{carb}) has been calculated as the difference between C_{tot} and C_{org}.

X-Ray Fluorescence (XRF): Total concentrations of major and trace elements in sediments were determined by XRF on 135 sub-samples. For major elements, 0.6 g pre-ignited (1000°C) fine-grounded sample material was mixed with 4.2 g $Li_2B_4O_7$ and fused to a bead in a CLAISSE FLUXER-BIS. The analysis of trace elements was based on pressed powder. The preparation was based on 1.2 g (±0.005g) Hoechst wax and 5.4 g (±0.005g) sample, which is mixed in a Spex Mixer/Mill for at least 1 minute. The mixture was then pressed to a pellet in a Herzog pelletizing press (approx. 20kN, time = 20 seconds). Both major and trace elements were analyzed with a Philips PW 1480 WD-XRF instrument equipped with a Rh X-ray tube. The primary aim with these XRF analyses on sub-samples was to calibrate and evaluate the significance of Ba variations seen on XRF logs obtained by the core scanner.

Mineral separates

To confirm whether or not the elevated Ba concentrations in sediments are due to dispersed barite from drilling, heavy mineral separates were obtained from 10 samples using heavy liquid (diiodomethane, density 3.3 g/cm^3). Mineral separation was undertaken on two size fractions, 38-108 μm and 108-250 μm. Heavy mineral concentrates were examined, and barite crystals were identified using scanning electron microscope equipped with energy dispersive spectrometer (SEM-EDS).

Thin sections of coral skeletons

To expose the internal structure of coral skeletons, and to study the sediments trapped in polyps, nine series of thin sections were made. The sections were made longitudinally because the growth-lines are not continuous throughout the whole length of the coral skeleton. Normally, only the outer 2 to 15 cm of branches are covered with a living calcifying tissue. The typical length (along the main growth axes) of coral skeletons that were selected for thin

section preparation varied between 10 and 20 cm. Coral skeletons were broken into ca. 2 cm long fragments (perpendicular to the growth axes) and impregnated using Struers Epofix. Coral skeletons A13, A16, VG 33, VG36 and VG50 were treated with sodium hypochlorite (klorin) to oxidize the organic matter prior to the thin section preparation, while thin sections of A14, L26, L26B and L27 skeletons were made of untreated samples. Transects through the middle of coral skeletons were attempted, but due to the curving and branching nature of skeletons, it was sometimes difficult to cut the impregnated slabs exactly parallel to the growth axes. The thickness of polished thin sections was adjusted to ca. 200 µm. This thickness, which is somewhat thicker than normal thin sections (30 µm) was chosen in order to allow LA-ICPMS analyses to be undertaken directly on thin sections without a risk of completely ablating through the skeletons. The internal structure and growth lines in skeletons and sediment impurities in polyps were examined by means of optical microscopy and SEM (Scanning Electron Microscopy). The morphological features of the internal structure were in case of selected thin sections enhanced by treating the sample surface with 1% HCl for 3-4 minutes.

RESULTS

Video inspections

Six reefs around the drilling site were inspected with ROV (Table 1, Figure 7 and 8). Living *Lophelia pertusa* were predominantly found on the eastern (up-current) side of the reefs. To provide a visualisation of coral reef habitats on maps, three habitat types were defined based on relative composition of live *Lophelia*, dead *Lophelia* blocks, and *Lophelia* rubble (pieces of dead *Lophelia* < 20 cm) (Figure 6).

The total length of inspected coral habitats was 531 m (Table 1). The size of the inspected reefs varied between 42 and 255 m in longest extension (Table 1). The dominant habitat on the reefs was *Lophelia* rubble covering between 25 and 76 percent of the surveyed reef bottom (239 m in total). Areas dominated by blocks of dead *Lophelia* had a limited extent (30 m), but dead corals cover typically more than 50 % of the bottom also in the area with live *Lophelia*.

Table 1. Extension (m) of *Lophelia* coral habitats on six reefs investigated during three ROV dives. LR = *Lophelia* rubble, DL = dead *Lophelia*, LL = live *Lophelia*.

Dive No.	Reef No.	LR	DL	LL	Sum coral habitats (LR+DL+LL)
9	4	23		22	45
9	5	32		10	42
11	1	41	28	38	107
11	2	14		40	54
11	3	16	2	9	28
15	6	167		88	255
Sum		293	30	207	531

Video inspection provides no clear evidence of a reduced coral health that could be related to the reef's location relative to the drilling site. An example of the mapping of coral reef habitats is shown in Figure 9.

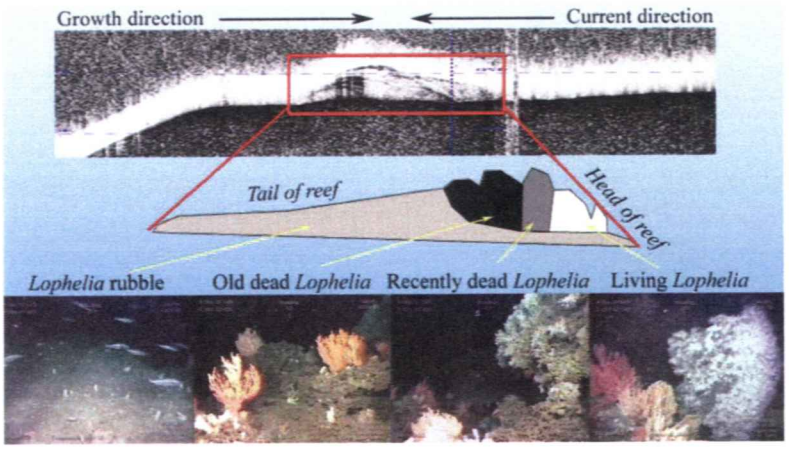

Figure 6. The elongated reefs in the Træna Deep grow towards the currents and exhibit clear zonation patterns. On top in the figure we see how a reef appear on a diagram made with Topas (a seismic instrument). Layers of coral stretch towards the current.

Live *Lophelia* – Live *Lophelia* present,
Dead *Lophelia* – No live *Lophelia* present and % dead *Lophelia* > *Lophelia* rubble,
Lophelia rubble – No live Lophelia present and % *Lophelia* rubble > dead *Lophelia.*

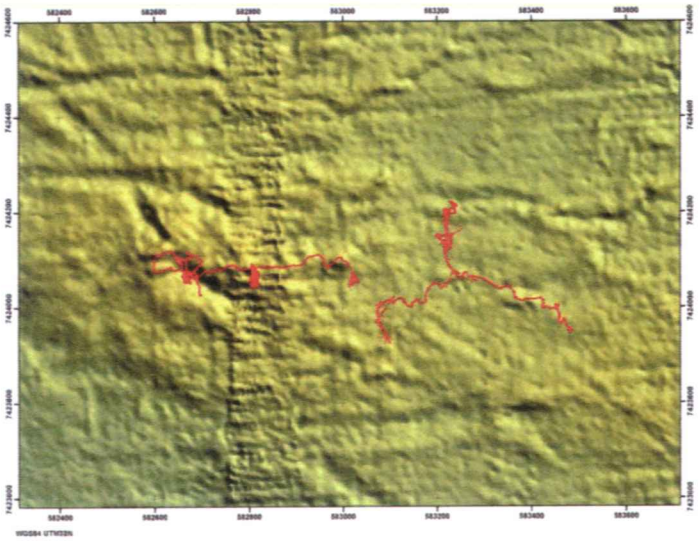

Figure 7. Tracks of the ROV dives on reefs around the exploration drilling site. Linear depressions are iceberg ploughmarks.

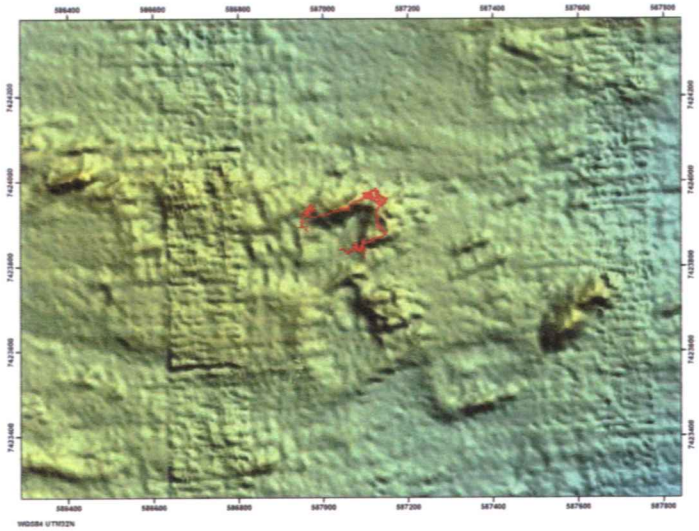

Figure 8. Tracks of the ROV dives on reefs up-current (east) of the exploration drilling well.

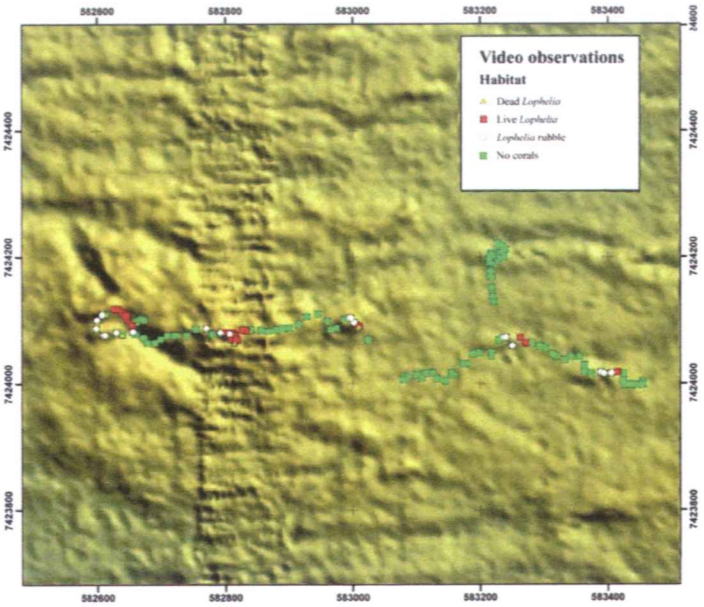

Figure 9. Distribution of main habitats along the ROV dive tracks on reefs around the exploration drilling site.

Current patterns

The current meters recorded velocity and direction for almost six days (Figure 10). The current velocity varied between 0 and 27 cm/s during the monitoring period. The area close to the exploration drilling site had the weakest currents, whereas the strongest currents were recorded about 12 km southeast of the drilling site. The current pattern showed tidal influence with a strong westward component. In general, the direction of elongated reefs coincided with the modal direction of currents as given in Figure 11. This was best seen in the reference areas north and southeast of the drilling site. Fan shaped colonies of the gorgonian coral *Paragorgia arborea* were observed on several reefs. These were oriented in the shape of a parabolic fan towards the same main current direction as documented with the current meters.

Sediment characteristics

Sediment grain size

A summary of sediment grain size characteristics is given in Table 2 and Figure 12. A complete list of grain size distribution data and calculated statistics is found in Appendix 3. Sediments in the study area are relatively coarse-grained (Table 2, Figure 13), and sand is a dominating size fraction at all stations except one (Station 4). However, the broad range of grain sizes and generally poor sorting of sediments manifest very variable depositional conditions and alteration of erosion and accumulation. A relatively high mud content (Figure 14) on the topographic high in the vicinity of the drilling site is somewhat surprising, because one would generally expect stronger currents on such ridges and hence more coarse grained sediments. The common occurrence of coral reefs on such ridges may, however, provide quiet areas behind reefs and locally facilitate enhanced accumulation of muddy sediments.

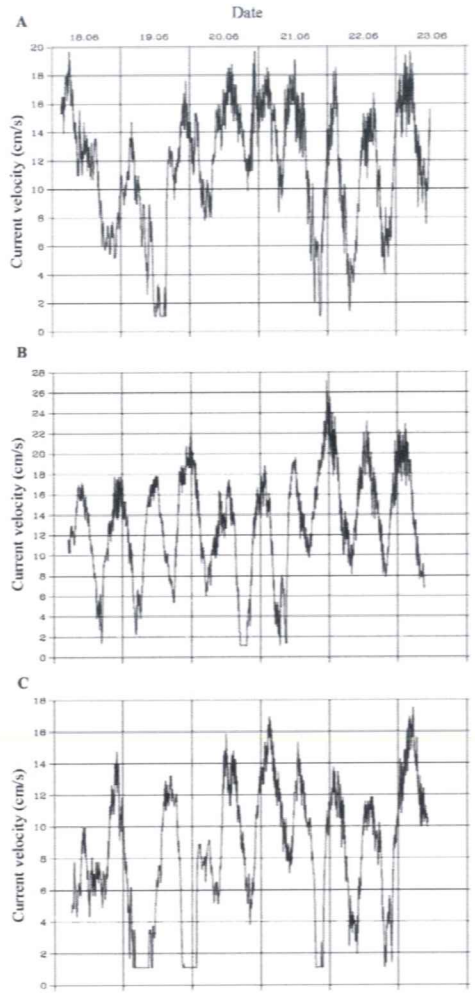

Figure 10. Changes in current velocity north of the exploration drilling site (A), close to the site (B), and southeast of the site. The diurnal tidal rhythm is clearly represented by peaks ranging from 9 to 27 cm/s.

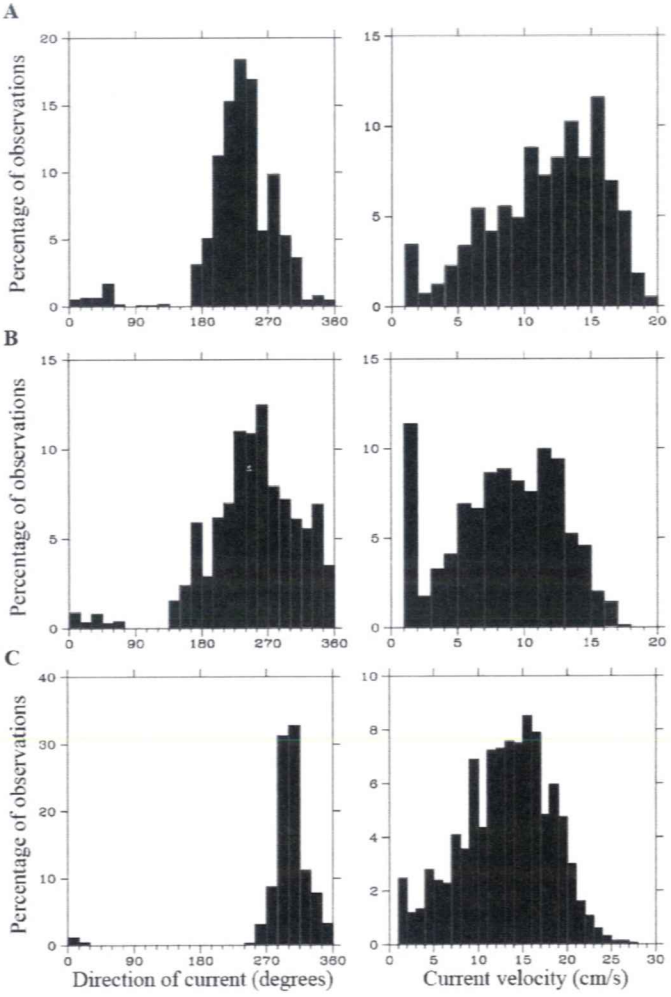

Figure 11. Frequency plot of current direction and velocity north of the exploration drilling site (A), close to the site (B), and southeast of the site (C).

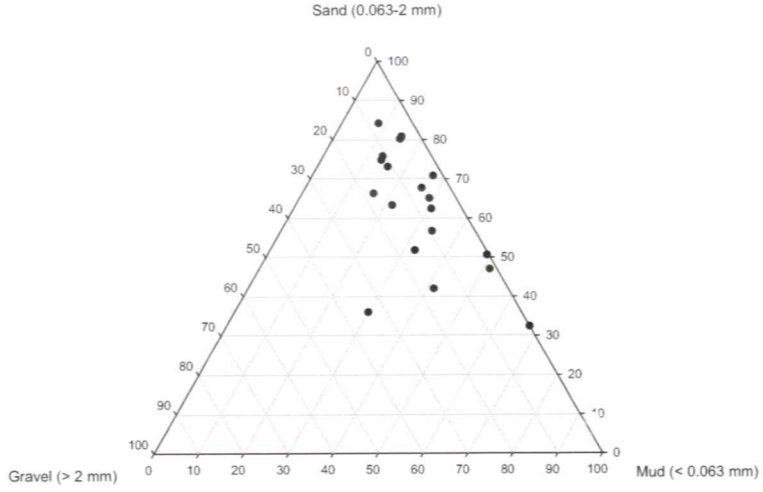

Figure 12. Ternary gravel-sand-mud diagram showing the dominance of sand in analyzed sediment samples.

Table 2. Grain size characteristics of analyzed sediment samples.

Station	Core ID_interval	Clay (%)	Silt (%)	Sand (%)	Gravel (%)	Median (μm)
1	C001_0-4	5.7	43.4	50.5	0.4	66.59
2	C007_0-1	3	24.1	70.7	2.2	158.8
3	C011_0-1	3.48	26.52	35.9	34.1	374.6
4	C013_4-6	7.1	60.6	32.3	0	28.83
5	C021_0-1	3.96	29.94	56.6	9.5	190.5
6	C026_0-1	4.94	36.66	41.9	16.5	113
7	C031_0-1	3.51	27.39	62.3	6.8	170.9
8	C037_0-1	2.54	19.26	63.2	15	347.5
9	C043_2-3	2.08	13.82	73	11.1	246.9
10	C047_0-1	2.09	13.01	80.1	4.8	242.7
11	C051_0-3	3.32	25.78	65	5.9	174.1
12	C057_0-1	5.52	45.98	46.9	1.6	57.3
13	C061_2-3	3.1	23	67.6	6.3	191.4
14	C066_1-2	1.92	14.18	66.2	17.7	490.6
15	C070_0-1	2	13.1	80.7	4.2	449.4
16	C075_0-1	1.8	11.6	75.7	10.9	513.9
17	C080_0-1	1.8	11.6	75.7	10.9	513.9
18	C085_0-1	0.92	7.39	84.09	7.6	741.7
19	C090_0-1	3.34	29.16	51.7	15.8	137.1
20	C095_0-1	1.9	11.7	74.7	11.7	501.8

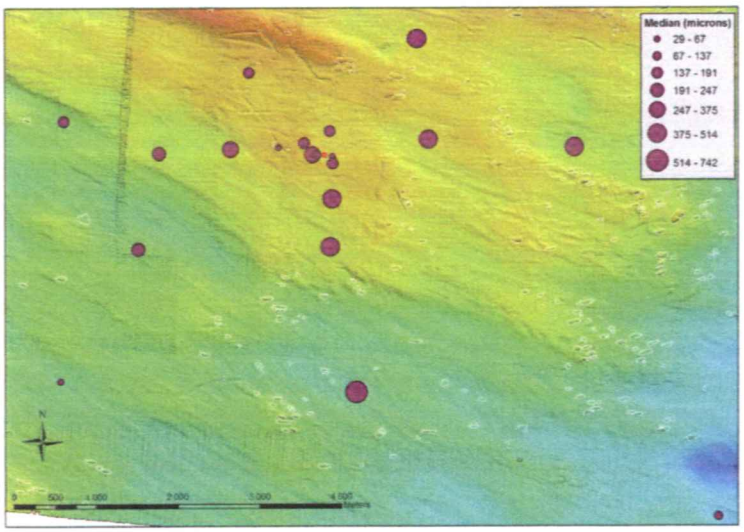

Figure 13. Geographic distribution of median grain size (μm) of analysed samples. Red dot marks the location of the drilling site.

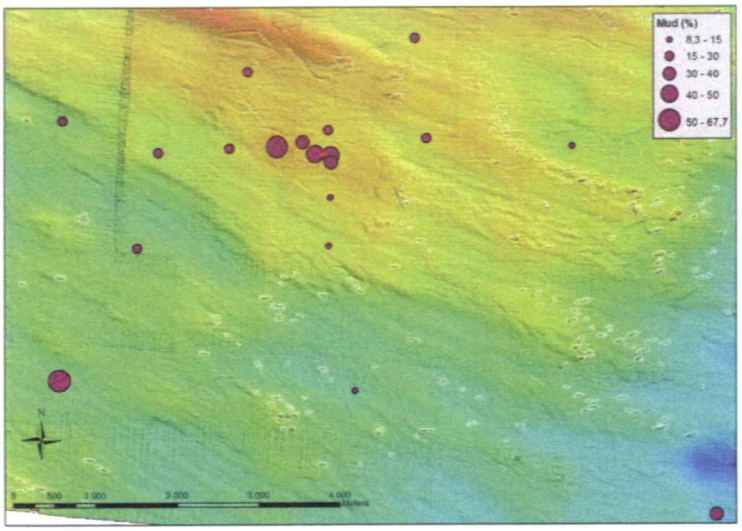

Figure 14. Mud (< 63 µm) content in analyzed samples. Note that mud content is above 50 % only in two samples. Red dot marks the location of the drilling site.

Sedimentation rates

Relatively coarse-grained texture of sediments indicates that erosion and/or by-pass (transport) are the prevailing sedimentary processes at the seabed in the area. These high velocity processes complicate the accurate radiometric dating of cores as some sediment intervals (time slices) can be removed or sediments with different ages can be mixed together. Radiometric dating gives most reliable results in case of relatively uniform sediment accumulation rates, but models have also been developed that allow the dating of sediments from dynamic basins with variable sedimentation rates (Appleby 2001).

The obtained dating results (full dating reports are shown in Appendix 4) suggest that the time slice corresponding to 1992-1993, i.e. the year of drilling, present within the top two centimeters of the sediment column is in all ten cores (Figure 15). Due to the apparent sediment reworking and disturbance within surface sediments, it is possible that the top sediments (1-2 cm) are mixed and represent the average sediment of the last ca. 20 years.

It is interesting, however, to note that calculated ^{210}Pb supply rates to the sediments in the area (170-630 Bq m^{-2} y^{-1}; Figure 16, Appendix 4) are well in excess the atmospheric flux (66-91 Bq m^{-2} y^{-1}) measured in Scandinavia (Appleby 2000). The ^{210}Pb supply rates do not appear to be controlled by sediment grain size, as there was no significant correlation between the median diameter of sediments and ^{210}Pb supply rate. The excess flux is often interpreted to reflect sediment focusing, whereas supply rates below atmospheric flux are thought to be due to sediment remobilization and removal (Appleby 2000). This two-dimensional model is evidently not applicable in the area of the present study that is clearly being subjected to erosion and removal of fine-grained, ^{210}Pb-carrying hemipelagic sediments, yet the calculated supply rates are in excess of atmospheric flux. The exact mechanisms behind such high apparent ^{210}Pb supply rates and geographic variability are yet to be proven, but sediment mixing and repeated re-washing and accumulation may result in enhanced concentration of ^{210}Pb-carrying finer grained particles into the surface layers. On the larger scale, there might well be a net loss of ^{210}Pb from the area, but the remaining ^{210}Pb might due to re-suspension with low burial rate stay effectively in the surface layer. Such redistribution process within the

sediment column might provide an explanation for the high ^{210}Pb activity in the surface sediments.

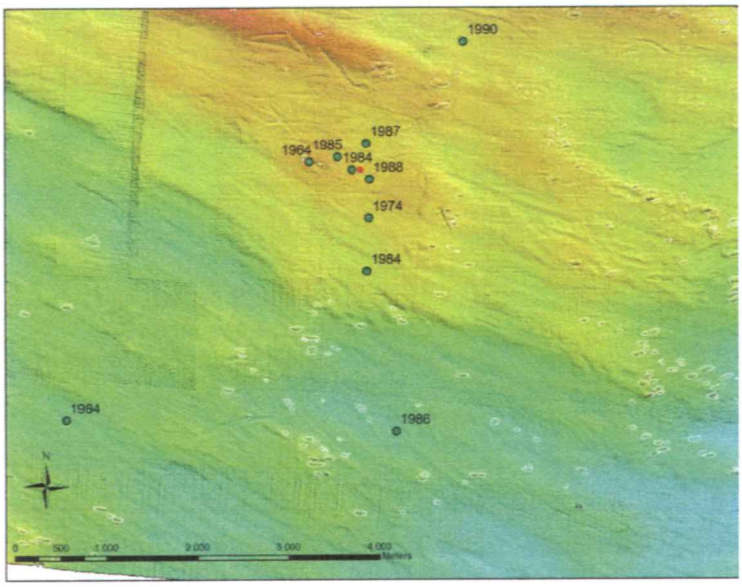

Figure 15. Map showing the ^{210}Pb age of the sediment slice from the 1-2 cm depth interval in 10 dated sediment cores. Most ages on the 1-2 cm sediment slice cluster between 1984 and 1990, and suggest that the sedimentary record from the last ca. 20 years is to be found within the top two centimetres of the sediment column. Red dot marks the location of the drilling site.

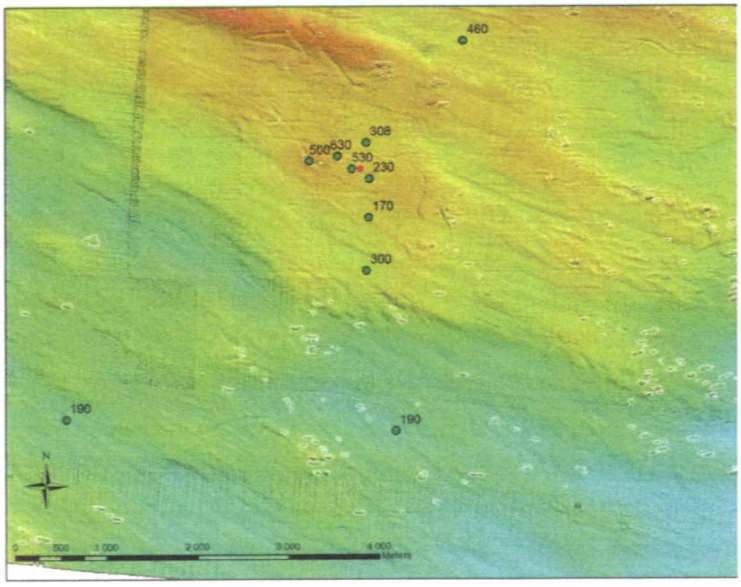

Figure 16. Calculated ^{210}Pb supply rates (Bq m^{-2} y^{-1}) based on ^{210}Pb inventories of 10 analyzed sediment cores. Red dot marks the location of the drilling site

Barite abundances in mineral separates

Barite crystals are clearly present in the surface sediment in the vicinity of the drilling site. Highest barite abundance was found in sediments of station 4, where its concentration in the fine sand /coarse silt fraction (38-108 µm) was ca. 5 % (Table 3, Figure 17).

Table 3. Barite abundances (%) in the heavy fraction (> 3.3 g/cm^3) of analyzed samples.

Station	Core ID_interval	Fraction 38-108 (μm)	Fraction 108-250 (μm)
2	C005_0-2	0.2	0
4	C013_0-2	5	2
4	C013_2-4	1	0.2
5	C022_0-2	1	0.2
6	C027_0-2	2	0
6	C027_2-4	0.5	0
8	C036_0-2	0.5	0.1
9	C043_0-2	0	0
11	C052_0-2	0.2	0
13	C061_0-2	0.1	0

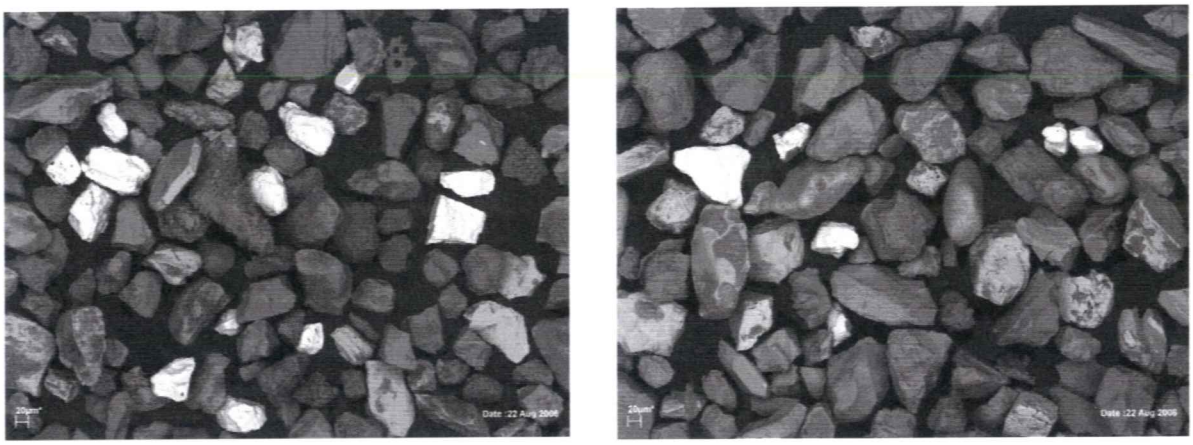

Figure 17. Scanning electron microscope backscatter electron (SEM BSE) images of mineral separates from surface sediments (0-2 cm) at stations 4 (left) and 6 (right). Barite crystals are seen on these images as bright particles due to their relatively high average atomic number that results in strong (bright) backscatter response. Most other particles are silicates such as amphiboles, pyroxenes and garnet.

Among the two size fractions analyzed, barite was more abundant in fine sand/coarse silt compared to medium sand (Table 3). This likely relates to barite grain size distribution in the drilling mud. Barite abundance decreases with the distance from the drilling site. Only a few crystals were found in the sediments of stations 11 and 13 (only in the finer size fraction) whereas no barite was detected in the sediments of station 9 (Table 3). Some barite grains bear signs of mechanical abrasion, as the sharp edges and corners of crystals are partly rounded off, but most of the grains are angular and differ from silicate grains that often are more rounded. This roundness contrast indicates that barite grains have had a short history in the sedimentary cycle, consistent with their recent discharge to the sea bottom in connection with the drilling activity. The morphological inspection of barite crystals from two sub-surface samples (2-4 cm, stations 4 and 6) did not reveal any dissolution features, indicating that barite has not been subjected to reductive dissolution in the diagenetic sulphate reduction environment.

Sediment geochemistry

Core logger results: Tracking of drilling mud barite in sediment cores with aid of the XRF core logging system turned out to be difficult. Core descriptions, optical and radiographic images (Figure 18 and 19, Appendix 5) demonstrate heterogeneous and relatively coarse-grained character of sediments.

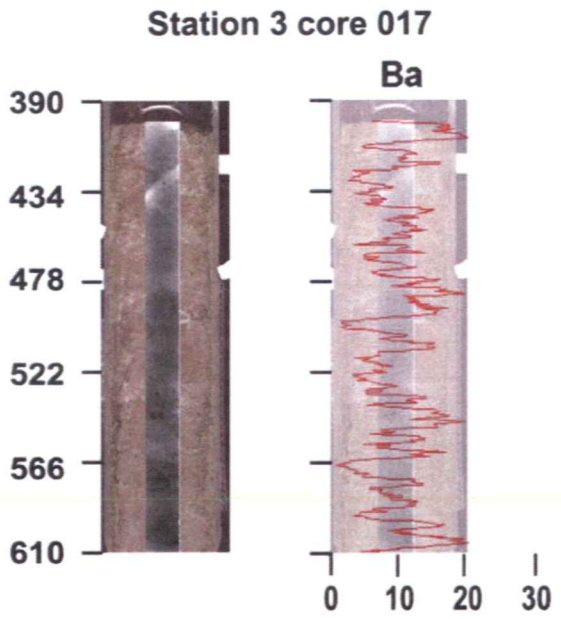

Figure 18. Optical and radiographic images and XRF Ba profile of core 017 from sampling station 3. Note that the core is ca. 21 cm long (Y-axes on the image shows instrument's arbitrary scanning interval in millimeters). Ba profile (counts) is rather variable, and it is not easy to realize that higher count rates at the surface are due to the contribution from the drilling mud barite. Notable drilling mud barite within the surface sediments was proved to be present by ICP-AES and mineral separation results.

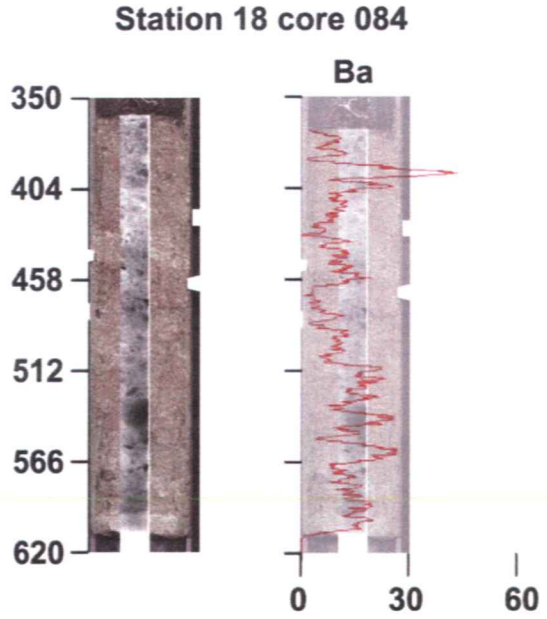

Figure 19. Optical and radiographic images and XRF Ba profile of core 084 from station 18. Note that the core is ca. 25 cm long (Y-axes on the image shows instrument's arbitrary scanning interval in millimeters). Ba profile (counts) shows significant sub-surface enrichment at ca. 2 cm, which according to ICP-AES results is not controlled by barite, but likely relates to elevated contents of Ba-rich silicates within this layer.

This heterogeneity allows a considerable down core variation in the background, bulk Ba concentrations because phases carrying natural Ba, such as feldspars and clays, are not stratigraphically uniformly distributed. Background Ba concentrations (count rates) vary by a factor of 3-4, and this makes it difficult to unambiguously trace the minor drilling mud barite component. Bulk Ba concentrations in sediment intervals containing most barite such as surface sediments of stations 4-6, are similar or even lower compared to some barite free intervals that are rich in natural Ba-carrying phases, possibly alkali feldspars and mixed-layer clay minerals (Figure 18 and 19, Appendix 5). For example, the distinct subsurface (ca. 2 cm) Ba peak on the profile from station 18 (Figure 19), which gives the highest observed Ba count rates among all XRF logged cores, is due to the abundance of Ba-rich silicates in this interval, and not to drilling mud barite. This manifests that drilling mud barite might be left unnoticed on the XRF core logger profiles if barite Ba concentrations in sediments are below ca. 1000 mg/kg (Figure 22).

ICP-AES, AA, Leco and XRF results: Ba concentrations in leachates obtained by digesting the sediment samples in 7N HNO_3, show distinct surface/subsurface enrichment in cores from the vicinity of the drilling site. Ba concentrations in the deeper intervals (> 5 cm) of sediment cores are relatively stable and vary typically between 40 and 80 mg/kg, with the exception of station 13 where Ba concentration reaches 150 mg/kg (Figure 21). These values in sediment intervals deeper than 5 cm reflect Ba concentrations in natural sediments in the area, and can be considered as background Ba values. Surface and subsurface (< 5 cm) sediments from three stations (4, 5, 6) in the vicinity of the drilling site have pronounced Ba enrichments with concentrations between 600 and 1200 mg/kg (Figure 21). The surface enrichment is less pronounced, or absent in cores relatively distant from the drilling site. Considering that the nitric acid attacks readily barite, but does not dissolve resistant silicates, it appears reasonable to claim that these Ba enrichments in surface/sub-surface sediments are due to barite, which is also consistent with the observations made on mineral separates. Elevated Ba concentrations, if present, are seen within the top 2-3 centimeters, which according to the ^{210}Pb dating results archive the last 20 years of the sedimentation history. Hence it is very likely that this Ba reflects barite that was released to the sea bottom in connection with the exploration drilling.

In order to quantify the component of Ba that is derived from the drilling mud barite in the surface sediments, a parameter named "excess Ba" was calculated using the following formula: $Ba_{excess} = Ba_{surface} - (Ba_{background} \cdot Al_{surface} / Al_{background})$. In this calculation the silicate-bound Ba in the surface sediments is estimated using Al concentration in surface sediments, and Ba and Al in the lowermost parts of the cores, and the excess Ba is given as a difference between the measured Ba ($Ba_{surface}$) and silicate-bound Ba ($Ba_{background} \cdot Al_{surface} / Al_{background}$) in each core. The geographic distribution of excess Ba (Figure 20) reveals that a significant amount of drilling mud barite is found in the surface sediments in the vicinity (within ca. 500 m) of the drilling site. A fan of traceable barite (excess Ba 40-80 mg/kg) extends several kilometers towards west and northwest from the drilling site. Such a distribution pattern of excess Ba reflects westerly transport of sediments, which is consistent with the prevailing currents in the area.

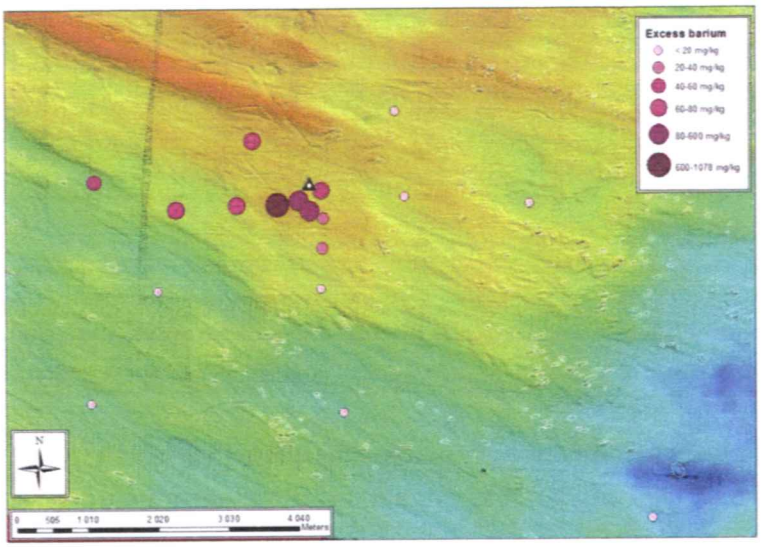

Figure 20. Geographic distribution of the excess Ba in the surface sediments. Excess Ba was calculated using the formula $Ba_{excess} = Ba_{surface} - (Ba_{background} \cdot Al_{surface} / Al_{background})$. Triangle marks the location of the drilling site.

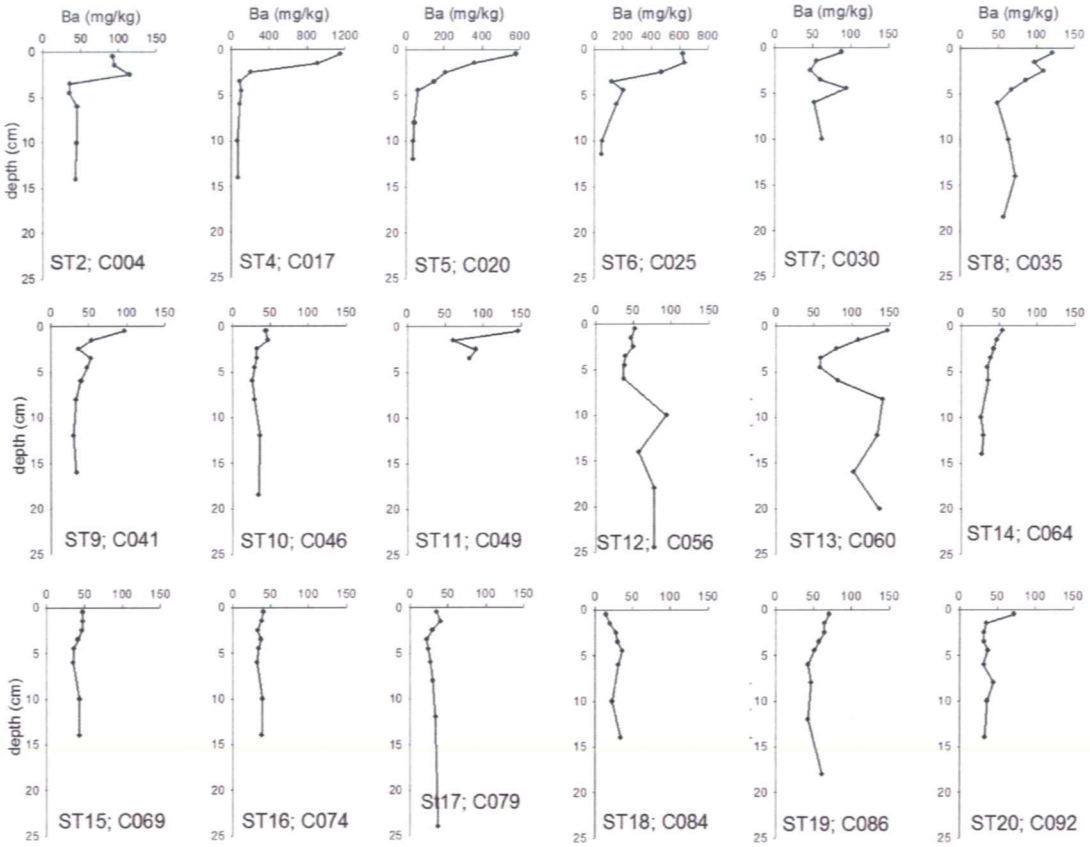

Figure 21. Stratigraphic profiles of Ba concentrations (7N HNO_3 leachates). Note that the Ba concentrations range (x-axes) is kept constant (from 0 to 150 mg/kg) on all profiles except three stations (ST4, ST5, ST6) that have significant surface/subsurface enrichments.

Highest values of excess Ba were found in station 4, where most fine-grained and clay- and silt-rich sediments occur. This indicates that the geographic distribution of drilling barite in the area is strongly influenced by the sedimentary regime at the sea bottom. In high-energy environments where sandy and gravelly sediments dominate, the silt-size barite, which is the predominant fraction in the drilling mud (Rye, 1996), may largely be by-passed and have thus limited accumulation. Relatively quiet areas with muddy bottoms are apparently the environments where the hydrodynamic conditions are most suitable for accumulation of silt-size barite from drilling mud. Accounting for the possibility of effective re-distribution of drilling mud barite by bottom currents, the geographic extent of excess Ba around the drilling site might not quite represent the area that is influenced by the drilling mud. The geographic extent of excess Ba around the drilling site traces the minimum size of the influence area, but the actual influence area is likely considerably larger.

The XRF analyses of total Ba in sediments were undertaken on 135 subsamples that had previously been analyzed for Ba and other elements in 7N HNO_3 leach. Concentrations of bulk Ba in sediments that are free of drilling mud barite vary typically between 300 and 500 mg/kg. Figure 22 shows the positive correlation between the total Ba and Ba extracted by 7N HNO_3 leach, with the intercept of ca. 300 mg/kg. This relationship demonstrates that in studied sediments, the 7N HNO_3 attack leaches only ca. 20% of silicate-bound Ba. None of

the samples that are free of drilling mud barite have total Ba concentrations above 600 mg/kg, whereas most barite-rich samples have bulk concentrations above 1000 mg/kg. XRF core logger data, however, indicated comparable Ba concentrations in barite-rich surface intervals and some subsurface, barite free intervals, but this indication, surprisingly, is not supported by the XRF data on 1 cm thick sub-samples. An explanation to this discrepancy might lie in the coarse grain size and heterogeneous, localized distribution of Ba-rich silicates, for examples alkali feldspars. Ba-rich intervals are typically thin (< 1 cm) on the core logger profiles (Figure 18 and 19), and in these thin intervals Ba concentration may locally reach 1000 mg/kg or more. However, such local enrichment might get effectively diluted and become depressed if measurements are made on 1 cm thick sub-samples that integrate a larger sediment volume than just the thin, Ba-rich interval.

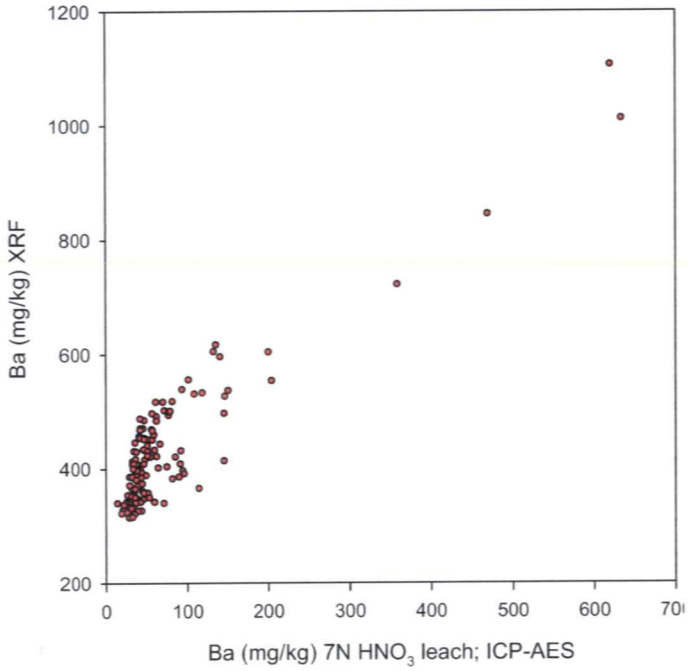

Figure 22. Correlation between Ba concentration in 7N HNO_3 leachate and total Ba (XRF).

Leachates (7N HNO_3) used for Ba determinations were also analyzed for selected major and trace elements including heavy metals. Stratigraphic profiles of these selected elements and C_{org}, C_{carb} and S_{total} are given in Appendix 6. According to the environmental state classification by the Norwegian Pollution Control Authority (Molvær et al. 1997), the concentrations of environmentally significant elements such as Zn, Cr, Ni, Hg and As in the studied sediments generally correspond to the class I - minor or no contamination. Stratigraphic profiles of Pb and Cu show a clear enrichment from deeper intervals towards the sediment surface (Appendix 6). Concentrations of Cu and Pb in the surface sediments are geographically variable (Figure 23 and 24). Cu concentrations in the surface sediments correspond to the environmental class I (< 35 mg/kg) at 12 sampling stations, class II (moderate contamination; 35-150 mg/kg) at 5 stations and class III (distinct contamination, 150-700 mg/kg) at one station (ST7) that is located a few hundred meters south of the drilling site. It is not clear whether or not the Cu enrichment at this most contaminated site it is due to the drilling activity. However, since this and two other most Cu rich stations (ST4 and ST5) cluster in the

vicinity of the drilling site (Figure 23), it is possible that the observed Cu enrichments at these three stations are related to the drilling. Pb concentrations correspond to environmental classes I (< 30 mg/kg; 9 stations) and II (30-120 mg/kg; 9 stations). The geographic pattern of Pb is generally chaotic, and does not seem to be influenced by the drilling activity.

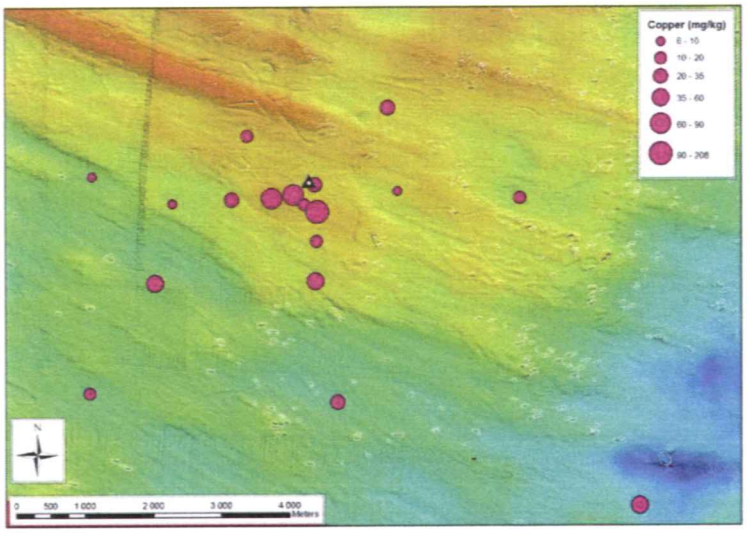

Figure 23. Copper distribution in the surface (0-1 cm) sediments. The triangle shows the position of the drilling site. Note that the highest Cu concentrations cluster in the vicinity of the drilling site that might indicate Cu contamination in connection with the drilling. Triangle marks the location of the drilling site.

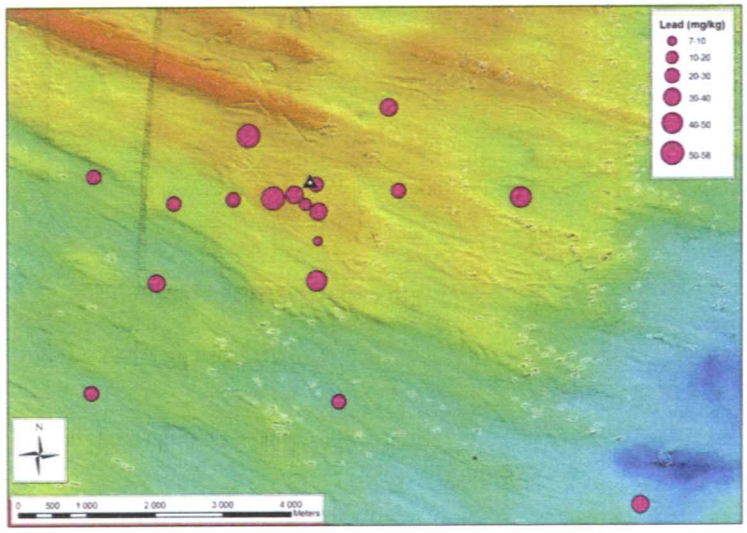

Figure 24. Lead distribution in the surface (0-1 cm) sediments. The triangle shows the position of the drilling site. Triangle marks the location of the drilling site.

Skeleton characteristics

Skeleton growth-lines

Thin sections of coral skeletons from eight localities on six reefs (Figure 25 and 26) were inspected using close-up photography, transmitted light microscopy and scanning electron microscopy. Three skeleton samples, two from the middle (VG30, VG31) and one from the eastern end (A14), were studied from a west-east stretching reef, situated ca 600 m SW of the drilling site (Figure 26).

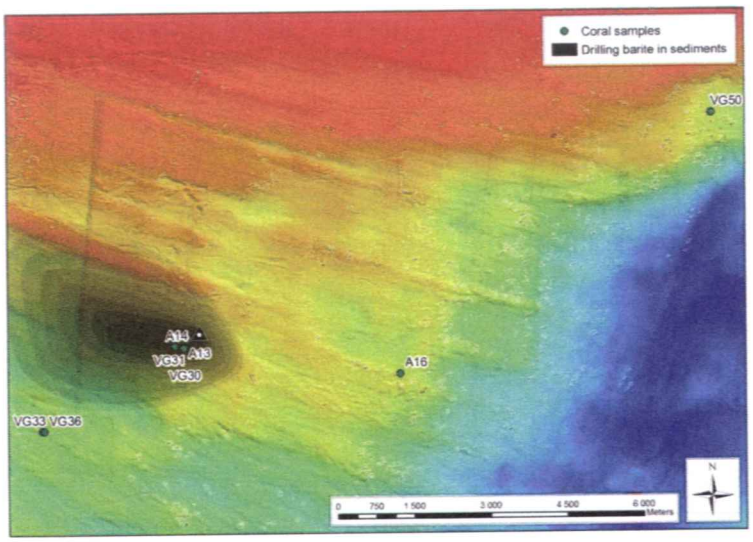

Figure 25. Sampling localities of coral skeletons and geographic extent of drilling mud affected seabed. Shading from dark to pale grey grades the degree of drilling mud influence that decreases with increasing distance from the drilling site (shown by a triangle).

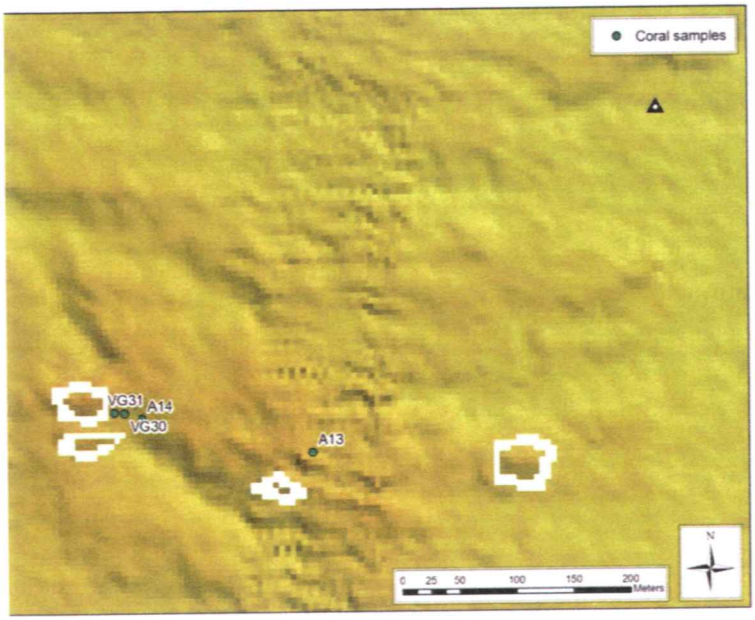

Figure 26. Sampling localities of coral skeletons in the vicinity of the drilling site (shown by a triangle).

Other studied reefs were represented by a single skeleton specimen. One series of thin-sections was provided from each sample except for VG30 where two series were made (Table 4).

The skeleton can be classified in two main types: skeleton of living polyps with a live tissue cover (live skeleton) and skeleton without a live tissue cover (dead skeleton). All of the analysed coral branches had at least one live polyp (Table 4). Branch VG30 had to be supplemented by a side branch (VG30b) in order to have a living reference polyp. Two of the branches consisted solely of living polyps. but on average, three polyp generations were alivie. Coral branches with a large proportion of living polyps are probably in a "good condition" with a high growth rate. In order to find long time series over a short distance within the skeleton, partly living coral branches were selected for thin sectioning and examination.

Table 4. Life span, based on counts of clear growth lines in sections of coral polyps of different generations. The outermost, youngest polyp (end of branch) is numbered as generation 1. Previous mother polyps are successively numbered with increasing number. Living polyps are indicated with bold numbers.

0 Mean age											
Generation#	VG33	VG36	VG31	A14	VG30	VG30b	A13	A16	VG50	Live	Dead
1	**3**	**5**	**7**	**4**	8	**7**	**4**	**3**	**2**	4.4	8.0
2	**4**	8	**7**	**5**	10	10	**5**	**4**	4	5.0	8.0
3	**6**	11	8	**7**	10	12	**7**	**5**	6	6.3	9.4
4	**9**	13	7	8	10	8	**8**	**6**	8	7.7	9.0
5	11	15	8	9	11		**9**	**7**	10	8.0	10.7
6	11	18	10	11	11		**9**	**8**	12	8.5	12.2
7	15			13	11		**11**	**8**	14	9.5	13.3
8				13	13			**10**		10.0	13.
9				13	12						12.5
10					13						13.0

Growth-lines were visible in thin-sections from both the septa (the fine ribs inside the skeletons, see Figure 27 for explanation to the skeleton structures) and theca (the skeleton wall) parts of the skeleton. The growth lines were clearest in the septa, but since these are thin and often curved, the sections often covered only short time series of the septa. In the theca, growth lines often occurred closely spaced with weak contrast, making exact counts difficult.

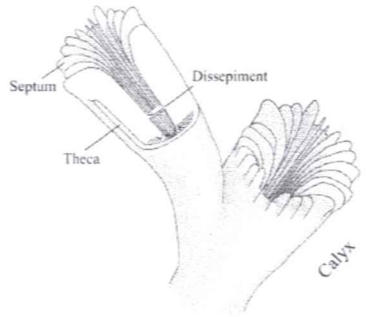

Figure 27. Schematic illustration of the skeleton of two polyps (calices) of *Lophelia pertusa*, one mother polyp (the large one to the right) and a daughter polyp (the small one to the left). The small one is cut open to display the inner structures.

In most thin section series through coral skeletons it was possible to connect growth-lines in sequential thin-sections (Figure 30). However. it was difficult to find the inner ends (border between tissue-covered and exposed skeleton) of growth lines that did not extend all the way back to a mother polyp. Such invisible growth line separations may be present in series of thin sections from dead calices (the skeleton "houses" of the polyps). The "blind" ends of growth lines result in under-estimation of polyp age, since the years represented by growth lines covering only parts of the branch should be added to the age estimated for the older parts of the branch.

Between 10 and 18 lines were present in calices from the lower part of the coral branch (Table 4). The distal (outer) ends of the growth lines occur closer to each other in the distal part of the calyx than closer to the basis near the mother polyp. The mean age of skeleton of living polyps was 6.3 years, whereas the life span of dead polyps was 10.6 years on average. Table 4 has examples of mother generations being younger than their offspring. This has two explanations: daughter polyps have longer life span than their mother polyps. or that closely spaced, unresolvable growth lines are present in mother polyps.

In most sections, there were between one and three growth lines between the branching points. This indicates that a new polyp is normally generated within the polyps first three years. However, wide polyps with thick calcification layers had more growth lines between the generations, indicating a slower growth. The relationships between the life span and number of generations (Figure 28 and 29) indicate that dead polyps became older than the present age of living ones, but also that one new generation per year is common in polyps more than two generations old. Slowly growing corals are represented by steep lines in figure 28. Most of the coral branches display relative straight lines with an increment of one year or more per generation (Figure 28), with the exception of VG31, VG30, and VG30b, Figure 30 shows an example of a thin section with a high number of visible growth lines. The oldest coral fragment, VG36 was 18 years old when it died. Unfortunately it was not possible to determine the year when it died, but it is likely that the oldest polyp was generated more than 20 years ago.

In the septa, transparent, thick growth lines as well as delicate lines were present (Figure 31). In some cases as shown in Figure 31 where the septa were preserved almost intact in the thin-section, around 12 fine lines were identified between the thicker lines. This probably demonstrates the lunar (tidal) cyclicity of the growth line formation as earlier suggested by Mortensen & Rapp (1998).

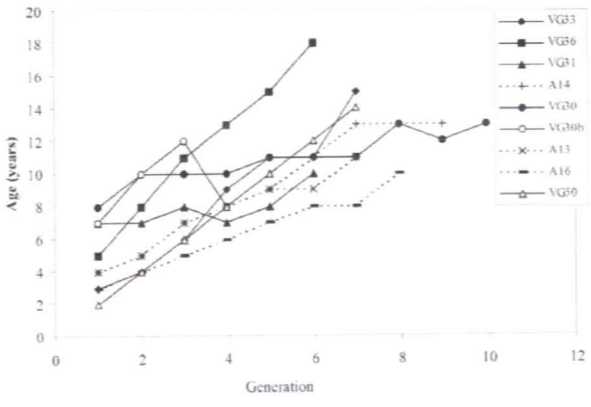

Figure 28. Life span (age) of polyps versus generation number for coral branches.

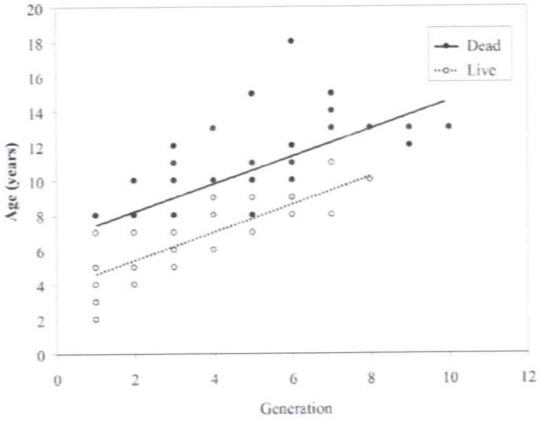

Figure 29. Life span of polyps versus generation number. grouped into dead and live.

Figure 30. Collage of longitudinal sections trough a branch tip of thin-section series VG36. The inserted image shows details of growth line patterns in the older part of the skeleton. The life span of this coral in the lower thin-section shown here was estimated to 11 years. Scale bar = 2 cm.

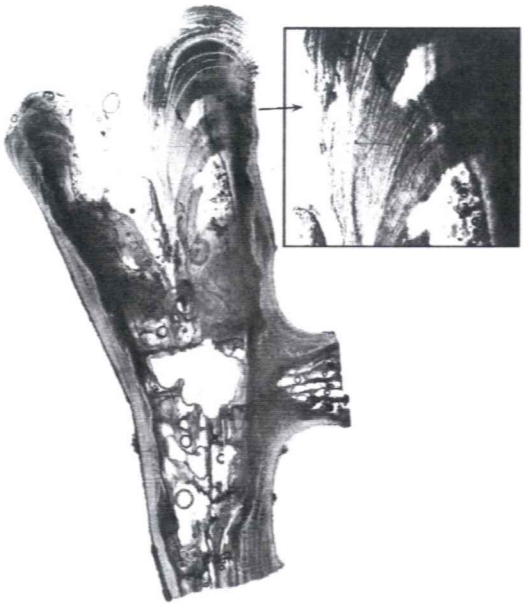

Figure 31. Example of fine growth lines in the septa from section L26B-1, observed in transmitted light microscope.

Impurities in coral skeletons

Fine-grained detrital sediments and calcareous and siliceous biogenic debris were commonly found within the calyces from six localities (A14, VG30, VG31, VG33, VG36 and VG50; Figure 32) whereas corals from two localities (A13 and A16) are largely free of impurities (Table 5). Barite crystals do not seem to be incorporated in the skeleton to a great amount, but accumulate within the calices and other crevices in dead skeletons. Two specimens (VG30 and VG31) appear to have been particularly affected by sediment accumulation. Sediments in calyces of these specimens are more abundant and coarser (sandier) compared to others, and contain mm-scale clasts of consolidated, framboidal pyrite bearing sediments (Figure 33). Barite crystals were identified in the calyx of four specimen (VG30, VG31, VG 33 and VG50; Table 5). Barite is rare and small (< 10 μm) in VG33 and VG50 while it is relatively abundant and reaches 60 μm in diameter in VG30 and VG31 (Figure 34).

Findings of relatively abundant barite in coral polyps of VG30 and VG31 signify the influence of drilling activity and drilling mud discharge on the reef 600 m SE of the drilling site, which is consistent with the distribution pattern of excess Ba (Figure 20 and 25). Drilling influence on this reef is also suggested by the presence of clasts of consolidated sediments, containing framboidal pyrite. These consolidated clasts are likely derived from older sediments that were released onto the seabed from deeper layers in connection with the drilling. Consolidated clasts may have also been eroded from old sediments exposing at the

sea floor, but the presence of chemically meta-stable framboidal pyrite in these clasts indicates relatively recent release, and appears thus consistent with their discharge in connection with drilling. It is interesting to note that sediment-rich and drilling mud influenced corals (VG30, VG31) occur in the central and western part of the reef, whereas the eastern end of this reef (A14) is free of barite and drilling mud (Table 5). Considering the close proximity of these three localities (Figure 26), one would expect to find barite in all coral samples if they were present during the drilling operation. Since there is no evidence of drilling mud in A14, it can be suggested that the eastern end of the reef post-dates the drilling activity.

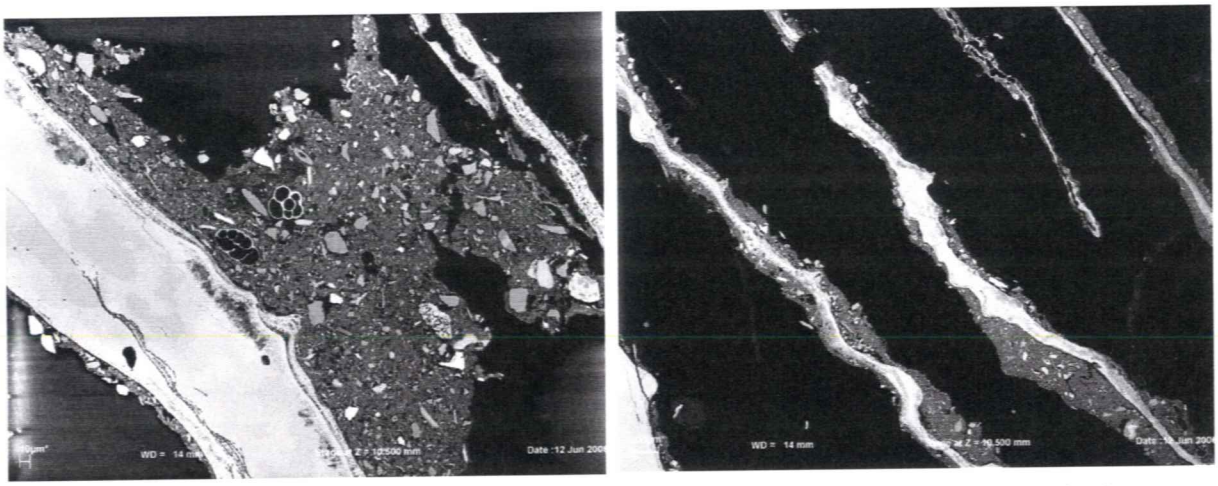

Figure 32. Scanning electron microscope backscatter electron image (SEM-BSE) of detrital fine grained sediments and calcareous and siliceous debris that is attached to the septa inside the calyx. Images from thin-section VG36-7.

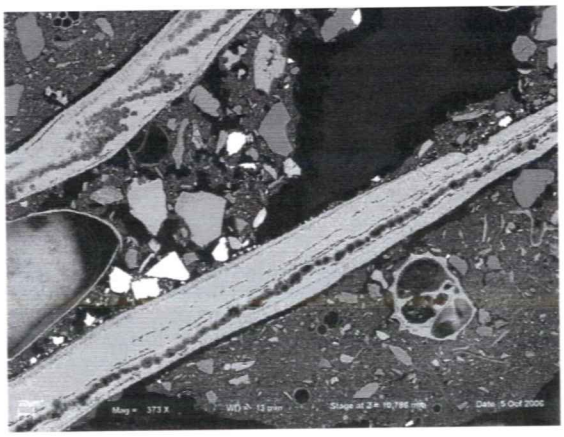

Figure 33. Scanning electron microscope backscatter electron (SEM-BSE) images of sediment impurities in coral calyx. Barite crystals that vary in diameter from a few microns to ca. 60 µm are seen on these images as bright particles due to their relatively high average atomic number that results in strong (bright) backscatter response. Image from thin section VG31-5.

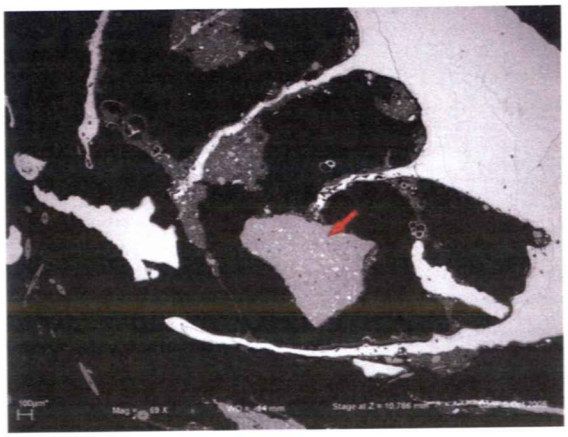

Figure 34. Scanning electron microscope backscatter electron (SEM-BSE) image of sediment impurities and a clast of consolidated sediment (indicated by a red arrow) in coral polyp. Note the higher backscatter intensity of the clasts compared to other sediments, which is due to the clast's lower porosity and organic matter content. Image from thin section VG31-5B.

The origin of fine-grained barite in skeletons of VG33 and VG50 from reefs that are relatively distant from the drilling site is ambiguous. Accounting for the strong currents in the study area, the transport of fine-grained drilling mud barite over long distances is possible (Lepland et al. 2000) hence the drilling site appears as a plausible source for barite seen in VG33 and VG50. In order to conclusively rule out other barite sources (Church 1979; Dehairs et al. 1980), a detailed trace element and isotope characterisation of individual crystals would be needed.

Table 5. Sediment impurities and barite abundances in coral calyces based on thin section inspection. Note that the observations of sediment impurities are qualitative: present (+) or absent (-). while barite abundances were graded into four arbitrary classes ranging from no barite (-) to relatively abundant barite (+++).

Thin-section ID	Sediments	Barite	Thin-section ID	Sediment	Barite
A13-1	-	-	VG30B-1	+	-
A13-2	-	-	VG30B-2	+	+
A13-3	-	-	VG30B-3	+	++
A13-4	-	-	VG30B-4	+	+
A13-5	-	-	VG31-1	+	-
A13-6	-	-	VG31-2	-	-
A13-7	-	-	VG31-3	+	++
A13-8	+	-	VG31-4	+	+
A14-1	-	-	VG31-4B	+	+
A14-2	+	-	VG31-5	+	+++
A14-3	+	-	VG31-5B	+	+++
A14-4	+	-	VG31-6	-	-
A14-5	+	-	VG33-1	+	-
A14-6	+	-	VG33-2	+	-
A16-1	-	-	VG33-3	+	+
A16-2	-	-	VG33-4	+	-
A16-3	-	-	VG33-5	+	+
A16-4	-	-	VG33-6	+	+
A16-5	-	-	VG36-1	-	-
A16-6	-	-	VG36-2	-	-
A16-7	-	-	VG36-3	+	-
VG30-1	+	+	VG36-4	-	-
VG30-2	+	-	VG36-5	+	-
VG30-3	+	-	VG36-6	+	-
VG30-4	+	+	VG36-7	+	-
VG30-5	+	+	VG50-1	+	-
VG30-6	+	+	VG50-2	+	-
VG30-7	+	-	VG50-3	+	+
VG30-8	+	++	VG50-4	+	+
VG30-9	+	-	VG50-5	-	-
			VG50-6	+	-

DISCUSSION

Limitations of the methodology

The majority of collected sediment cores contained sandy and gravelly sediments indicating that active sediment erosion and/or by-pass (transport) are the prevailing sedimentary processes at the seabed in the area. These high current velocity processes would certainly influence the geographic distribution of drilling mud components including barite in sediments, which in turn would complicate the straightforward use of sediment Ba concentration as a proxy for defining the primary impact area around the drilling site.

Clearly, the drilling activity can be traced in corals and sediments around the drilling site. Sand size barite crystals and elevated Ba concentrations in the sediments were found up to 4 km from the exploration drilling site. Fine-grained barite from the drilling mud is likely winnowed away from the study area due to high current velocities, hence the dispersal radius of fine-grained drilling mud components is plausibly considerably bigger. In the skeletons, however, the patterns of barite distribution were variable. No barite was detected in the skeletons from the samples from the easternmost (up-current) locations on reefs nearest to the drilling site (A13, A14), whereas the reference reef (VG50) around eight km to the NE of the drilling site contained barite. The largest concentration of barite was found in corals from the westernmost (down-current) part of the reef nearest to the exploration drilling site (VG30, VG31). The barite crystals in corals from down-current locations near the drilling site were bigger (< 60 μm) than those found in the reference reef (<10 μm). The occurrence of fine-grained barite in coral skeletons distant from the drilling site is consistent with the effective transport of fine-grained material in the study area.

One important finding of this study was that barite crystals do not seem to be incorporated in the skeleton to a great amount, but accumulate within the calices and other crevices in dead skeletons. Thus, the dead coral polyps represent time series of sediment entrapment, each covering a time interval from their death to present day. However, it has turned out that dating the death of corals is more difficult than counting its life span. In contrast to the growth of corals and generation of new polyps, which seems to be a rhythmic process, the death of corals may very well be episodic and sporadic.

Effects of drilling mud discharge

The presence of relatively coarse-grained sediments and drilling mud components in the coral polyps ca. 600 m down current from the drilling site signals the elevated turbulence and sediment supply during the drilling activity. This elevated sediment dispersion was likely to have an influence upon the coral reef at this distance from the drilling site. However, due to relatively short duration of the drilling campaign (ca. 7 months; 24.10.1992 - 18.02.1993 and 10 Sep – 12 Dec 1993) and strong currents that effectively dilute episodic sediment and drilling mud discharges, the damage was apparently not significant, and the reef recovered from this possible damage.

Interestingly, all the coral branches that deviate from the common relationship between life span and polyp generations (Figure 29) have calices containing relatively large barite grains. The normal rate of death (which must be assumed to balance the growth rate) may have been disturbed by increased sedimentation. As mentioned above, dating the death of these polyps has turned out to be difficult. However, if we assume that one new polyp is formed every year (as indicated in Figure 29), we can count backward, starting with the age of the youngest polyp (see Table 4) adding one year for each mother generation. If this is correct, polyp in thin-section VG31-5, which contained most barite, may have died around 1995. Polyps VG30-8 and VG30B-3 also contained relatively abundant barite. These have probably died after 1991 and 1997, respectively. Whether larger mineral grains can get trapped in the stomach of the polyps is not known. Furthermore, it is not known whether polyps would be affected negatively by having such grains in their stomachs.

The dataset available does not show dramatic signs of poor health status of reefs in the vicinity (600m) of the drilling site that can be related to the discharge of drilling waste. The reefs more distant from the drilling site, such as the ones at 3, 4 and 8 km distances studied here, have apparently been saved form any negative effects of the drilling activity. Further studies may, however, be needed to give a conclusive answer and to grade the danger zones around the drilling site. The discharge of the drilling waste took place periodically during a period of 7 months, and there is still the possibility that effects could have been more dramatic if the exposure time had been longer, e.g. if there had been continuous drilling of several production wells over a longer period of time.

Previous experiments have been carried out on tropical shallow water corals in field and laboratory (Thompson et al. 1980) with exposure to drilling fluids of different concentrations. Thompson et al (1980) found that none of seven studied species of corals died after three days of exposure to a drilling mud dilution of 10000:1. At a dilution of 1000:1, however, three species died. Exposure to drilling mud and normal carbonate mud in the field showed that drilling mud caused mortality quicker than natural mud.

The relevance of the results from impact studies carried out on tropical corals for the situation of cold water corals reefs on the Norwegian shelf may not be clear, as these are very different organisms and the environments are very different. The particle concentrations used in such experiments are also much higher than those the corals some hundreds meters away from a drilling site may be exposed to. Therefore, one might expect negative effects of weakly elevated concentrations of inorganic particles over a prolonged period to appear slowly over time. Maybe as a result of the imbalance in the energy budget of corals because they have to spend much time and energy to expel inedible particle they swallow mixed with the food.

ACKNOWLEDGEMENT

This project was funded by Norsk Hydro, Eni Norge, and Statoil. We would like to thank Jon Rytter Hasle, Hilde Espedal Arntsen and Ingunn Nilsen for fruitful discussions. Thanks to technicians at the laboratory at NGU, and to the captain and crew onboard RV G. O. Sars.

REFERENCES

Appleby, P.G. 2000. Radiometric dating of sediment records in European mountain lakes. Limnology, 59: 1-14.

Appleby, P.G. 2001. Chronostratigraphic techniques in recent sediments. In: Last, W.M. and Smol, J.P. (eds). Tracking Environmental Change Using Lake Sediments. Volume 1 - Basin Analysis. Coring and Chronological Techniques. Kluwer. Pp 171-203.

Church, T.M. 1979. Marine barite. In: Burns, R.G. (ed). Marine Minerals. Mineralogical Society of America. Reviews in Mineralology, 6: 170-210.

Croudace, I.W., Rindby, A., Rothwell, R.G. 2006. ITRAX: description and evaluation of a new X-ray core scanner. In: R.G. Rothwell (ed.) New Ways of Looking at Sediment Cores and Core Data. The Geolocial Society Special Publications, London, in press.

Dehairs, F., Chesselet, R.., Jedwab, J. 1980. Discrete suspended particles of barite and the barium cycle in the ocean. Earth and Planetary Science Letters, 49: 528-550.

Deslarzes, K.J.P., Boothe, P.N., Presley, B.J., Steinmetz, G.L. 1995. Historical incorporation of barium in the reef building coral Montastrea annularis at the Flower Garden Banks. north-west Gulf of Mexico. Marine Pollution Bulletin, 30: 718-722.

Guzman, H.M.., Jarvis, K.E. 1996. Vanadium century record from Caribbean reef corals: A tracer of oil pollution in Panama. Ambio, 35: 523-526.

Law, A.T., Readman, J.W., Tolosa, I., Bartolucci, J. 1994. Distribution of hydrocarbons and sterols in coral: A preliminary study. NRCT-JSPS Joint Seminar on Marine Science. Songkhla (Thailand), 2-3 Dec 1993.

Lepland, A., Sæther, O., Thorsnes, T. 2000. Accumulation of barium in recent Skagerrak sediments: sources and distribution controls. Marine Geology, 163: 13-26.

Molvær, J., Knutzen, J., Magnusson, J., Rygg, B., Skei, J. and Sørensen, J. 1997. Environmental quality classification in fjords and coastal areas. Statens Forurensningstilsyn TA-1467. Norway. 36 pp.

Mortensen, P.B., Roberts, J.M., Sundt, R.C. 2000. Video-assisted grabbing: a minimally destructive method of sampling azooxanthellate coral banks. Journal of the Marine Biological Association of the UK, 80:365-366.

Mortensen. P.B., Rapp, H.T. 1998. Oxygen- and carbon isotope ratios related to growth line patterns in skeletons of Lophelia pertusa (L) (Anthozoa: Scleractinia): Implications for determination of linear extension rates. Sarsia, 83:433-446.

Poulain, P.M., Warn Varnas, A., Niiler, P.P. 1996. Near-surface circulation of the Nordic seas as measured by Lagrangian drifters. Journal of Geophysical Research, 101: 18237-18258.

Readman. J.W., Tolosa, I., Law, A.T., Bartocci, J., Azemard, S., Hamilton, T., Mee, L.D., Wagener, A. Le Tissier, M., Roberts, C., Downing, N., Price, A.R.G. 1996. Discrete bands of petroleum hydrocarbons and molecular organic markers identified within massive coral skeletons. Marine Pollution Bulletin, 32: 437-443.

Rye. H. 1996. Miljøeffekter av utslipp av borekjemikalier. IKU Petroleumsforskning. Rapport nr. 42.4053.00/01/96. 98 pp.

Thompson, J.H., Shinn, E.A., Bright, T.J. 1980. Effects of drilling mud on seven species of reef-building corals as measured in the field and laboratory. In: Geyer, R.A. (ed.) Marine Environmental Pollution. Vol. 1—Hydrocarbons. Elsevier. Amsterdam. Pp. 433–453.

Trefry, J.H., Trocine, R.P., Meyer, D.B. 1981. Tracing the Fate of Petroleum Drilling Fluids in the Northwest Gulf of Mexico. The Ocean - An International Workplace. Oceans 81 Conference Record – Boston, Massachusetts, 16-18 September 1981, 2: 732-736.

APPENDIX 1. Narrative of cruise and list of sampled and inspected locations. Positions are given as decimal degrees.

Time	Activity	Gear	Sample no	Latitude	Longitude	Depth
Friday 18.06.						
2:14	Deployment of current meter at the Northern reference location.	Current meter	13504	66.96350	11.08617	301
3:50	---------- " ----------	Current meter	13499	66.88333	11.16883	299
4:57	Deployment of current meter at the drilling site	Current meter	10444	66.92950	10.93950	308
6:00	Inspection of *Lophelia* reef	ROV Aglantha	A09	66.92310	10.89820	309
8:47	Inspection near drilling site	ROV Aglantha	A10	66.92310	10.89820	310
10:57	Deployment of multicorer	Multicorer	M8L7	66.92267	10.90500	308
12:12	Deployment of multicorer	Multicorer	M8L9	66.92533	10.90383	309
15:42	Sampling of dead *Lophelia*	Video grab	R8L23	66.92347	10.89112	301
15:42	Sampling of dead and live *Lophelia*	Video grab	R8L24	66.92332	10.89710	302
17:51	Deployment of multicorer	Multicorer	M8L10	66.92267	10.89950	308
18:08	Deployment of multicorer	Multicorer	M8L12	66.92267	10.89950	308
18:19	ROV dive on *Lophelia* reef	ROV Aglantha	A11	66.92310	10.89820	309
22:54	Sampling of dead *Lophelia*	Video grab	R8L25	66.90672	10.89003	302
Saturday 19.06.						
0:42	Two attempts to sample *Lophelia*. Aborted	Video grab		66.92383	10.89683	305
4:08	Sampling of live and dead *Lophelia*	Video grab	R8L26	66.90687	10.88950	296
4:59	---------- " ----------	Video grab	R8L27	66.90687	10.88930	296
7:03	ROV dive. Sampling of live *Lophelia*	ROV Aglantha	A12	66.92322	10.89353	302
8:20	ROV dive. Sampling of live *Lophelia*	ROV Aglantha	A13	66.92323	10.89342	302
9:46	Deployment of multicorer	Multicorer	M8L13	66.92233	10.87617	318
11:27	---------- " ----------	Multicorer	M8L14	66.92150	10.84917	320
11:54	---------- " ----------	Multicorer	M8L15	66.92162	10.85669	322
12:51	---------- " ----------	Multicorer	M8L16	66.91150	10.85050	332
13:46	---------- " ----------	Multicorer	M8L17	66.92467	10.82817	329
14:00	---------- " ----------	Multicorer	M8L18	66.92450	10.82933	329
15:16	Deployment of video grab. Aborted.	Video grab	R8L28	66.92333	10.89333	297
17:43	Sampling of live *Lophelia*	ROV Aglantha	A14	66.92350	10.88970	305
20:58	Inspection of *Lophelia* reef	ROV Aglantha	A15	66.91997	10.99105	316
20:58	Sampling of live *Lophelia*	ROV Aglantha	A16	66.92095	10.99150	312
23:35	---------- " ----------	Video grab	R8L29	66.90765	10.83228	328
Sunday 20.06.						
1:37	Sampling of live and dead *Lophelia*	Video grab	R8L30	66.90708	10.83322	327
3:36	Sampling of dead *Lophelia*	Video grab	R8L31	66.90758	10.83280	327
5:04	Sampling of live and dead *Lophelia*	Video grab	R8L32	66.90727	10.83297	322
6:24	Deployment of multicorer	Multicorer	M8L19	66.89600	10.83317	339

Appendix 1 (Cont.)

Time	Activity	Gear	Sample no	Latitude	Longitude	Depth
7:08	Deployment of multicorer	Multicorer	M8L20	66.93100	10.87900	307
7:28	---------- " ----------	Multicorer	M8L21	66.93117	10.88017	307
8:04	---------- " ----------	Multicorer	M8L22	66.93600	10.92667	313
8:56	---------- " ----------	Multicorer	M8L23	66.92533	10.93150	314
9:18	---------- " ----------	Multicorer	M8L24	66.92533	10.93150	314
9:51	---------- " ----------	Multicorer	M8L25	66.92533	10.97233	323
11:36	---------- " ----------	Multicorer	M8L26	66.89717	10.91617	343
11:57	---------- " ----------	Multicorer	M8L27	66.89717	10.91617	343
13:58	---------- " ----------	Multicorer	M8L28	66.91800	10.90567	311
14:06	CTD	CTD	336	66.91807	10.90567	311
16:33	Other project until Wednesday 23.06.			66.96800	11.13800	327
Wednesday 23.06.						
10:11	Recovery of current meter at the Southeastern reference location.	Current meter	13499	66.88333	11.16883	299
11:30	Recovery of current meter at the drilling site	Current meter	10444	66.92950	10.93950	308
12:50	Recovery of current meter at the Northern reference location	Current meter	13504	66.96350	11.08617	301
21:54	Other project for the rest of the cruise					
Thursday 24.06.						
9:00	Steaming for Bodø. End of cruise.					

APPENDIX 2. Core inventory. Specifications given in the "remarks" column indicate the type of analyses undertaken on cores

Station	Core ID	Core diameter (mm)	Core length (cm)	Remarks
Station1	C001	63	4	grain size
Station2	C002	63	ca. 25	stored
	C003	63	ca. 25	stored
	C004	63	ca. 25	core logging, geochemistry
	C005	110	23	mineral separation
	C006	110	28	dating
	C007	110	15	grain size
Station3	C008	63	3	subsampled, stored
	C009	63	3	subsampled, stored
	C010	63	3	subsampled, stored
	C011	110	5	grain size
	C012	110	4	subsampled, stored
Station 4	C013	63	ca.15	dating, mineral separation, grain size
	C014	63	ca.15	stored
	C015	63	ca. 15	stored
	C016	63	ca. 15	stored
	C017	63	ca.15	core logging, geochemistry
Station 5	C018	63	ca. 12	stored
	C019	63	ca. 12	stored
	C020	63	ca. 12	core logging, geochemistry
	C021	110		dating, grain size
	C022	110		mineral separation
Station 6	C023	63	ca. 11	stored
	C024	63	ca.11	stored
	C025	63	ca. 11	core logging, geochemistry
	C026	110	11	dating, grain size
	C027	110	11	mineral separation
Station 7	C028	63	ca. 10	stored
	C029	63	ca.10	stored
	C030	63	ca. 10	core logging, geochemistry
	C031	110	9	dating, grain size
	C032	110	9	subsampled, stored
Station 8	C033	63	ca. 20	stored
	C034	63	ca. 20	stored
	C035	63	ca. 20	core logging, geochemistry
	C036	110	19	mineral separation
	C037	110	21	grain size
	C038	63	ca. 20	stored
Station 9	C039	63	ca. 25	stored
	C040	63	ca. 25	stored
	C041	63	ca. 25	core logging, geochemistry
	C042	63	0	
	C043	110	23	mineral separation, grain size
Station10	C044	63	ca. 25	stored
	C045	63	ca. 25	stored
	C046	63	ca. 25	core logging, geochemistry
	C047	110	21	grain size
	C048	63	ca. 25	stored

Appendix 2 (Cont.).

Station	Core ID	Core diameter (mm)	Core length (cm)	Remarks
Station 11	C049	63	ca. 5	geochemistry
	C050	63	4	
	C051	63	3	grain size
	C052	110	5	mineral separation
Station 12	C053	63	ca. 20	stored
	C054	63	ca. 20	stored
	C055	63	ca. 20	stored
	C056	63	ca. 20	core logging, geochemistry
	C057	110	23	dating, grain size
Station 13	C058	63	ca. 25	stored
	C059	63	ca. 25	stored
	C060	63	ca. 25	core logging, geochemistry
	C061	110	21	mineral separation, grain size
Station 14	C062	63	ca. 25	stored
	C063	63	ca. 25	stored
	C064	63	ca. 25	core logging, geochemistry
	C065	63	ca. 25	stored
	C066	110	23	dating, grain size
Station 15	C067	63	ca. 15	stored
	C068	63	ca. 15	stored
	C069	63	ca. 15	core logging, geochemistry
	C070	110	12	grain size
Station 16	C071	63	ca. 15	stored
	C072	63	ca. 15	stored
	C073	63	ca. 15	stored
	C074	63	ca. 15	core logging, geochemistry
	C075	110	15	grain size
Station 17	C076	63	ca. 30	stored
	C077	63	ca. 30	stored
	C078	63	ca. 30	stored
	C079	63	ca. 30	core logging, geochemistry
	C080	110	25	dating, grain size
Station 18	C081	63	ca. 25	stored
	C082	63	ca. 25	stored
	C083	63	ca. 25	stored
	C084	63	ca. 25	core logging, geochemistry
	C085	110	21	dating, grain size
Station 19	C086	63	ca. 25	core logging, geochemistry
	C087	63	ca. 25	stored
	C088	63	ca. 25	core splitting test, discarded
	C089	63	ca. 25	stored
	C090	110	25	grain size
Station 20	C091	63	ca. 20	stored
	C092	63	ca. 20	core logging, geochemistry
	C093	63	ca. 20	stored
	C094	63	ca. 10	stored
	C095	63	19	dating, grain size

Appendix 3. Cumulative grain-size distribution plots and statistical characteristics of individual samples. Note that sample IDs show the core numbers and subsampling intervals, i.e. ID C001_0-4 stands for a subsample collected from 0-4 cm depth interval of Core 001.

NGU

COULTER® LS Particle Size Analyzer

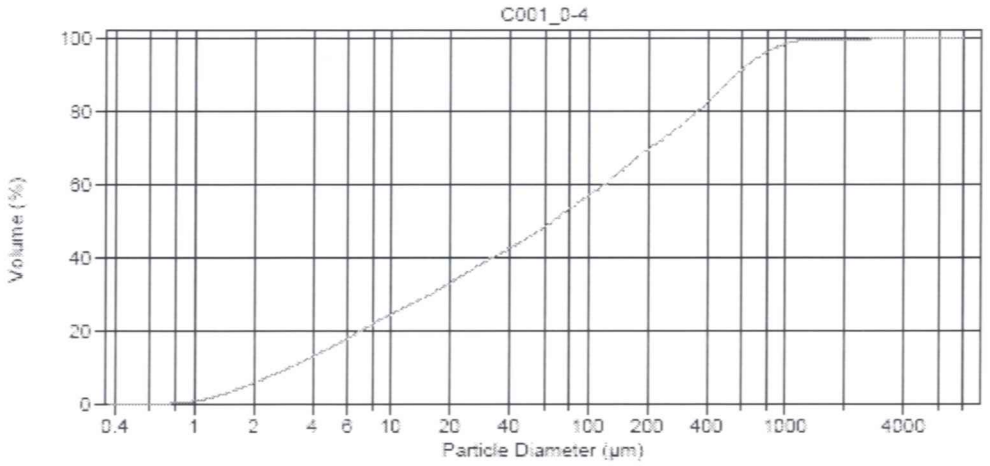

Volume Statistics (Arithmetic) c001#a.$02

Calculations from 0.375 µm to 8000 µm

Volume	100.0%		
Mean:	198.4 µm	95% Conf. Limits:	0-921.7 µm
Median:	66.59 µm	S.D.:	369.0 µm
D(3,2):	9.932 µm	Variance:	136174 µm^2
Mean/Median Ratio:	2.980	C.V.:	186%
Mode:	471.1 µm	Skewness:	8.097 Right skewed
d_{10}:	3.086 µm	Kurtosis:	107.0 Leptokurtic
d_{50}:	66.59 µm		
d_{90}:	562.5 µm		
Specific Surf. Area	6041 cm^2/ml		

% <	10	20	50	75	90
Size µm	3.086	6.992	66.59	276.0	562.5

c001#a.$02

Particle Diameter µm	Volume % <	Particle Diameter µm	Volume % <
2.000	5.70	8000	100
5.000	15.6		
10.00	24.6		
15.00	29.2		
20.00	33.2		
50.00	45.6		
60.00	48.3		
63.00	49.1		
70.00	50.9		
75.00	52.0		
90.00	55.1		
125.0	60.6		
200.0	69.4		
250.0	73.2		
400.0	82.4		
500.0	87.4		
1000	98.3		
2000	99.6		
4000	99.8		

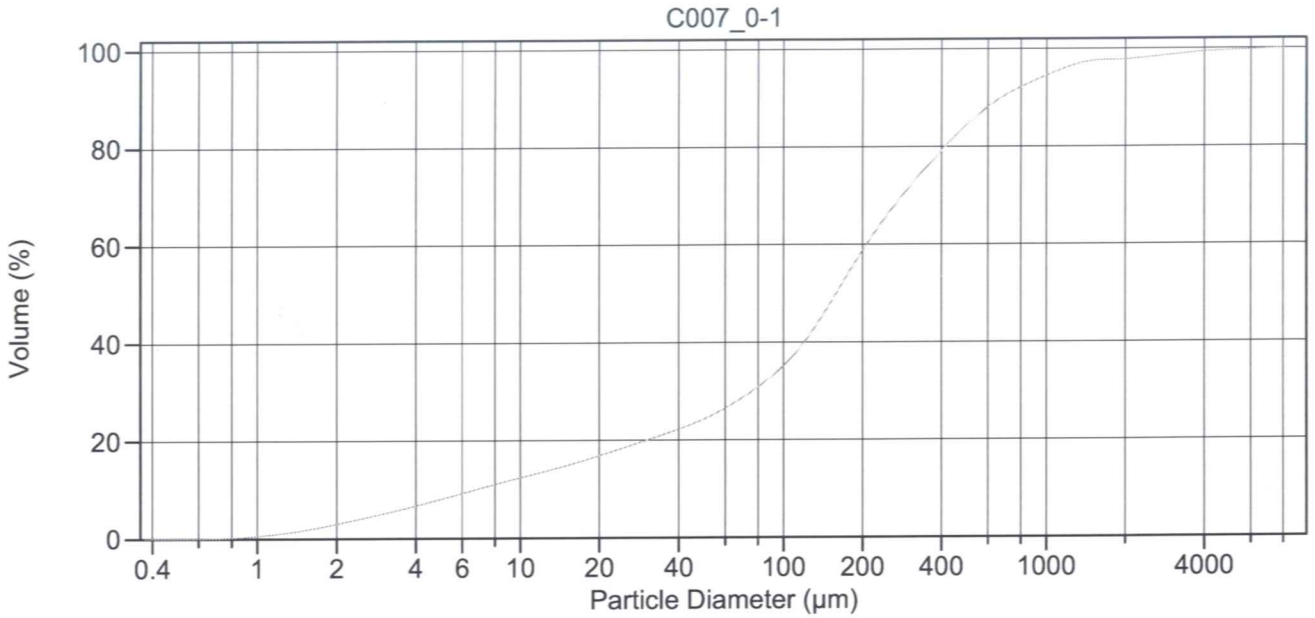

Volume Statistics (Arithmetic) c007a.$02

Calculations from 0.375 µm to 8000 µm

Volume	100.0%		
Mean:	316.4 µm	95% Conf. Limits:	0-1483 µm
Median:	158.8 µm	S.D.:	595.3 µm
D(3,2):	17.88 µm	Variance:	354368 µm^2
Mean/Median Ratio:	1.992	C.V.:	188%
Mode:	168.8 µm	Skewness:	5.678 Right skewed
d_{10}:	6.784 µm	Kurtosis:	41.32 Leptokurtic
d_{50}:	158.8 µm		
d_{90}:	673.8 µm		
Specific Surf. Area	3356 cm^2/ml		

% <	10	20	50	75	90
Size µm	6.784	30.25	158.8	339.9	673.8

c007a.$02

Particle Diameter µm	Volume % <	Particle Diameter µm	Volume % <
2.000	3.00	8000	100
5.000	8.04		
10.00	12.4		
15.00	14.8		
20.00	16.8		
50.00	24.3		
60.00	26.5		
63.00	27.1		
70.00	28.7		
75.00	29.7		
90.00	32.9		
125.0	41.3		
200.0	58.7		
250.0	66.2		
400.0	79.2		
500.0	84.5		
1000	94.5		
2000	97.8		
4000	99.4		

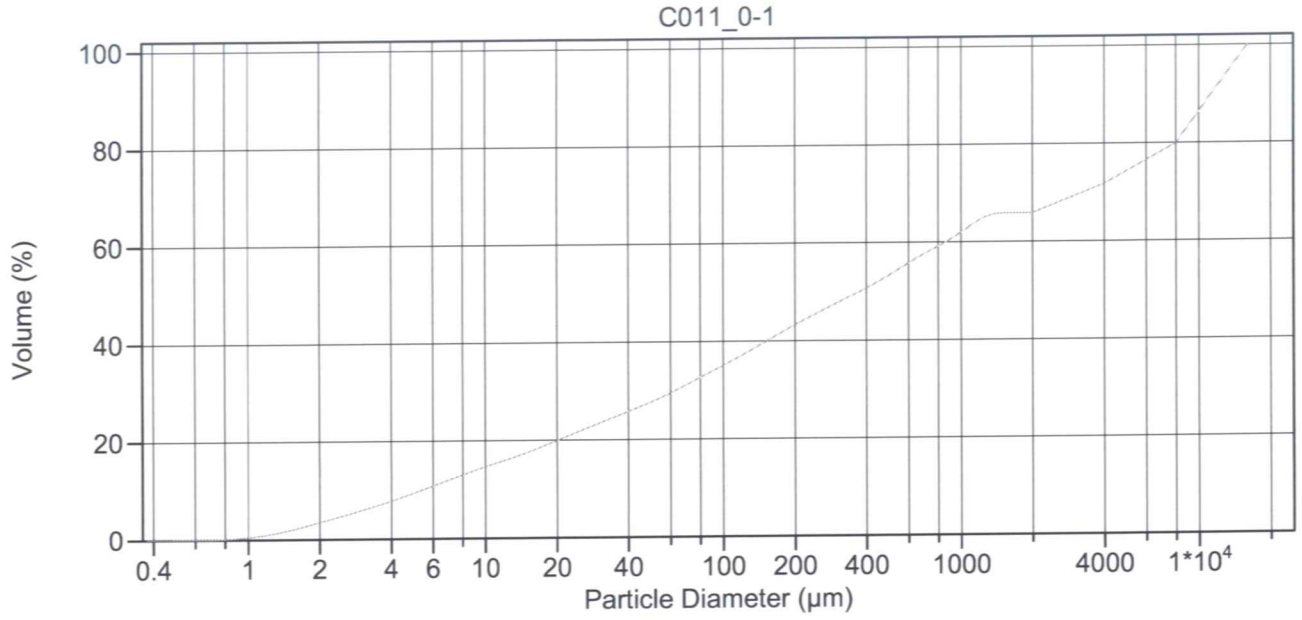

Volume Statistics (Arithmetic) c011#a.$02

Calculations from 0.375 µm to 16000 µm

Volume	100.0%		
Mean:	3061 µm	95% Conf. Limits:	0-11723 µm
Median:	374.6 µm	S.D.:	4419 µm
D(3,2):	16.36 µm	Variance:	19529588 µm^2
Mean/Median Ratio:	8.172	C.V.:	144%
Mode:	11314 µm	Skewness:	1.147 Right skewed
d_{10}:	5.422 µm	Kurtosis:	-0.431 Platykurtic
d_{50}:	374.6 µm		
d_{90}:	12018 µm		
Specific Surf. Area	3667 cm^2/ml		

% <	10	20	50	75	90
Size µm	5.422	20.18	374.6	5584	12018

c011#a.$02

Particle Diameter µm	Volume % <	Particle Diameter µm	Volume % <
2.000	3.48	8000	79.9
5.000	9.38		
10.00	14.6		
15.00	17.5		
20.00	19.9		
50.00	27.7		
60.00	29.5		
63.00	30.0		
70.00	31.1		
75.00	31.9		
90.00	33.9		
125.0	37.6		
200.0	43.2		
250.0	45.7		
400.0	50.7		
500.0	53.4		
1000	62.0		
2000	65.9		
4000	71.8		

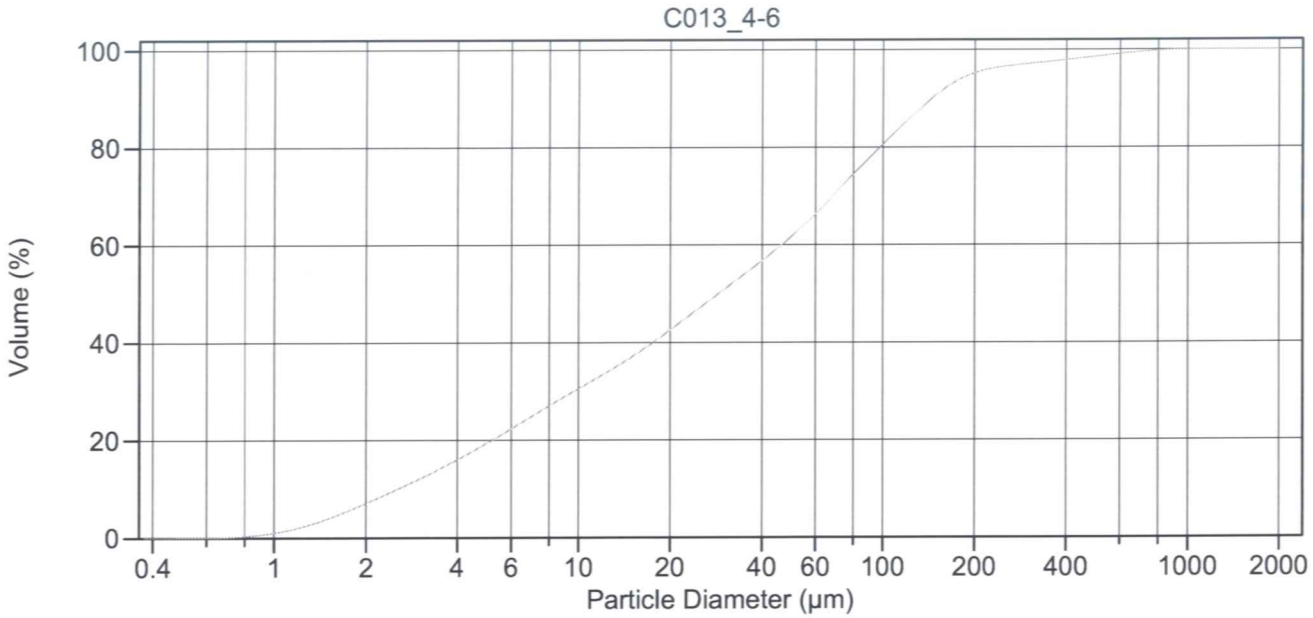

Volume Statistics (Arithmetic) c013.$02

Calculations from 0.375 µm to 2000 µm

Volume	100.0%		
Mean:	62.62 µm	95% Conf. Limits:	0-257.5 µm
Median:	28.83 µm	S.D.:	99.41 µm
D(3,2):	7.823 µm	Variance:	9883 µm^2
Mean/Median Ratio:	2.172	C.V.:	159%
Mode:	72.95 µm	Skewness:	4.095 Right skewed
d_{10}:	2.545 µm	Kurtosis:	22.28 Leptokurtic
d_{50}:	28.83 µm		
d_{90}:	144.5 µm		
Specific Surf. Area	7669 cm^2/ml		

% <	10	20	50	75	90
Size µm	2.545	5.208	28.83	81.59	144.5

c013.$02

Particle Diameter µm	Volume % <	Particle Diameter µm	Volume % <
2.000	7.10	8000	100
5.000	19.4		
10.00	30.5		
15.00	37.0		
20.00	42.6		
50.00	61.7		
60.00	66.3		
63.00	67.7		
70.00	70.7		
75.00	72.6		
90.00	77.7		
125.0	86.4		
200.0	95.2		
250.0	96.6		
400.0	97.9		
500.0	98.6		
1000	100.0		
2000	100		
4000	100		

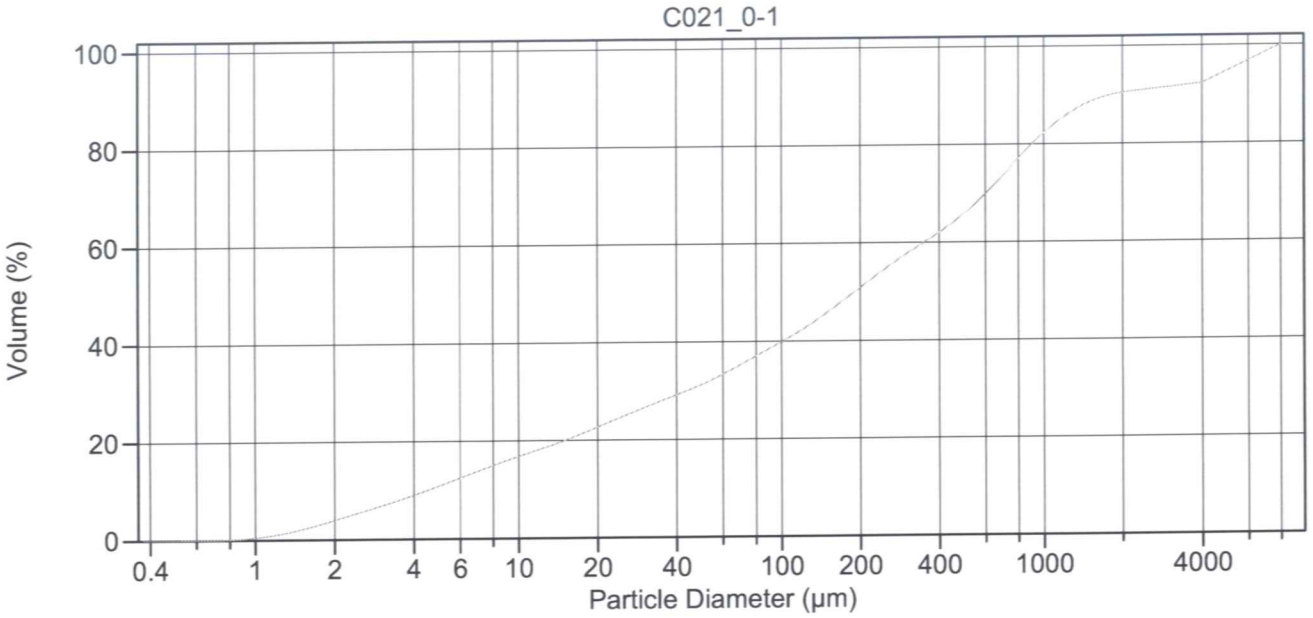

Volume Statistics (Arithmetic) c021#a.$02

Calculations from 0.375 µm to 8000 µm

Volume	100.0%		
Mean:	789.7 µm	95% Conf. Limits:	0-3725 µm
Median:	190.5 µm	S.D.:	1498 µm
D(3,2):	14.33 µm	Variance:	2243248 µm^2
Mean/Median Ratio:	4.145	C.V.:	190%
Mode:	5657 µm	Skewness:	2.628 Right skewed
d_{10}:	4.527 µm	Kurtosis:	5.686 Leptokurtic
d_{50}:	190.5 µm		
d_{90}:	1803 µm		
Specific Surf. Area	4188 cm^2/ml		

% <	10	20	50	75	90
Size µm	4.527	15.01	190.5	736.3	1803

c021#a.$02

Particle Diameter µm	Volume % <	Particle Diameter µm	Volume % <
2.000	3.96	8000	100
5.000	10.9		
10.00	16.8		
15.00	20.0		
20.00	22.7		
50.00	31.3		
60.00	33.3		
63.00	33.9		
70.00	35.2		
75.00	36.1		
90.00	38.5		
125.0	42.9		
200.0	50.8		
250.0	54.7		
400.0	62.0		
500.0	66.0		
1000	82.2		
2000	90.5		
4000	92.3		

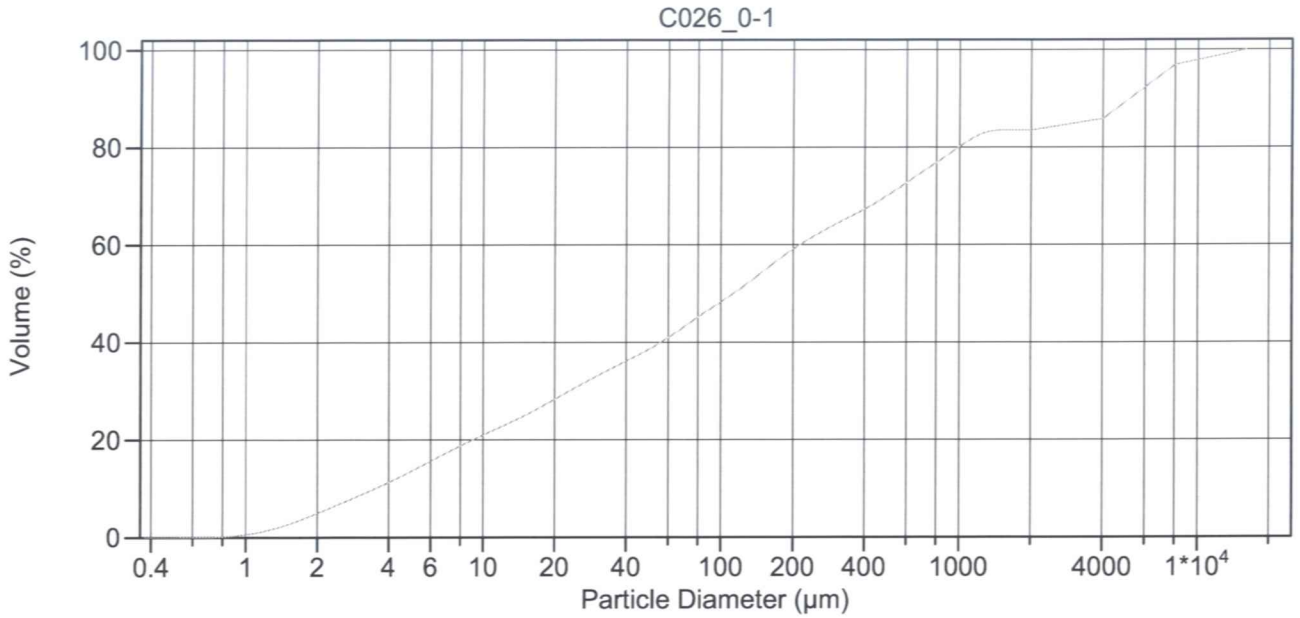

Volume Statistics (Arithmetic) c026#a.$02

Calculations from 0.375 µm to 16000 µm

Volume	100.0%		
Mean:	1219 µm	95% Conf. Limits:	0-6153 µm
Median:	113.0 µm	S.D.:	2517 µm
D(3,2):	11.59 µm	Variance:	6336537 µm^2
Mean/Median Ratio:	10.79	C.V.:	207%
Mode:	5657 µm	Skewness:	2.552 Right skewed
d_{10}:	3.518 µm	Kurtosis:	6.147 Leptokurtic
d_{50}:	113.0 µm		
d_{90}:	5508 µm		
Specific Surf. Area	5177 cm^2/ml		

% <	10	20	50	75	90
Size µm	3.518	9.041	113.0	703.2	5508

c026#a.$02

Particle Diameter µm	Volume % <	Particle Diameter µm	Volume % <
2.000	4.94	8000	96.9
5.000	13.6		
10.00	21.0		
15.00	25.0		
20.00	28.3		
50.00	38.6		
60.00	40.9		
63.00	41.6		
70.00	43.2		
75.00	44.2		
90.00	46.8		
125.0	51.6		
200.0	59.1		
250.0	62.0		
400.0	67.3		
500.0	70.1		
1000	80.1		
2000	83.5		
4000	85.8		

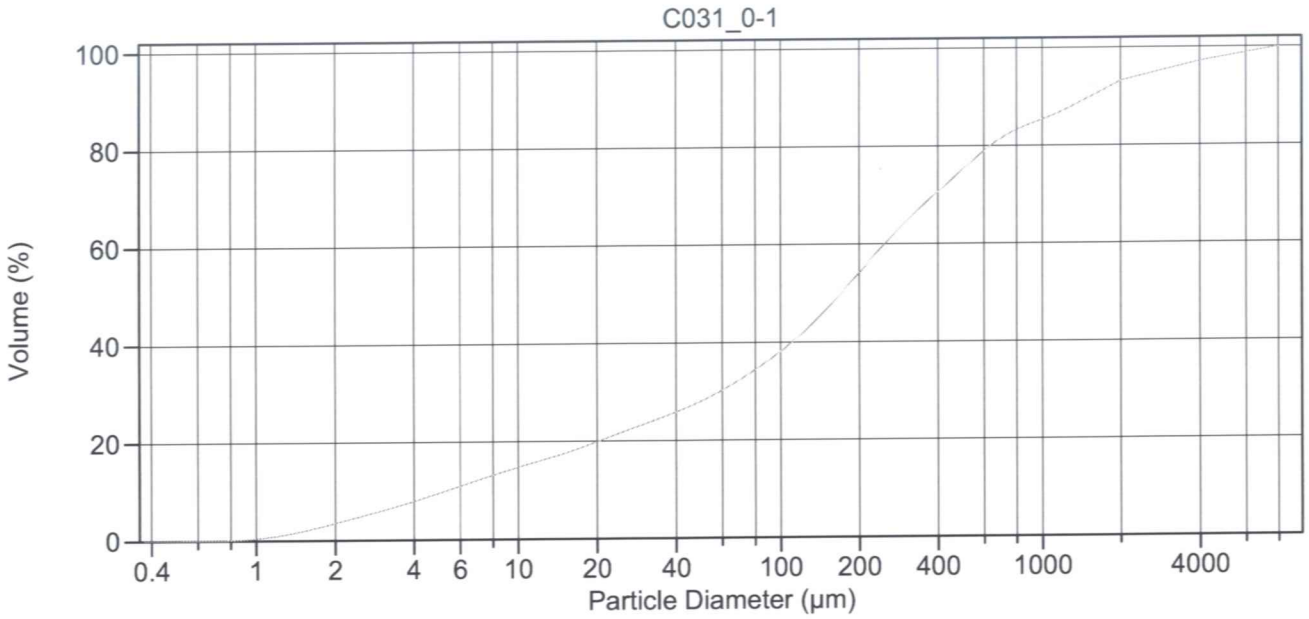

Volume Statistics (Arithmetic) c031a.$02

Calculations from 0.375 µm to 8000 µm

Volume	100.0%		
Mean:	558.3 µm	95% Conf. Limits:	0-2670 µm
Median:	170.9 µm	S.D.:	1078 µm
D(3,2):	15.97 µm	Variance:	1161140 µm^2
Mean/Median Ratio:	3.267	C.V.:	193%
Mode:	2828 µm	Skewness:	3.372 Right skewed
d_{10}:	5.317 µm	Kurtosis:	12.05 Leptokurtic
d_{50}:	170.9 µm		
d_{90}:	1533 µm		
Specific Surf. Area	3757 cm^2/ml		

% <	10	20	50	75	90
Size µm	5.317	20.26	170.9	494.4	1533

c031a.$02

Particle Diameter µm	Volume % <	Particle Diameter µm	Volume % <
2.000	3.51	8000	100
5.000	9.53		
10.00	14.7		
15.00	17.5		
20.00	19.9		
50.00	28.1		
60.00	30.2		
63.00	30.9		
70.00	32.4		
75.00	33.4		
90.00	36.3		
125.0	42.5		
200.0	54.1		
250.0	60.0		
400.0	70.6		
500.0	75.2		
1000	85.3		
2000	93.2		
4000	97.2		

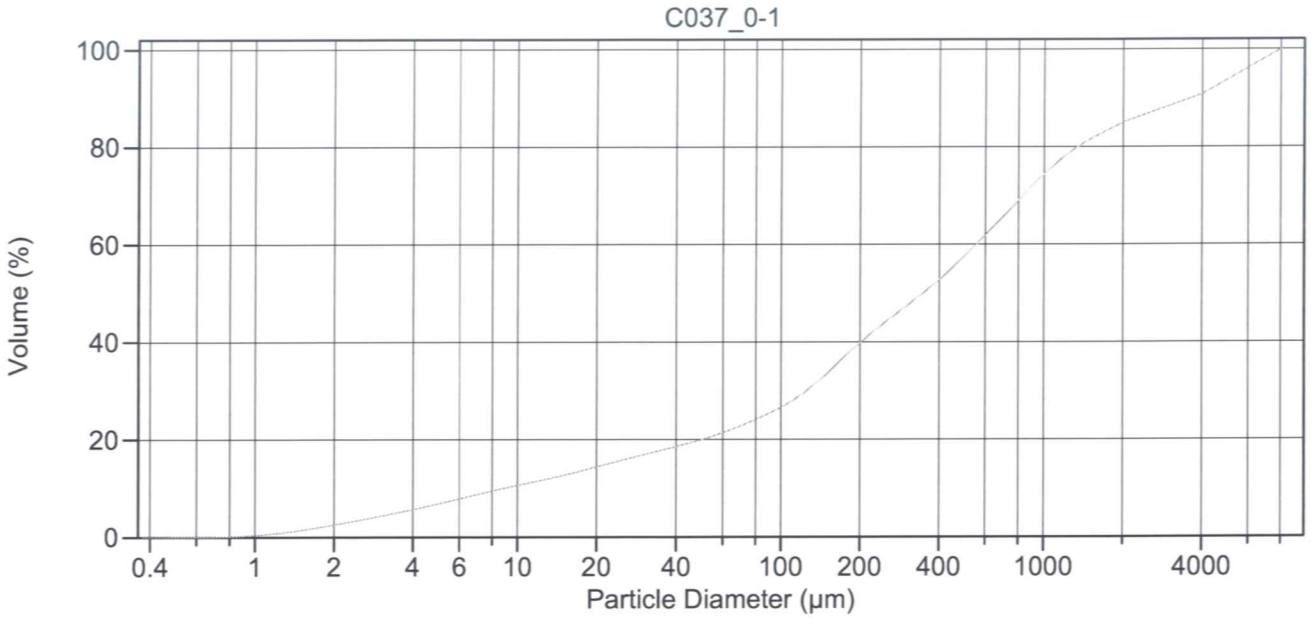

Volume Statistics (Arithmetic) c037a.$02

Calculations from 0.375 µm to 8000 µm

Volume	100.0%		
Mean:	1039 µm	95% Conf. Limits:	0-4235 µm
Median:	347.5 µm	S.D.:	1631 µm
D(3,2):	21.73 µm	Variance:	2658547 µm^2
Mean/Median Ratio:	2.990	C.V.:	157%
Mode:	5657 µm	Skewness:	2.072 Right skewed
d_{10}:	8.868 µm	Kurtosis:	3.074 Leptokurtic
d_{50}:	347.5 µm		
d_{90}:	3730 µm		
Specific Surf. Area	2761 cm^2/ml		

% <	10	20	50	75	90
Size µm	8.868	50.08	347.5	1031	3730

c037a.$02

Particle Diameter µm	Volume % <	Particle Diameter µm	Volume % <
2.000	2.54	8000	100
5.000	6.84		
10.00	10.6		
15.00	12.7		
20.00	14.4		
50.00	20.0		
60.00	21.4		
63.00	21.8		
70.00	22.8		
75.00	23.4		
90.00	25.3		
125.0	29.9		
200.0	39.8		
250.0	44.0		
400.0	52.7		
500.0	57.5		
1000	74.3		
2000	85.0		
4000	90.8		

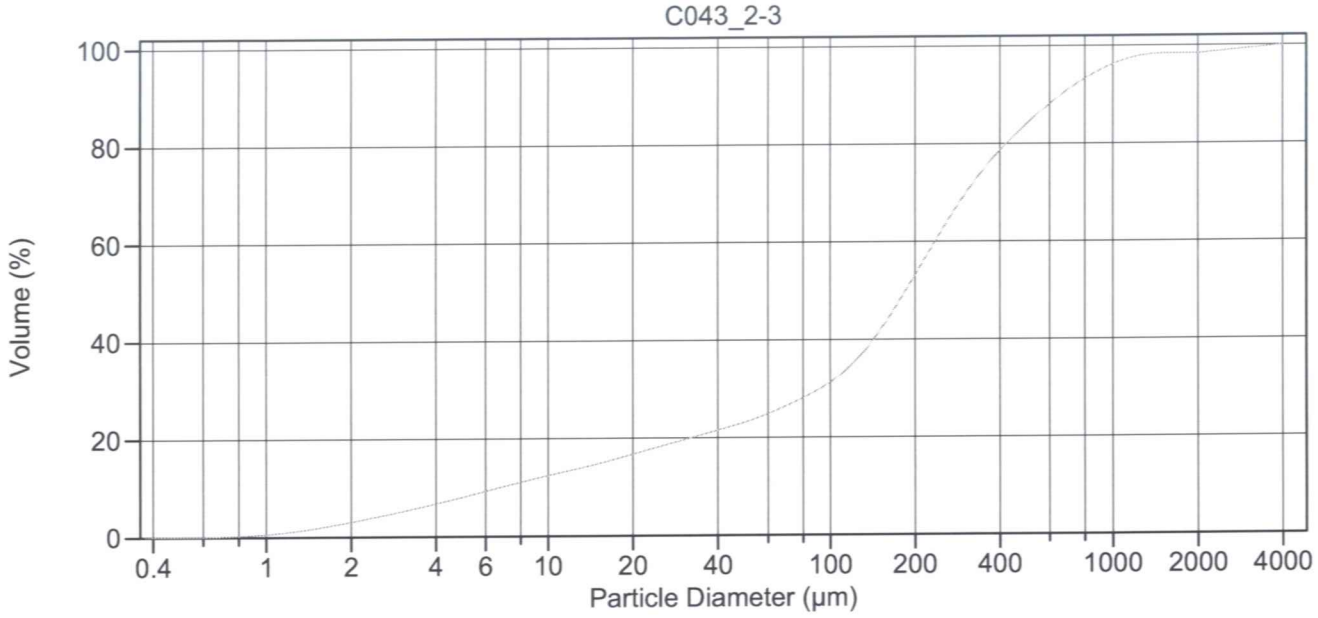

Volume Statistics (Arithmetic) c043a.$02

Calculations from 0.375 µm to 4000 µm

Volume	100.0%		
Mean:	292.4 µm	95% Conf. Limits:	0-1099 µm
Median:	185.7 µm	S.D.:	411.6 µm
D(3,2):	17.85 µm	Variance:	169412 µm^2
Mean/Median Ratio:	1.574	C.V.:	141%
Mode:	203.5 µm	Skewness:	4.016 Right skewed
d_{10}:	6.728 µm	Kurtosis:	20.79 Leptokurtic
d_{50}:	185.7 µm		
d_{90}:	659.6 µm		
Specific Surf. Area	3362 cm^2/ml		

% <	10	20	50	75	90
Size µm	6.728	32.08	185.7	353.0	659.6

c043a.$02

Particle Diameter µm	Volume % <	Particle Diameter µm	Volume % <
2.000	3.04	8000	100
5.000	8.10		
10.00	12.4		
15.00	14.8		
20.00	16.7		
50.00	23.2		
60.00	24.9		
63.00	25.4		
70.00	26.5		
75.00	27.3		
90.00	29.7		
125.0	36.0		
200.0	53.1		
250.0	62.5		
400.0	78.6		
500.0	84.2		
1000	96.2		
2000	98.4		
4000	100		

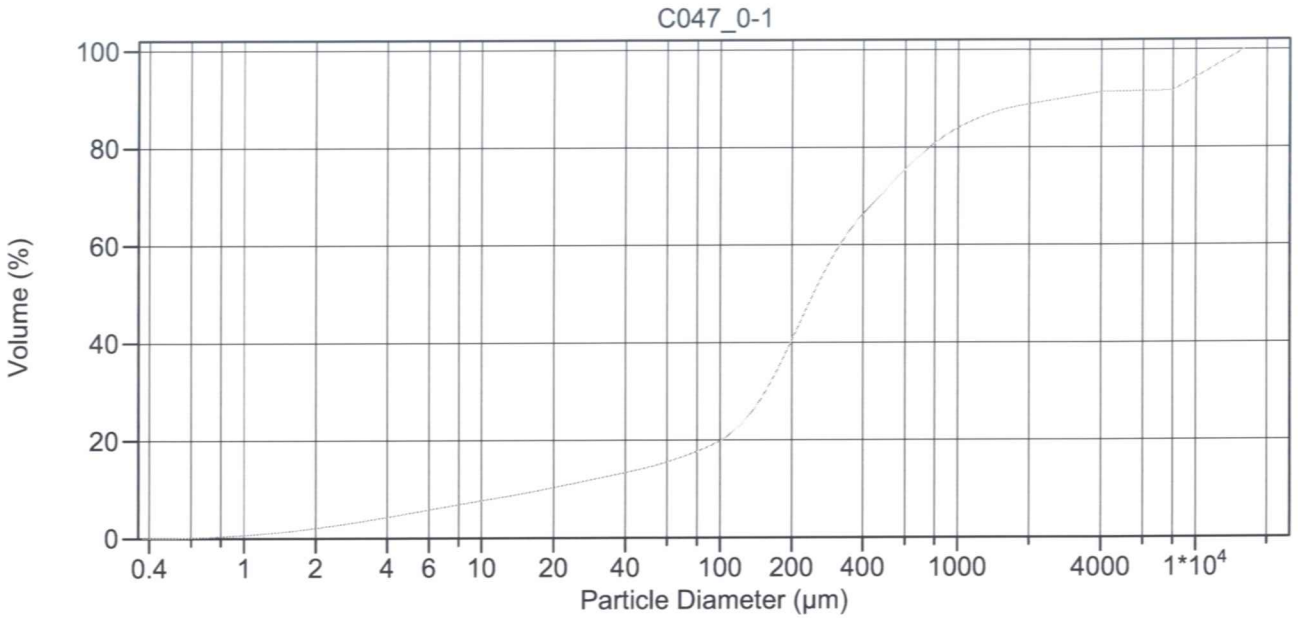

Volume Statistics (Arithmetic) c047#a.$02

Calculations from 0.375 µm to 16000 µm

Volume	100.0%		
Mean:	1318 µm	95% Conf. Limits:	0-7342 µm
Median:	246.9 µm	S.D.:	3074 µm
D(3,2):	25.55 µm	Variance:	9447086 µm^2
Mean/Median Ratio:	5.338	C.V.:	233%
Mode:	11314 µm	Skewness:	2.848 Right skewed
d_{10}:	18.58 µm	Kurtosis:	6.378 Leptokurtic
d_{50}:	246.9 µm		
d_{90}:	2920 µm		
Specific Surf. Area	2348 cm^2/ml		

% <	10	20	50	75	90
Size µm	18.58	101.0	246.9	589.8	2920

c047#a.$02

Particle Diameter µm	Volume % <	Particle Diameter µm	Volume % <
2.000	2.08	8000	91.6
5.000	5.10		
10.00	7.67		
15.00	9.13		
20.00	10.3		
50.00	14.4		
60.00	15.5		
63.00	15.9		
70.00	16.6		
75.00	17.2		
90.00	18.7		
125.0	23.7		
200.0	40.5		
250.0	50.6		
400.0	66.3		
500.0	71.4		
1000	83.9		
2000	88.9		
4000	91.4		

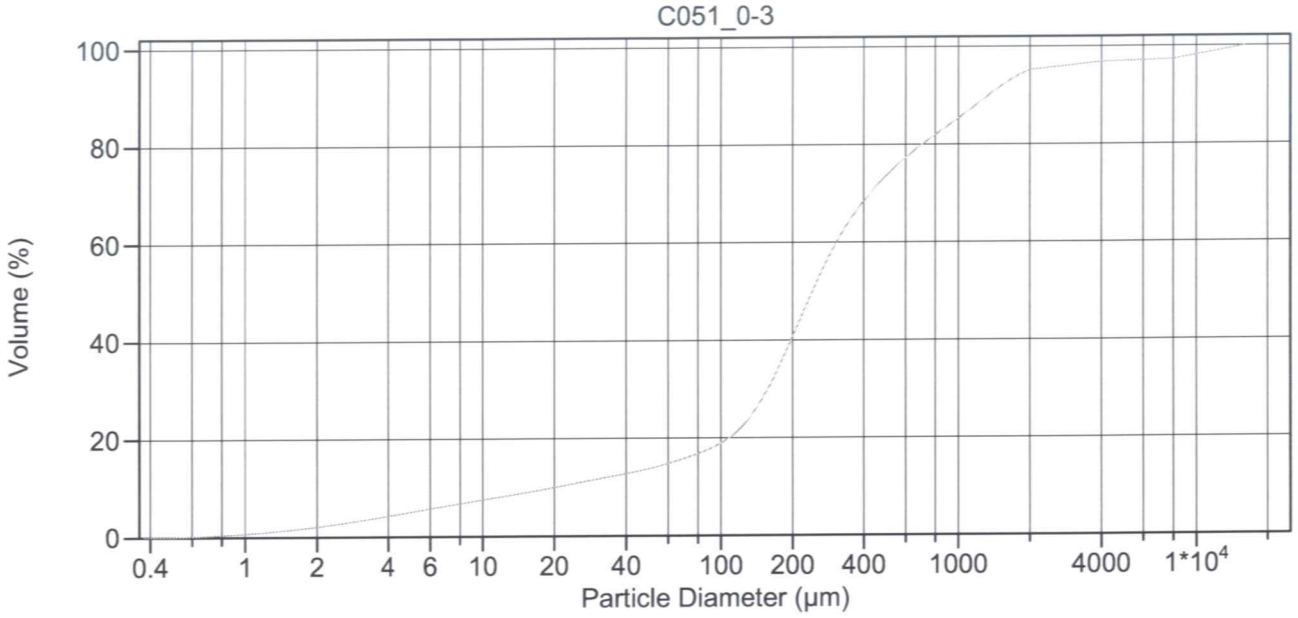

Volume Statistics (Arithmetic) c051a.$02

Calculations from 0.375 µm to 16000 µm

Volume	100.0%		
Mean:	739.8 µm	95% Conf. Limits:	0-4411 µm
Median:	242.7 µm	S.D.:	1873 µm
D(3,2):	25.55 µm	Variance:	3507858 µm^2
Mean/Median Ratio:	3.048	C.V.:	253%
Mode:	223.4 µm	Skewness:	4.984 Right skewed
d_{10}:	20.14 µm	Kurtosis:	24.88 Leptokurtic
d_{50}:	242.7 µm		
d_{90}:	1338 µm		
Specific Surf. Area	2348 cm^2/ml		

% <	10	20	50	75	90
Size µm	20.14	108.3	242.7	533.2	1338

c051a.$02

Particle Diameter µm	Volume % <	Particle Diameter µm	Volume % <
2.000	2.09	8000	97.3
5.000	5.05		
10.00	7.51		
15.00	8.88		
20.00	9.97		
50.00	13.8		
60.00	14.8		
63.00	15.1		
70.00	15.8		
75.00	16.3		
90.00	17.8		
125.0	22.8		
200.0	40.6		
250.0	51.4		
400.0	68.4		
500.0	73.7		
1000	85.3		
2000	95.2		
4000	96.8		

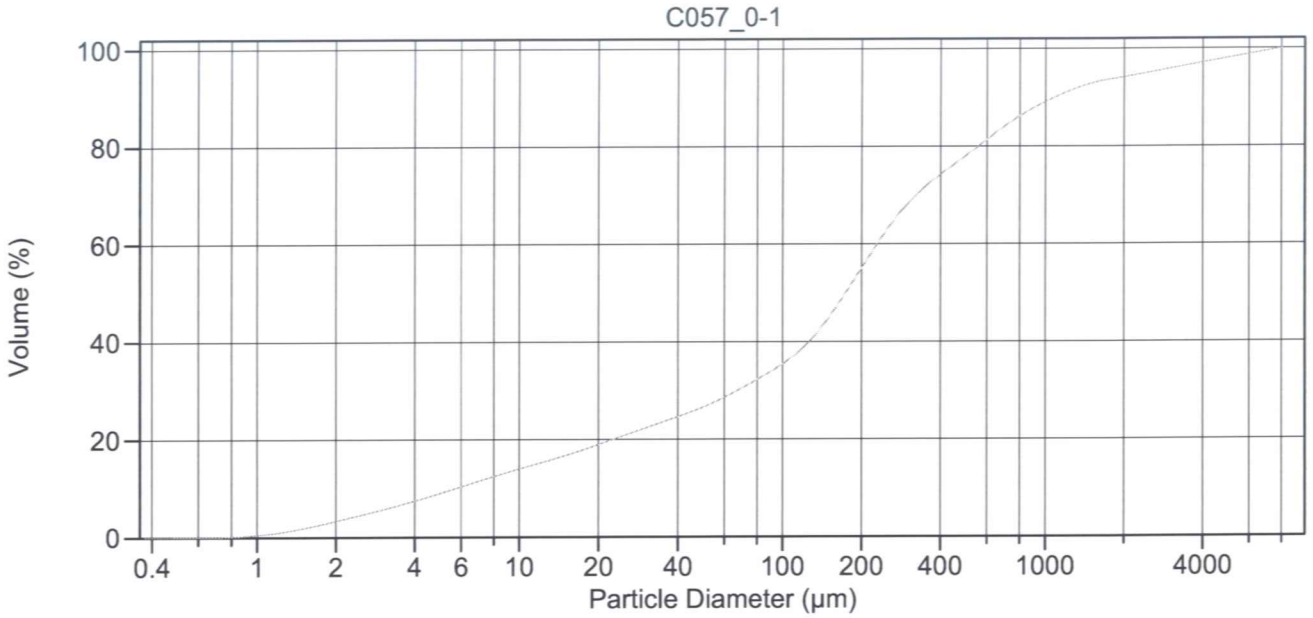

Volume Statistics (Arithmetic) c057a.$02

Calculations from 0.375 µm to 8000 µm

Volume	100.0%		
Mean:	501.9 µm	95% Conf. Limits:	0-2546 µm
Median:	174.1 µm	S.D.:	1043 µm
D(3,2):	16.62 µm	Variance:	1087805 µm^2
Mean/Median Ratio:	2.883	C.V.:	208%
Mode:	203.5 µm	Skewness:	3.811 Right skewed
d_{10}:	5.733 µm	Kurtosis:	15.03 Leptokurtic
d_{50}:	174.1 µm		
d_{90}:	1086 µm		
Specific Surf. Area	3610 cm^2/ml		

% <	10	20	50	75	90
Size µm	5.733	22.63	174.1	417.8	1086

c057a.$02

Particle Diameter µm	Volume % <	Particle Diameter µm	Volume % <
2.000	3.32	8000	100
5.000	9.00		
10.00	14.0		
15.00	16.7		
20.00	19.0		
50.00	26.6		
60.00	28.6		
63.00	29.1		
70.00	30.5		
75.00	31.4		
90.00	33.8		
125.0	39.8		
200.0	55.1		
250.0	62.9		
400.0	74.2		
500.0	78.1		
1000	89.1		
2000	94.1		
4000	97.1		

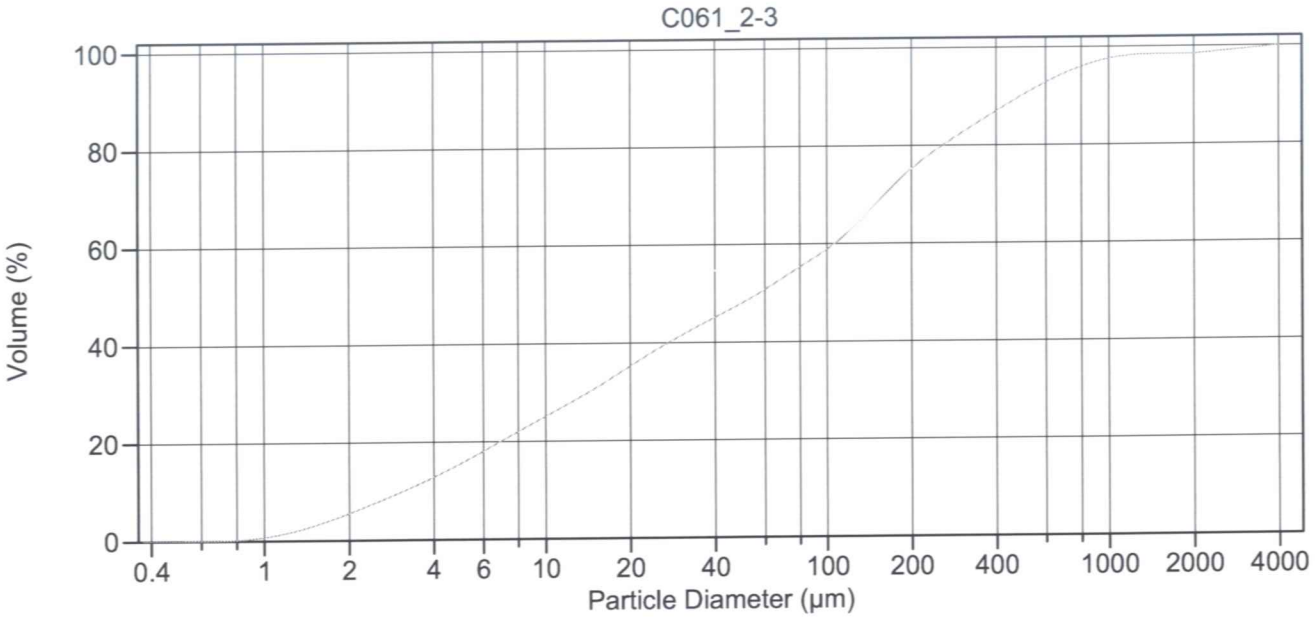

Volume Statistics (Arithmetic) c061a.$02

Calculations from 0.375 µm to 4000 µm

Volume	100.0%		
Mean:	190.2 µm	95% Conf. Limits:	0-963.7 µm
Median:	57.30 µm	S.D.:	394.6 µm
D(3,2):	9.819 µm	Variance:	155745 µm^2
Mean/Median Ratio:	3.319	C.V.:	208%
Mode:	153.8 µm	Skewness:	4.919 Right skewed
d_{10}:	3.125 µm	Kurtosis:	28.74 Leptokurtic
d_{50}:	57.30 µm		
d_{90}:	490.3 µm		
Specific Surf. Area	6110 cm^2/ml		

% <	10	20	50	75	90
Size µm	3.125	6.910	57.30	197.9	490.3

c061a.$02

Particle Diameter µm	Volume % <	Particle Diameter µm	Volume % <
2.000	5.52	8000	100
5.000	15.6		
10.00	25.1		
15.00	30.7		
20.00	35.3		
50.00	48.0		
60.00	50.7		
63.00	51.5		
70.00	53.2		
75.00	54.3		
90.00	57.1		
125.0	63.4		
200.0	75.2		
250.0	79.4		
400.0	87.0		
500.0	90.3		
1000	97.6		
2000	98.4		
4000	100		

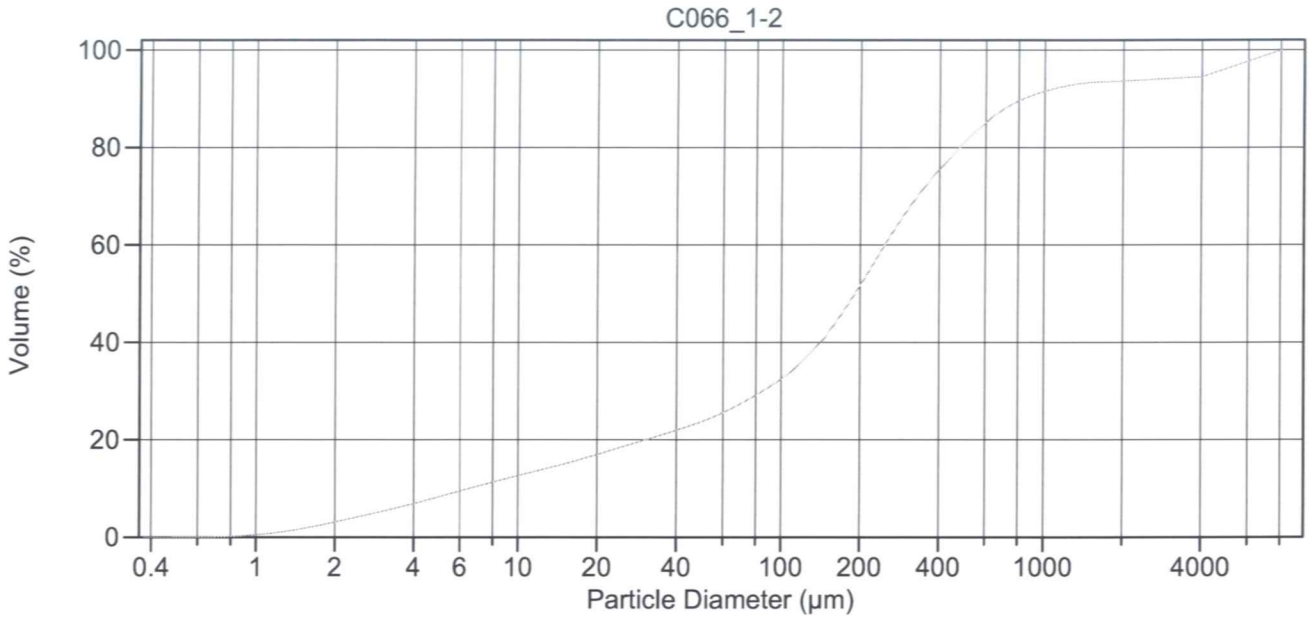

Volume Statistics (Arithmetic) c066a.$02

Calculations from 0.375 µm to 8000 µm

Volume	100.0%		
Mean:	561.8 µm	95% Conf. Limits:	0-3061 µm
Median:	191.4 µm	S.D.:	1275 µm
D(3,2):	17.92 µm	Variance:	1626034 µm^2
Mean/Median Ratio:	2.935	C.V.:	227%
Mode:	5657 µm	Skewness:	3.516 Right skewed
d_{10}:	6.517 µm	Kurtosis:	11.07 Leptokurtic
d_{50}:	191.4 µm		
d_{90}:	833.4 µm		
Specific Surf. Area	3349 cm^2/ml		

% <	10	20	50	75	90
Size µm	6.517	30.60	191.4	392.8	833.4

c066a.$02

Particle Diameter µm	Volume % <	Particle Diameter µm	Volume % <
2.000	3.10	8000	100
5.000	8.28		
10.00	12.7		
15.00	15.0		
20.00	17.0		
50.00	23.8		
60.00	25.6		
63.00	26.1		
70.00	27.4		
75.00	28.3		
90.00	30.8		
125.0	36.8		
200.0	51.7		
250.0	60.4		
400.0	75.5		
500.0	81.1		
1000	91.5		
2000	93.7		
4000	94.5		

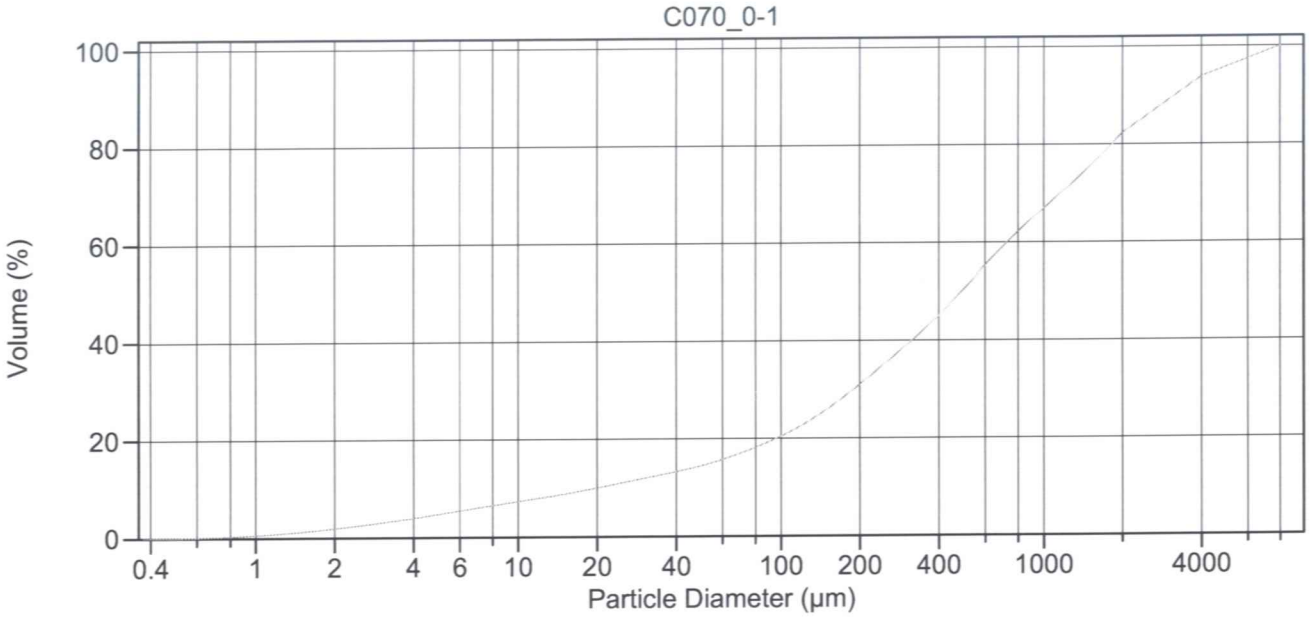

Volume Statistics (Arithmetic) c070#a.$02

Calculations from 0.375 µm to 8000 µm

Volume	100.0%		
Mean:	1104 µm	95% Conf. Limits:	0-3963 µm
Median:	490.6 µm	S.D.:	1459 µm
D(3,2):	27.61 µm	Variance:	2127909 µm^2
Mean/Median Ratio:	2.249	C.V.:	132%
Mode:	2828 µm	Skewness:	1.923 Right skewed
d_{10}:	19.89 µm	Kurtosis:	3.164 Leptokurtic
d_{50}:	490.6 µm		
d_{90}:	3333 µm		
Specific Surf. Area	2173 cm^2/ml		

% <	10	20	50	75	90
Size µm	19.89	96.15	490.6	1474	3333

c070#a.$02

Particle Diameter µm	Volume % <	Particle Diameter µm	Volume % <
2.000	1.92	8000	100
5.000	4.77		
10.00	7.31		
15.00	8.78		
20.00	10.0		
50.00	14.5		
60.00	15.7		
63.00	16.1		
70.00	17.0		
75.00	17.6		
90.00	19.3		
125.0	23.2		
200.0	31.0		
250.0	35.3		
400.0	45.0		
500.0	50.5		
1000	66.9		
2000	82.3		
4000	93.8		

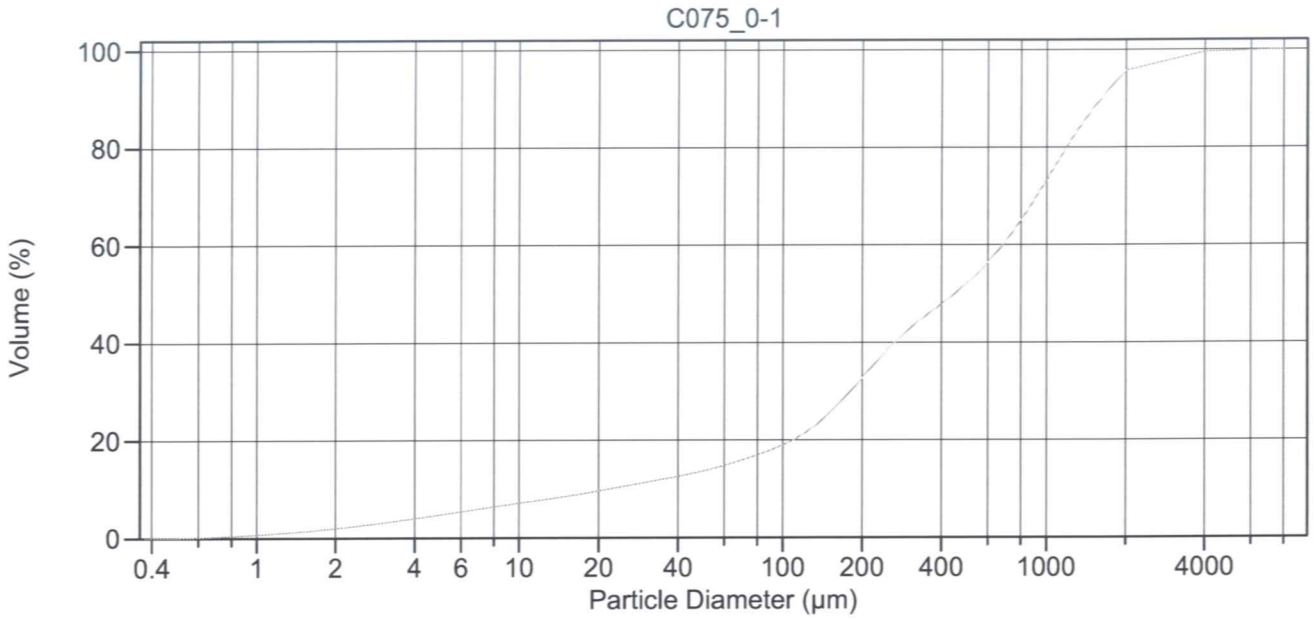

Volume Statistics (Arithmetic) c075a.$02

Calculations from 0.375 µm to 8000 µm

Volume	100.0%		
Mean:	692.4 µm	95% Conf. Limits:	0-2163 µm
Median:	449.4 µm	S.D.:	750.1 µm
D(3,2):	26.95 µm	Variance:	562713 µm^2
Mean/Median Ratio:	1.541	C.V.:	108%
Mode:	2828 µm	Skewness:	2.143 Right skewed
d_{10}:	21.98 µm	Kurtosis:	7.917 Leptokurtic
d_{50}:	449.4 µm		
d_{90}:	1613 µm		
Specific Surf. Area	2226 cm^2/ml		

% <	10	20	50	75	90
Size µm	21.98	109.5	449.4	1045	1613

c075a.$02

Particle Diameter µm	Volume % <	Particle Diameter µm	Volume % <
2.000	2.00	8000	100
5.000	4.75		
10.00	7.11		
15.00	8.47		
20.00	9.61		
50.00	13.7		
60.00	14.8		
63.00	15.1		
70.00	15.9		
75.00	16.4		
90.00	17.9		
125.0	21.9		
200.0	32.7		
250.0	38.5		
400.0	47.8		
500.0	52.2		
1000	73.3		
2000	95.8		
4000	99.6		

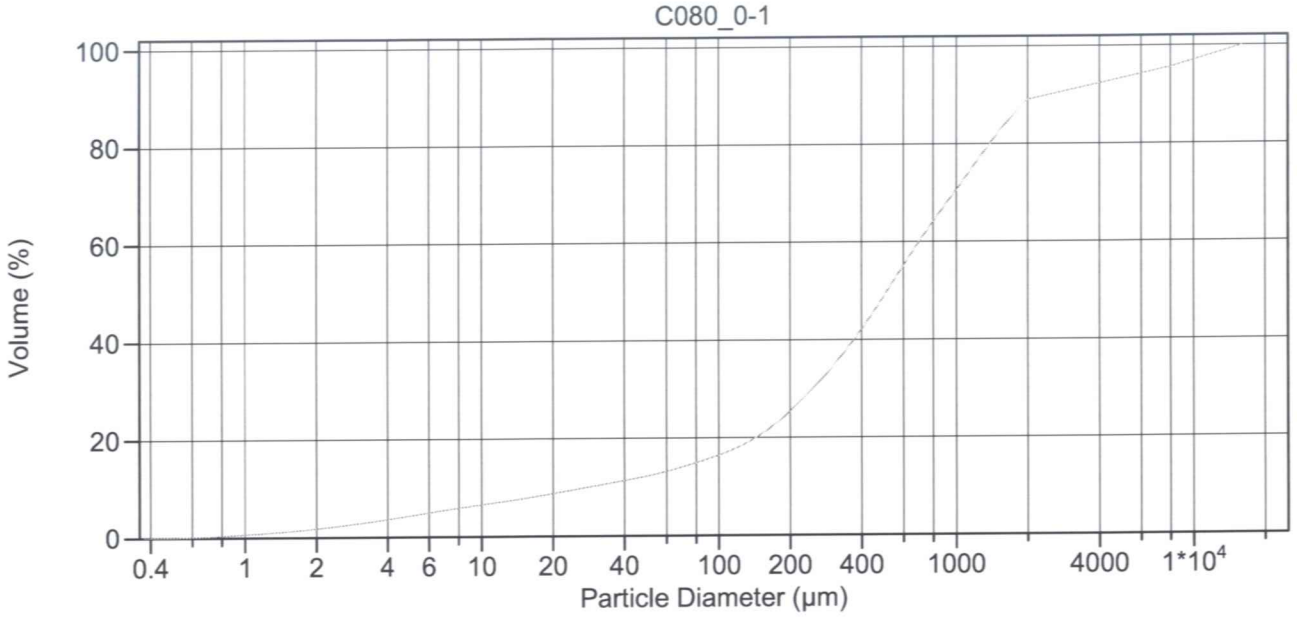

Volume Statistics (Arithmetic) c080a.$02

Calculations from 0.375 µm to 16000 µm

Volume	100.0%		
Mean:	1288 µm	95% Conf. Limits:	0-6010 µm
Median:	513.9 µm	S.D.:	2409 µm
D(3,2):	29.79 µm	Variance:	5802474 µm^2
Mean/Median Ratio:	2.507	C.V.:	187%
Mode:	11314 µm	Skewness:	3.323 Right skewed
d_{10}:	28.03 µm	Kurtosis:	10.58 Leptokurtic
d_{50}:	513.9 µm		
d_{90}:	2574 µm		
Specific Surf. Area	2014 cm^2/ml		

% <	10	20	50	75	90
Size µm	28.03	143.3	513.9	1166	2574

c080a.$02

Particle Diameter µm	Volume % <	Particle Diameter µm	Volume % <
2.000	1.80	8000	95.6
5.000	4.34		
10.00	6.53		
15.00	7.74		
20.00	8.75		
50.00	12.3		
60.00	13.2		
63.00	13.4		
70.00	14.1		
75.00	14.5		
90.00	15.7		
125.0	18.4		
200.0	25.4		
250.0	30.0		
400.0	42.1		
500.0	49.1		
1000	70.5		
2000	89.1		
4000	92.4		

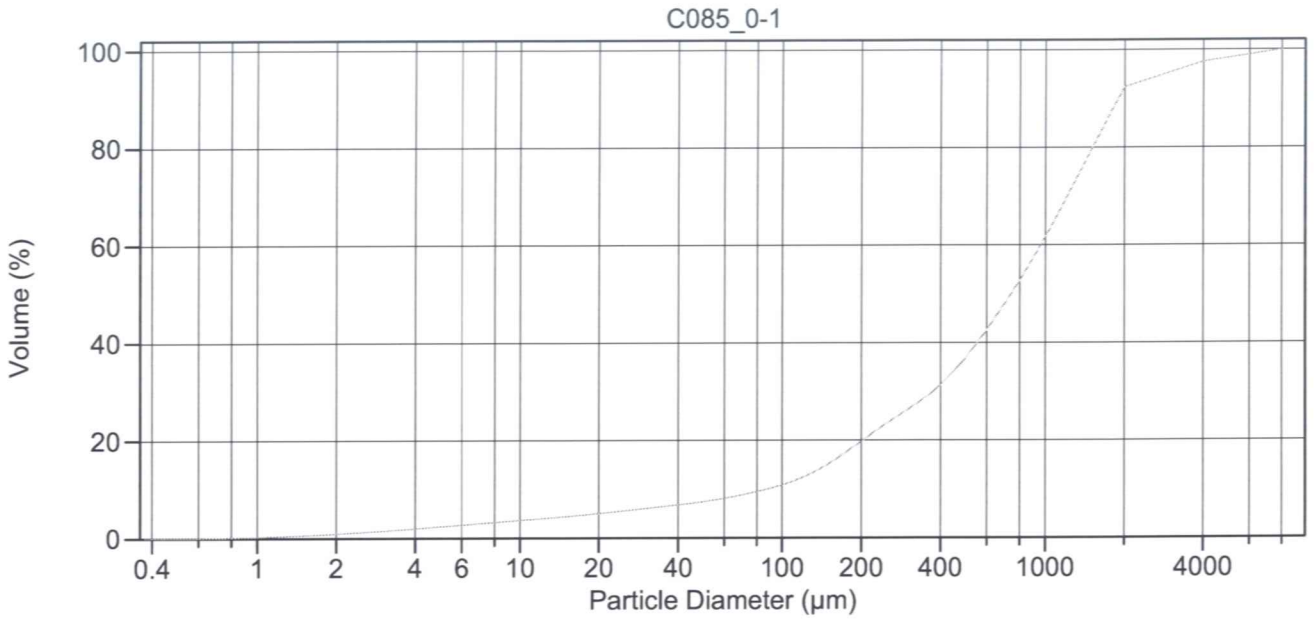

Volume Statistics (Arithmetic) c085a.$02

Calculations from 0.375 µm to 8000 µm

Volume	100.0%		
Mean:	985.6 µm	95% Conf. Limits:	0-2990 µm
Median:	741.7 µm	S.D.:	1023 µm
D(3,2):	52.99 µm	Variance:	1045630 µm^2
Mean/Median Ratio:	1.329	C.V.:	104%
Mode:	2828 µm	Skewness:	2.475 Right skewed
d_{10}:	87.96 µm	Kurtosis:	8.246 Leptokurtic
d_{50}:	741.7 µm		
d_{90}:	1898 µm		
Specific Surf. Area	1132 cm^2/ml		

% <	10	20	50	75	90
Size µm	87.96	202.6	741.7	1358	1898

c085a.$02

Particle Diameter µm	Volume % <	Particle Diameter µm	Volume % <
2.000	0.92	8000	100
5.000	2.37		
10.00	3.65		
15.00	4.41		
20.00	5.05		
50.00	7.42		
60.00	8.10		
63.00	8.31		
70.00	8.79		
75.00	9.13		
90.00	10.1		
125.0	12.8		
200.0	19.8		
250.0	23.4		
400.0	31.3		
500.0	36.9		
1000	61.6		
2000	92.4		
4000	97.6		

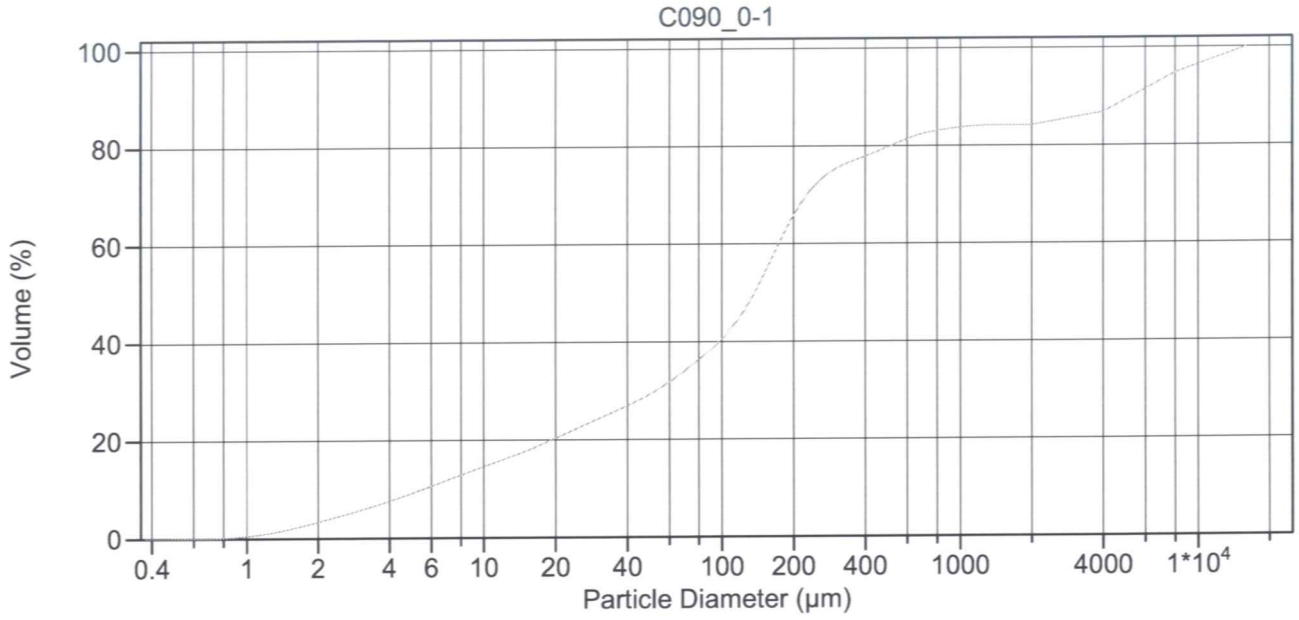

Volume Statistics (Arithmetic) c090a.$02

Calculations from 0.375 µm to 16000 µm

Volume	100.0%		
Mean:	1240 µm	95% Conf. Limits:	0-6777 µm
Median:	137.1 µm	S.D.:	2825 µm
D(3,2):	15.94 µm	Variance:	7982226 µm^2
Mean/Median Ratio:	9.044	C.V.:	228%
Mode:	5657 µm	Skewness:	2.637 Right skewed
d_{10}:	5.557 µm	Kurtosis:	5.986 Leptokurtic
d_{50}:	137.1 µm		
d_{90}:	5613 µm		
Specific Surf. Area	3765 cm^2/ml		

% <	10	20	50	75	90
Size µm	5.557	19.33	137.1	292.9	5613

c090a.$02

Particle Diameter µm	Volume % <	Particle Diameter µm	Volume % <
2.000	3.34	8000	94.8
5.000	9.19		
10.00	14.6		
15.00	17.7		
20.00	20.3		
50.00	29.3		
60.00	31.8		
63.00	32.5		
70.00	34.1		
75.00	35.2		
90.00	38.4		
125.0	46.6		
200.0	65.8		
250.0	72.3		
400.0	77.9		
500.0	79.8		
1000	83.7		
2000	84.2		
4000	86.8		

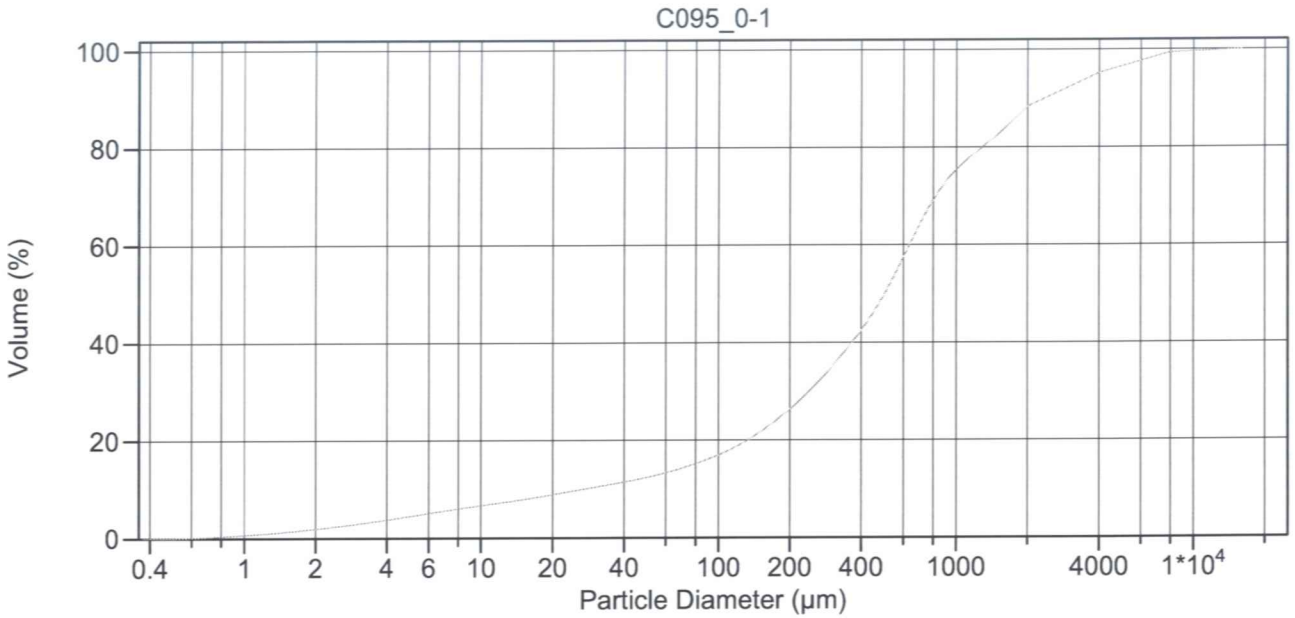

Volume Statistics (Arithmetic) c095a.$02

Calculations from 0.375 µm to 16000 µm

Volume	100.0%		
Mean:	965.4 µm	95% Conf. Limits:	0-3855 µm
Median:	501.8 µm	S.D.:	1474 µm
D(3,2):	28.71 µm	Variance:	2173181 µm^2
Mean/Median Ratio:	1.924	C.V.:	153%
Mode:	2828 µm	Skewness:	3.514 Right skewed
d_{10}:	27.14 µm	Kurtosis:	16.29 Leptokurtic
d_{50}:	501.8 µm		
d_{90}:	2487 µm		
Specific Surf. Area	2090 cm^2/ml		

% <	10	20	50	75	90
Size µm	27.14	132.7	501.8	984.5	2487

c095a.$02

Particle Diameter µm	Volume % <	Particle Diameter µm	Volume % <
2.000	1.90	8000	99.4
5.000	4.49		
10.00	6.67		
15.00	7.87		
20.00	8.88		
50.00	12.4		
60.00	13.3		
63.00	13.6		
70.00	14.2		
75.00	14.7		
90.00	16.1		
125.0	19.3		
200.0	26.3		
250.0	30.8		
400.0	42.4		
500.0	49.9		
1000	75.3		
2000	88.3		
4000	95.3		

Appendix 4. Results of radiometric dating of sediment cores.

Gamma Dating Center Copenhagen

Copenhagen, 9 October 2006

Thorbjørn J. Andersen
Institute of Geography
University of Copenhagen
Oester Voldgade 10
1350 Copenhagen K
e-mail tja@geogr.ku.dk
phone +45 35 32 25 03
fax +45 35 32 25 01

Dating of core 006

Dating of core 006

Methods

The samples have been analysed for the activity of ^{210}Pb, ^{226}Ra and ^{137}Cs via gammaspectrometry at the Gamma Dating Center, Institute of Geography, University of Copenhagen. The measurements were carried out on a Canberra low-background Ge-detector. ^{210}Pb was measured via its gamma-peak at 46,5 keV, ^{226}Ra via the granddaughter ^{214}Pb (peaks at 295 and 352 keV) and ^{137}Cs via its peak at 661 keV.

Results

The core showed high surface contents of unsupported ^{210}Pb and and a tendency for an exponential decrease with depth. The content of ^{137}Cs was high in the topmost sample but otherwise low and decreasing downcore (table 1 and fig 1).

CRS-modelling (Appleby, 2001) has been applied on the profile, assuming that the level of absence of unsupported ^{210}Pb is reached at 10.5 cm depth. The result is given in table 2.
The ^{137}Cs-profile does not give any good indirect indication of the quality of this dating. The general similarity between the ^{210}Pb and ^{137}Cs profiles indicates that the distribution of the isotopes could partly or entirely be explained by mixing of surface sediments on a station with little or no sediment accumulation. However, the inventory of unsupported ^{210}Pb is 308 Bq m^{-2} y^{-1} which is about four times higher than the estimated atmospheric flux at the site. This indicates that sediment focussing is taking place and bioturbation alone is not responsible for the isotope-profiles. In conclusion, the ages given in table 2 should be regarded as minimum ages due to possibility of bioturbation/mixing at the site.

9 October 2006

Thorbjørn J Andersen

Reference:
Appleby, P.G. (2001): Chronostratigraphic techniques in recent sediments. In: Last, W.M & Smol, J.P. (eds) Tracking environmental change using lake sediments. Volume 1: Basin analysis, coring and chronological techniques. Kluwer Academic Publishers, the Netherlands.

Table 1. Core 006

Depth	Pb-210tot	error Pb-210 tot	Pb-210 supupp 210Pb	error pb-210 sup	Pb-210 unsup	error pb-210 unsup	Cs-137	error Cs-137
cm	Bq kg-1	Bq kg-1	Bq kg-1	Bq kg-1	Bq kg-1	Bq kg-1	Bq kg-1	Bq kg-1
0.5	239	16	22	1	217	16	148	5
1.5	121	9	23	2	99	9	35	2
2.5	66	5	22	0	44	5	13	1
3.5	79	7	29	2	49	7	10	1
4.5	74	7	28	1	46	7	12	1
6.5	65	6	25	0	40	6	9	1
8.5	38	3	23	1	15	3	3	0
10.5	23	3	28	2	0	4	1	0
14.5	29	3	24	1	5	3	1	0
20.5	23	3	27	2	0	4	1	3

Table 2, Core 006, CRS-dating

Depth	acc dry mass	Age	error age	Date	acc rate	error rate
cm	g cm-3	y	y	y	(kg m-2 y-1)	(kg m-2 y-1)
0				2005		
0.5	0.79	6	2	1999	1.3	0.1
1.5	2.41	18	2	1987	1.3	0.1
2.5	4.08	26	2	1979	2.2	0.3
3.5	5.76	32	3	1973	2.6	0.4
4.5	7.49	41	3	1964	2.1	0.3
6.5	11.03	66	7	1939	1.4	0.3
8.5	14.67	116	20	1889	0.7	0.5

Fig 1

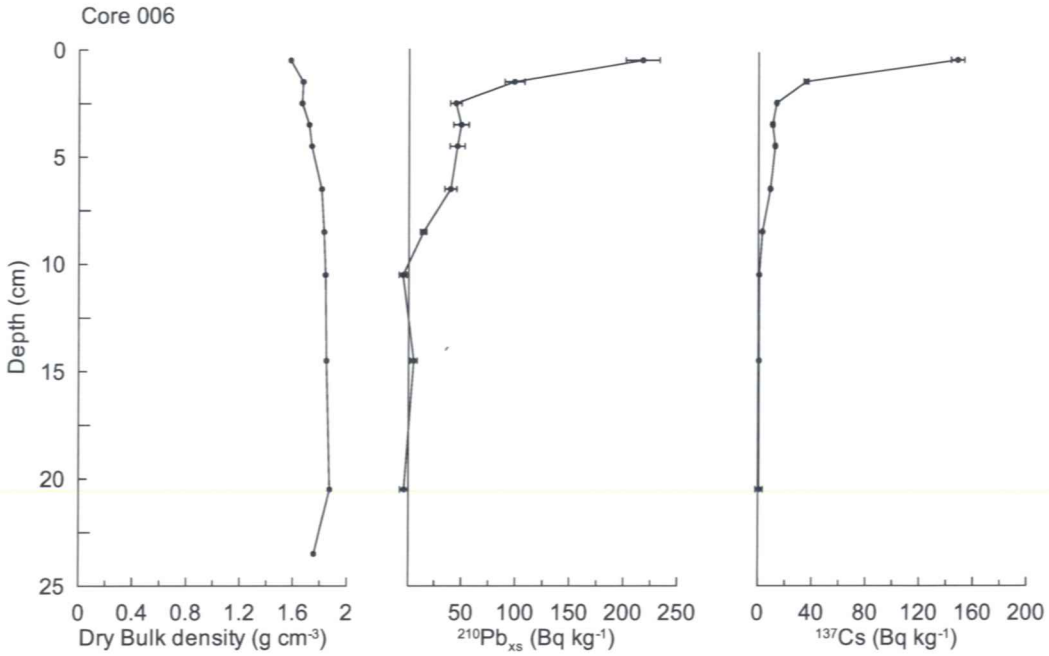
Core 006
Depth (cm)
0
5
10
15
20
25
0 0.4 0.8 1.2 1.6 2
Dry Bulk density (g cm-3)
50 100 150 200 250
210Pbxs (Bq kg-1)
0 40 80 120 160 200
137Cs (Bq kg-1)

Fig 2

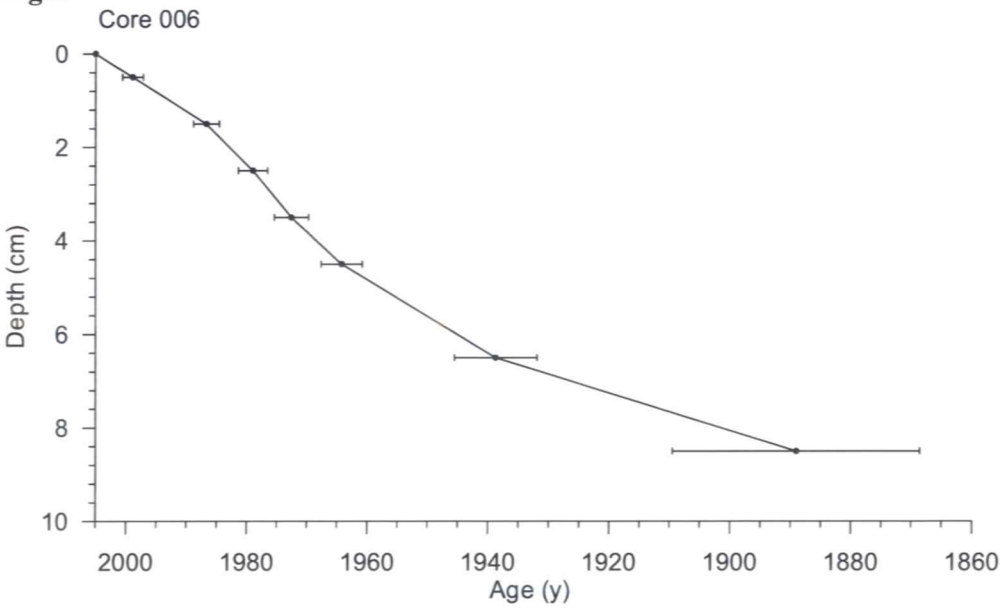
Core 006
Depth (cm)
0
2
4
6
8
10
2000 1980 1960 1940 1920 1900 1880 1860
Age (y)

Dating of core 013

Methods

The samples have been analysed for the activity of ^{210}Pb, ^{226}Ra and ^{137}Cs via gammaspectrometry at the Gamma Dating Center, Institute of Geography, University of Copenhagen. The measurements were carried out on a Canberra low-background Ge-detector. ^{210}Pb was measured via its gamma-peak at 46,5 keV, ^{226}Ra via the granddaughter ^{214}Pb (peaks at 295 and 352 keV) and ^{137}Cs via its peak at 661 keV.

Results

Only five 2 cm-samples were analysed in this core and both the low number of samples and the poor vertical resolution makes this dating-attempt less precise than what our laboratory normally aim at.

The core showed high surface contents of unsupported ^{210}Pb and and a tendency for an exponential decrease with depth. Cs-137 was found only in the two topmost samples (table 1 and fig 1). The inventory of unsupported ^{210}Pb is about 500 Bq m^{-2} y^{-1} which is about six times higher than the estimated atmospheric flux at the site.

CIC-modelling (Appleby, 2001) has been applied on the profile on the basis of the regression line shown in fig 2. The dating is given in table 2. The calculated accumulation rate is 0.31 ± 0.01 kg m^{-2} y^{-1}.

The ^{137}Cs-profile does not give any good indirect indication of the quality of this dating. The general similarity between the ^{210}Pb and ^{137}Cs profiles indicates that the distribution of the isotopes could partly or entirely be explained by mixing of surface sediments on a station with little or no sediment accumulation. However, the high inventory of unsupported ^{210}Pb shows that sediment focussing is taking place and bioturbation alone is not responsible for the isotope-profiles. In conclusion, the ages given in table 2 should be regarded as minimum ages due to possibility of bioturbation/mixing at the site.

9 October 2006

Thorbjørn J Andersen

Reference:
Appleby, P.G. (2001): Chronostratigraphic techniques in recent sediments. In: Last, W.M & Smol, J.P. (eds) Tracking environmental change using lake sediments. Volume 1: Basin analysis, coring and chronological techniques. Kluwer Academic Publishers, the Netherlands.

Table 1. Core 013

Depth	Pb-210tot	error Pb-210 tot	Pb-210 supupp 210Pb	error pb-210 sup	Pb-210 unsup	error pb-210 unsup	Cs-137	error Cs-137
cm	Bq kg-1	Bq kg-1	Bq kg-1	Bq kg-1	Bq kg-1	Bq kg-1	Bq kg-1	Bq kg-1
1	429	11	32	3	397	12	35	2
3	81	11	30	0	51	11	14	3
5	34	11	26	1	7	11	0	0
7	20	11	29	5	0	12	0	0
9	35	10	36	12	0	16	0	0

Table 2, Core 013, CIC-modelling

Depth	acc dry mass	Age	error age	Date
cm	g cm-3	y	y	y
0				2005
1	1.28	41	1	1964
3	3.91	125	3	1880

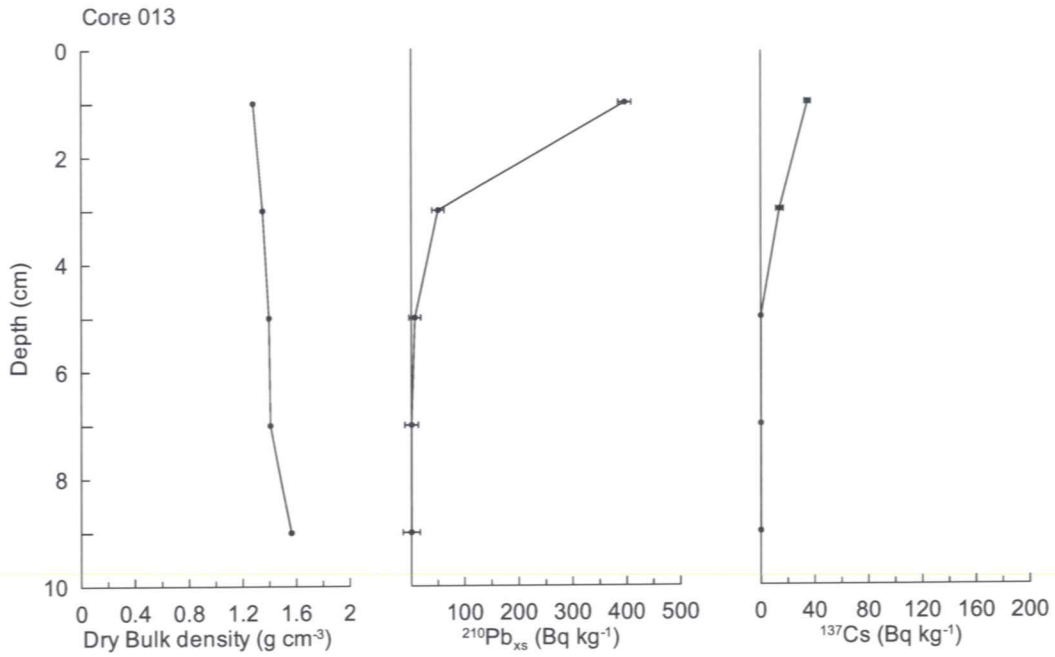
Core 013
Depth (cm)
0
2
4
6
8
10
0 0.4 0.8 1.2 1.6 2
Dry Bulk density (g cm-3)
100 200 300 400 500
210Pbxs (Bq kg-1)
0 40 80 120 160 200
137Cs (Bq kg-1)

Fig 1

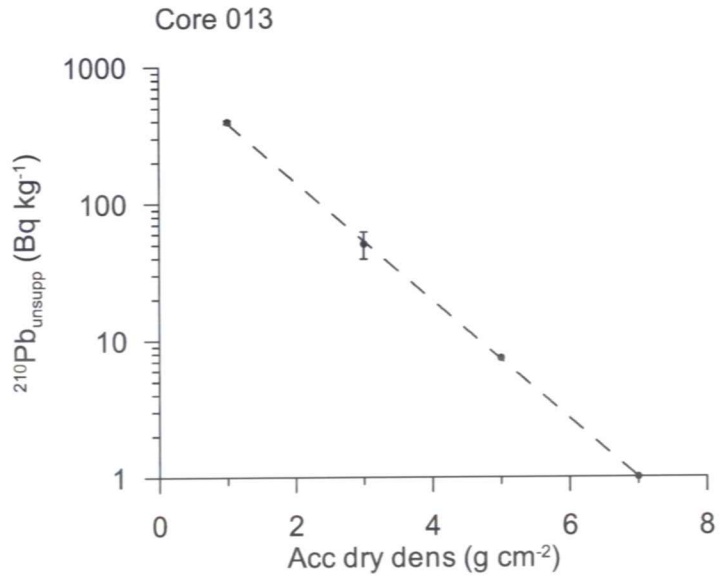
Core 013
1000
100
10
1
210Pbunsupp (Bq kg-1)
0
2
4
6
8
Acc dry dens (g cm-2)

Fig 2

Dating of core 021

Methods

The samples have been analysed for the activity of ^{210}Pb, ^{226}Ra and ^{137}Cs via gammaspectrometry at the Gamma Dating Center, Institute of Geography, University of Copenhagen. The measurements were carried out on a Canberra low-background Ge-detector. ^{210}Pb was measured via its gamma-peak at 46,5 keV, ^{226}Ra via the granddaughter ^{214}Pb (peaks at 295 and 352 keV) and ^{137}Cs via its peak at 661 keV.

Results

The core showed high surface contents of unsupported ^{210}Pb and and a tendency for an exponential decrease with depth, although with major irregularities. The inventory of unsupported ^{210}Pb is about 630 Bq m^{-2} y^{-1} which is almost a magnitude higher than the estimated atmospheric flux at the site.

Weak peaks of ^{137}Cs were found at 1.5 and 5.5 cm depth. The upper one is likely to be due to the Chernobyl accident in 1986 whereas the lower one probably is related to grain size variation as a clear co-variation with ^{210}Pb is observed (fig1).

CRS-modelling (Appleby, 2001) has been applied on the profile assuming that there is no activity of unsupported ^{210}Pb below 11.5 cm. The result is given in table 2 and fig 2.

The upper peak in the ^{137}Cs-profile is dated to 1985 which is in good agreement with the expected Chernobyl-origin (1986). However, ^{137}Cs is also found at levels dated to before the release of this isotope into the environment (around 1954). This shows that some bioturbation/mixing of the surface sediments takes place. Therefore, the ages given in table 2 should be regarded as minimum ages.

10 October 2006

Thorbjørn J Andersen

Reference:
Appleby, P.G. (2001): Chronostratigraphic techniques in recent sediments. In: Last, W.M & Smol, J.P. (eds) Tracking environmental change using lake sediments. Volume 1: Basin analysis, coring and chronological techniques. Kluwer Academic Publishers, the Netherlands.

Table 1. Core 021

Depth	acc dry dens	Pb-210tot	error Pb-210 tot	Pb-210 supupp 210Pb	error pb-210 sup	Pb-210 unsup	error pb-210 unsup	Cs-137	error Cs-137
cm	g cm-2	Bq kg-1	Bq kg-1	Bq kg-1	Bq kg-1	Bq kg-1	Bq kg-1	Bq kg-1	Bq kg-1
0.5	0.66	487	17	29	12	458	21	47	3
1.5	2.10	439	16	28	3	411	17	64	3
2.5	3.64	170	12	29	3	141	13	20	2
3.5	5.20	97	8	32	4	65	9	7	1
4.5	6.78	100	10	28	3	72	11	14	2
5.5	8.34	127	11	35	5	92	12	20	2
6.5	9.91	100	11	30	1	70	12	14	2
7.5	11.52	44	12	18	1	26	12	4	2
9.5	14.96	38	11	28	4	10	11	1	2
11.5	18.52	19	10	27	3	0	11	0	0

Table 2, Core 021

Depth cm	acc dry mass g cm-3	Age y	error age y	Date y	acc rate (kg m-2 y-1)	error rate (kg m-2 y-1)
0				2005		
0.5	0.7	5	2	2000	1.3	0.1
1.5	2.1	20	2	1985	1.0	0.1
2.5	3.6	35	3	1970	1.0	0.1
3.5	5.2	44	4	1961	1.8	0.3
4.5	6.8	51	5	1954	2.1	0.4
5.5	8.3	63	7	1942	1.3	0.3
6.5	9.9	82	12	1923	0.8	0.3
7.5	11.5	104	23	1901	0.7	0.6
9.5	15.0	*153*	*101*	*1852*	*0.7*	*2.3*

Note: numbers in italics are not reliable

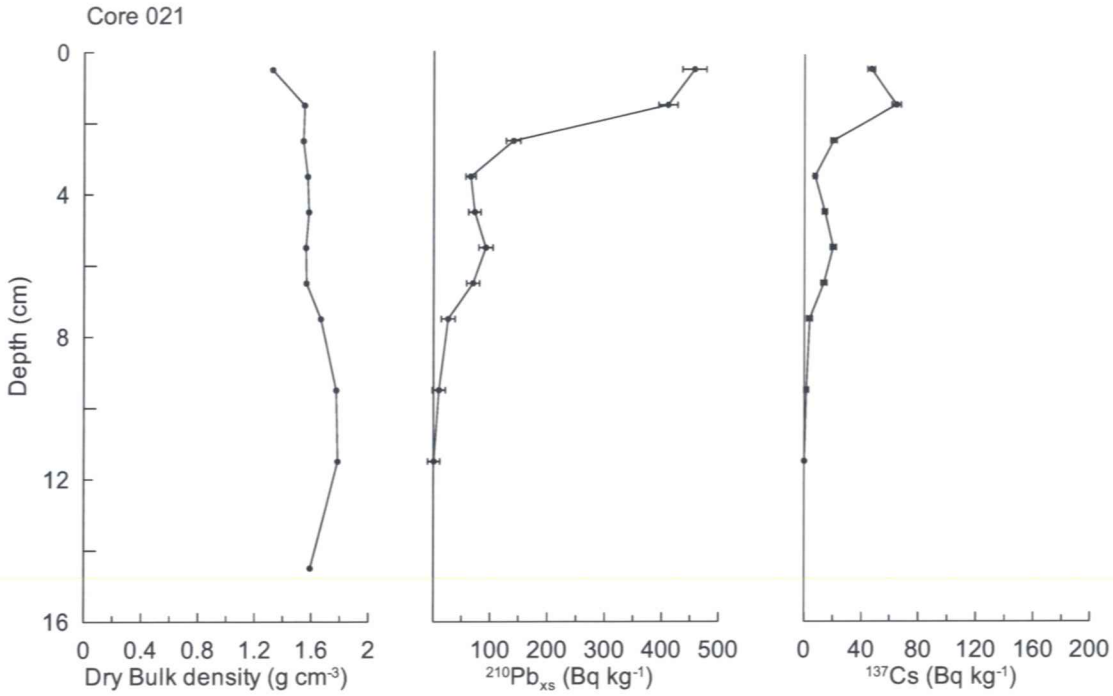
Core 021
Depth (cm)
0
4
8
12
16
0 0.4 0.8 1.2 1.6 2
Dry Bulk density (g cm-3)
100 200 300 400 500
210Pbxs (Bq kg-1)
0 40 80 120 160 200
137Cs (Bq kg-1)

Fig 1

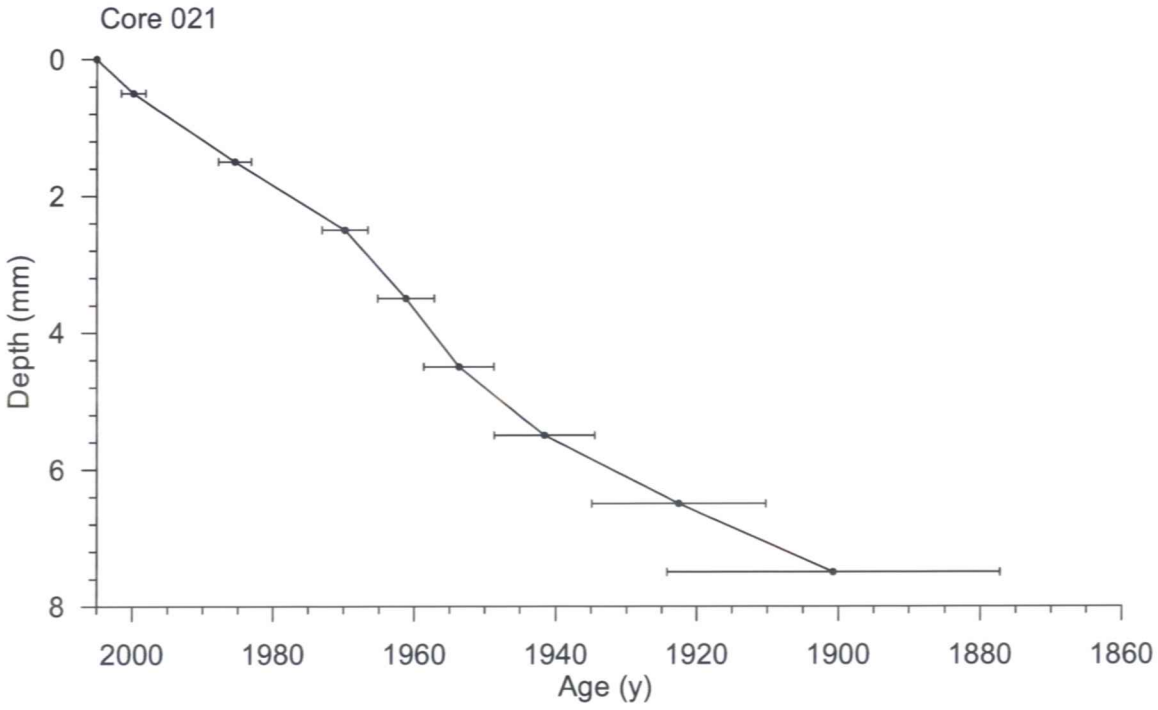
Core 021
Depth (mm)
0
2
4
6
8
2000
1980
1960
1940
1920
1900
1880
1860
Age (y)

Dating of core 026

Methods

The samples have been analysed for the activity of ^{210}Pb, ^{226}Ra and ^{137}Cs via gammaspectrometry at the Gamma Dating Center, Institute of Geography, University of Copenhagen. The measurements were carried out on a Canberra low-background Ge-detector. ^{210}Pb was measured via its gamma-peak at 46,5 keV, ^{226}Ra via the granddaughter ^{214}Pb (peaks at 295 and 352 keV) and ^{137}Cs via its peak at 661 keV.

Results

The core showed high surface contents of unsupported ^{210}Pb and and a tendency for an exponential decrease with depth. The flux of unsupported ^{210}Pb is about 530 Bq m^{-2} y^{-1} which is about eight times larger than the estimated atmospheric flux at the site.
The content of ^{137}Cs was generally low and decreasing downcore (table 1 and fig 1).

CRS-modelling (Appleby, 2001) has been applied on the profile using a modified method where the inventory below 7.5 cm is calculated on the basis of the regression shown in fig 2. The result is given in table 2.

The presence of ^{137}Cs in samples dated to before 1954 indicates that some mixing/bioturbation takes place at the site. However, the vertical profile of ^{210}Pb shows a tendency for the expected exponential decay with depth and the profile is not similar to the ^{137}Cs-profile. It is therefore concluded that the dating is reasonable robust but that the ages given in table 2 should be interpreted as minimum ages due to the possibility of bioturbation/mixing at the site.

12 October 2006

Thorbjørn J Andersen

Reference:
Appleby, P.G. (2001): Chronostratigraphic techniques in recent sediments. In: Last, W.M & Smol, J.P. (eds) Tracking environmental change using lake sediments. Volume 1: Basin analysis, coring and chronological techniques. Kluwer Academic Publishers, the Netherlands.

Table 1. Core 026

Depth	Pb-210tot	error Pb-210 tot	Pb-210 supupp 210Pb	error pb-210 sup	Pb-210 unsup	error pb-210 unsup	Cs-137	error Cs-137
cm	Bq kg-1	Bq kg-1	Bq kg-1	Bq kg-1	Bq kg-1	Bq kg-1	Bq kg-1	Bq kg-1
0.5	510	19	23	14	486	24	27	3
1.5	219	14	27	6	192	15	16	3
2.5	208	14	23	7	185	15	16	3
3.5	102	11	23	6	78	13	6	2
4.5	100	11	27	5	73	12	10	2
5.5	96	11	21	3	75	12	2	2
6.5	76	11	21	0	55	11	8	2
7.5	41	11	23	4	18	12	0	2
8.5	20	10	22	4	0	11	2	2
10.5	39	10	28	3	11	11	2	2

Table 2, Core 026, CRS-dating

Depth	acc dry dens	Age	error age	Date	acc rate	error rate
cm	g cm-3	y	y	y	(kg m-2 y-1)	(kg m-2 y-1)
0				2005		
0.5	0.7	5	2	2000	1.30	0.08
1.5	2.1	18	2	1987	1.10	0.10
2.5	3.7	30	2	1975	1.35	0.14
3.5	5.3	42	3	1963	1.34	0.23
4.5	6.9	51	4	1954	1.66	0.30
5.5	8.5	65	5	1940	1.18	0.23
6.5	10.2	86	7	1919	0.79	0.22
7.5	11.8	109	11	1896	0.72	0.26

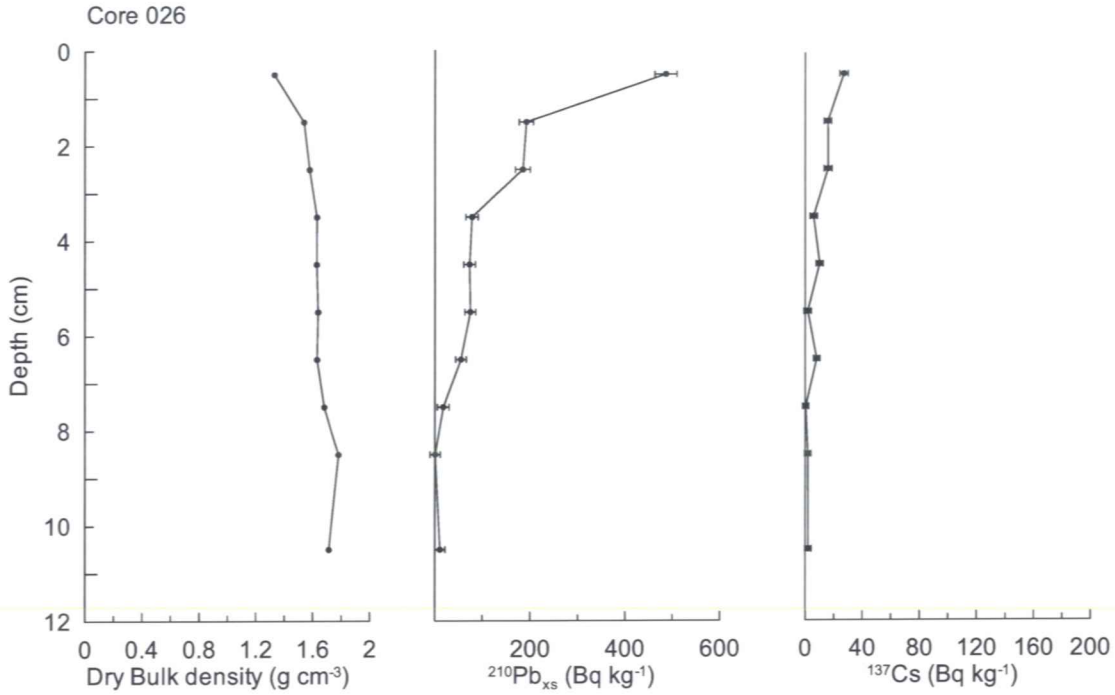
Core 026
Depth (cm)
0
2
4
6
8
10
12
0 0.4 0.8 1.2 1.6 2
Dry Bulk density (g cm-3)
200 400 600
210Pbxs (Bq kg-1)
0 40 80 120 160 200
137Cs (Bq kg-1)

Fig 1

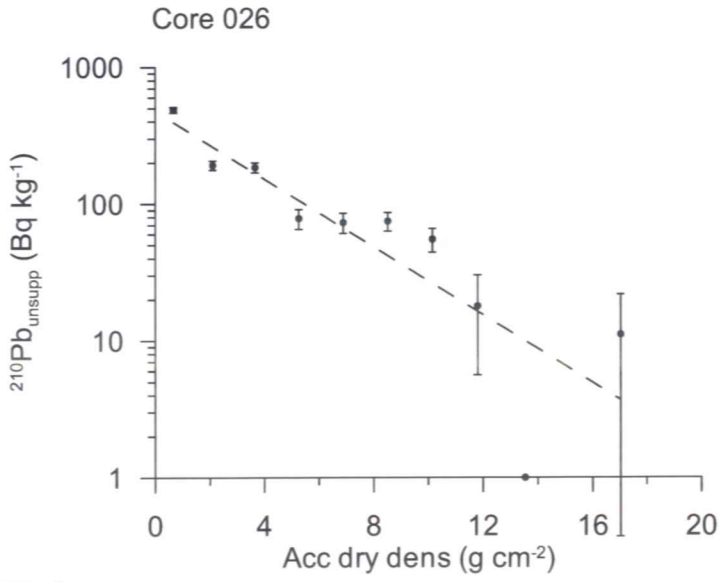
Core 026
1000
100
10
1
210Pbunsupp (Bq kg-1)
0 4 8 12 16 20
Acc dry dens (g cm-2)

Fig 2

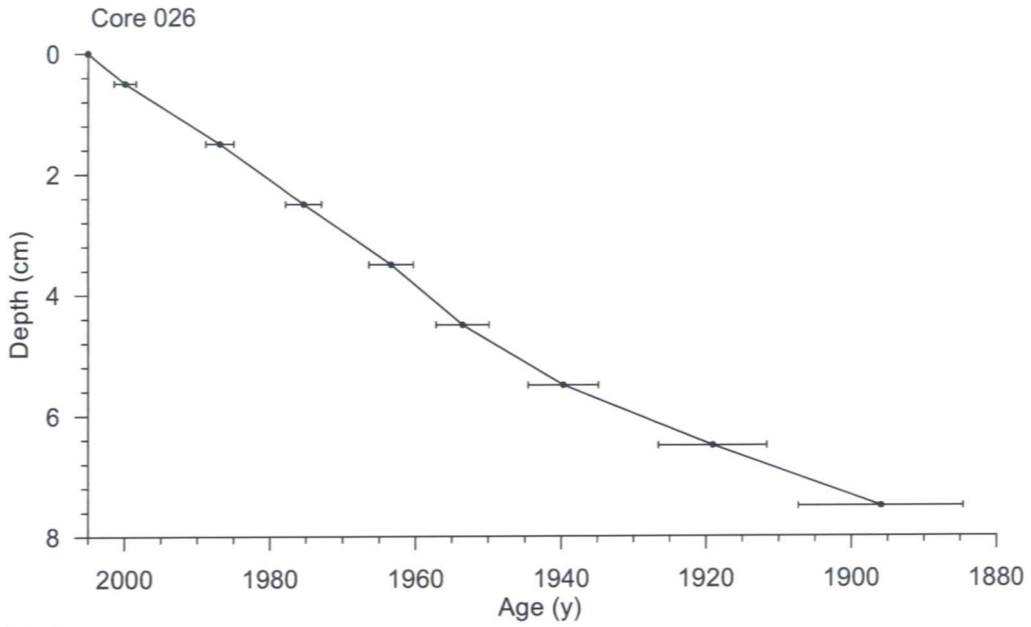
Core 026
0
2
4
6
8
Depth (cm)
2000
1980
1960
1940
1920
1900
1880
Age (y)

Fig 3

Dating of core 031

Methods

The samples have been analysed for the activity of ^{210}Pb, ^{226}Ra and ^{137}Cs via gammaspectrometry at the Gamma Dating Center, Institute of Geography, University of Copenhagen. The measurements were carried out on a Canberra low-background Ge-detector. ^{210}Pb was measured via its gamma-peak at 46,5 keV, ^{226}Ra via the granddaughter ^{214}Pb (peaks at 295 and 352 keV) and ^{137}Cs via its peak at 661 keV.

Results

The core showed moderate surface contents of unsupported ^{210}Pb and a very irregular profile downcore. Samples at depths of 5.5 cm and below had contents close to zero (note the large error-bars). Assuming that the activity is zero at 5.5 cm, the inventory of unsupported ^{210}Pb is about 230 Bq m^{-2} y^{-1} which is about three times higher than the estimated atmospheric flux at the site. Low contents of ^{137}Cs were found in the upper 4 cm of the core.

CRS-modelling (Appleby, 2001) has been applied on the profile assuming that there is no activity of unsupported ^{210}Pb below 5.5 cm. The result is given in table 2 and fig 2. The dating depends on where the level of zero activity is asumed to be, especially at the lower levels. Therefore, the dating at the lower levels has to be used with this in mind.

The irregular profile of unsupported ^{210}Pb, low levels of ^{137}Cs and possibility of sediment mixing makes dating of this core difficult and the result shown in table 2 and fig 2 is only indicative.

10 October 2006

Thorbjørn J Andersen

Reference:

Appleby, P.G. (2001): Chronostratigraphic techniques in recent sediments. In: Last, W.M & Smol, J.P. (eds) Tracking environmental change using lake sediments. Volume 1: Basin analysis, coring and chronological techniques. Kluwer Academic Publishers, the Netherlands.

Table 1. Core 031

Depth	Pb-210tot	error Pb-210 tot	Pb-210 supupp 210Pb	error pb-210 sup	Pb-210 unsup	error pb-210 unsup	Cs-137	error Cs-137
cm	Bq kg-1	Bq kg-1	Bq kg-1	Bq kg-1	Bq kg-1	Bq kg-1	Bq kg-1	Bq kg-1
0.5	187	13	32	6	155	14	17	2
1.5	88	9	27	0	61	9	11	2
2.5	115	7	24	2	91	7	6	1
3.5	128	14	16	0	112	14	8	3
4.5	53	11	21	3	32	11	1	2
5.5	33	10	19	5	14	12	0	0
6.5	42	11	27	8	15	14	2	3
7.5	42	12	29	7	14	14	0	2
8.5	7	12	25	1	0	12	3	2

Table 2, Core 031

Depth cm	acc dry mass g cm-3	Age y	error age y	Date y	acc rate (kg m-2 y-1)	error rate (kg m-2 y-1)
0.0				2005		
0.5	0.8	6	2	1999	1.4	0.1
1.5	2.5	17	3	1988	1.5	0.2
2.5	4.1	28	4	1977	1.5	0.2
3.5	5.7	51	7	1954	0.7	0.2
4.5	7.4	105	31	1900	0.3	0.3

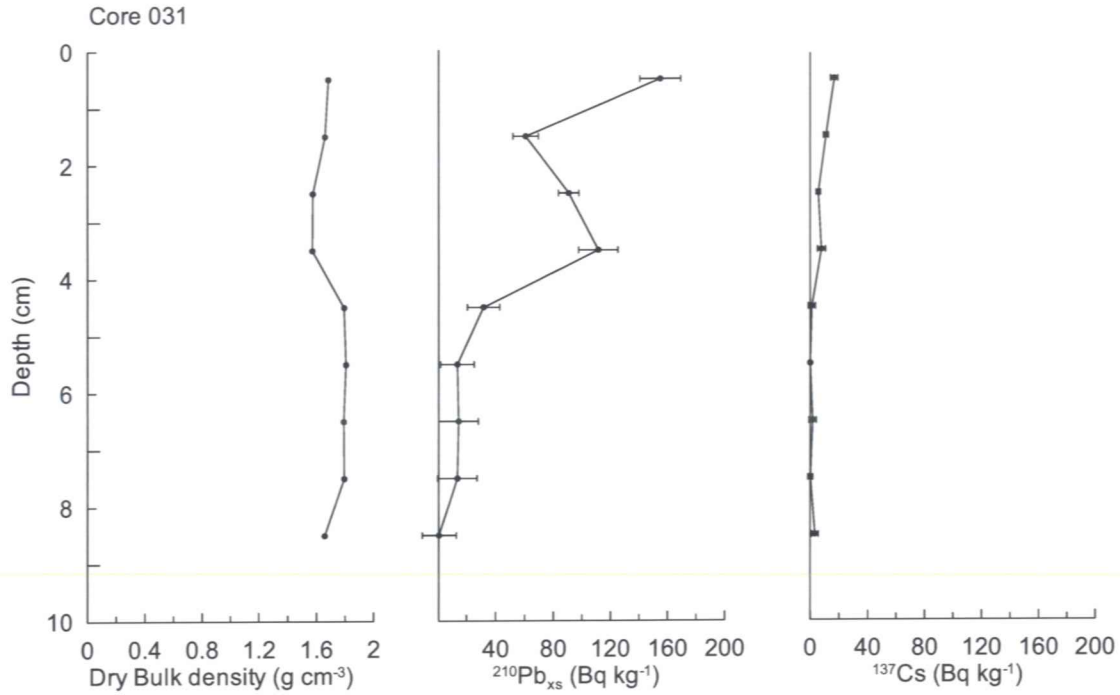
Core 031
Depth (cm)
0
2
4
6
8
10
0 0.4 0.8 1.2 1.6 2
Dry Bulk density (g cm-3)
40 80 120 160 200
210Pbxs (Bq kg-1)
0 40 80 120 160 200
137Cs (Bq kg-1)

Fig 1

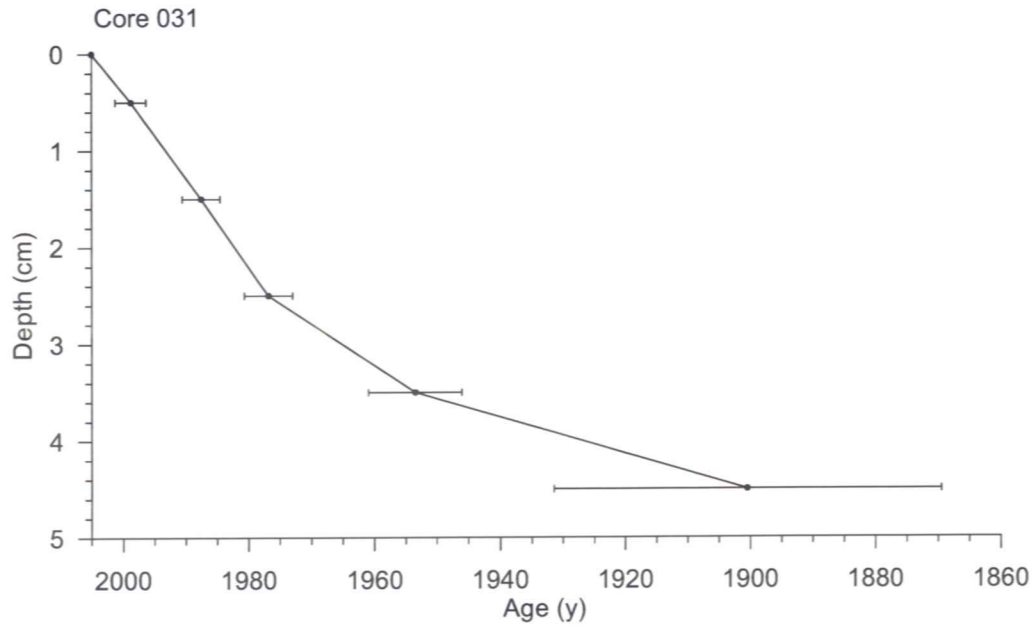
Core 031
Depth (cm)
0
1
2
3
4
5
2000
1980
1960
1940
1920
1900
1880
1860
Age (y)

Fig 2

Dating of core 057

Methods

The samples have been analysed for the activity of ^{210}Pb, ^{226}Ra and ^{137}Cs via gammaspectrometry at the Gamma Dating Center, Institute of Geography, University of Copenhagen. The measurements were carried out on a Canberra low-background Ge-detector. ^{210}Pb was measured via its gamma-peak at 46,5 keV, ^{226}Ra via the granddaughter ^{214}Pb (peaks at 295 and 352 keV) and ^{137}Cs via its peak at 661 keV.

Results

The core showed high surface contents of unsupported ^{210}Pb and an exponential decrease with depth down to about 6 cm. Cs-137 was generally only present in the top 5cm of the core (table 1 and fig 1).

CRS-modelling (Appleby, 2001) has been applied on the profile using a modified method where the inventory below 6.5 cm is calculated on the basis of the regression shown in fig 2. The result is given in table 2.

The presence of ^{137}Cs in samples dated to before 1954 indicates that some mixing/bioturbation takes place at the site. However, the vertical profile of ^{210}Pb shows the expected exponential decay with depth and the profile is not similar to the ^{137}Cs-profile. It is therefore concluded that the dating is reasonable robust but that the ages given in table should be interpreted as minimum ages due to the possibility of bioturbation/mixing at the site.

11 October 2006

Thorbjørn J Andersen

Reference:
Appleby, P.G. (2001): Chronostratigraphic techniques in recent sediments. In: Last, W.M & Smol, J.P. (eds) Tracking environmental change using lake sediments. Volume 1: Basin analysis, coring and chronological techniques. Kluwer Academic Publishers, the Netherlands.

Table 1. Core 057

Depth	Pb-210tot	error Pb-210 tot	Pb-210 supupp 210Pb	error pb-210 sup	Pb-210 unsup	error pb-210 unsup	Cs-137	error Cs-137
cm	Bq kg-1	Bq kg-1	Bq kg-1	Bq kg-1	Bq kg-1	Bq kg-1	Bq kg-1	Bq kg-1
0.5	198	14	28	13	169	19	13	3
1.5	142	12	22	0	120	12	28	2
2.5	98	11	27	2	71	11	23	2
3.5	73	12	24	1	49	12	11	2
4.5	56	11	39	2	17	11	0	2
6.5	37	10	28	5	8	11	0	0
8.5	34	10	28	7	7	13	5	2
10.5	43	12	32	8	12	14	6	2
14.5	43	12	32	5	10	13	0	0
22	49	12	38	6	11	13	2	2

Table 2, Core 057

Depth cm	acc dry mass g cm-3	Age y	error age y	Date y	acc rate (kg m-2 y-1)	error rate (kg m-2 y-1)
				2005		
0.5	0.8	6	3	1999	1.2	0.2
1.5	2.3	21	4	1984	1.0	0.2
2.5	3.9	39	7	1966	0.9	0.2
3.5	5.5	58	11	1947	0.8	0.4
4.5	7.2	78	20	1927	0.8	0.6
6.5	10.5	111	50	1894	1.0	1.6

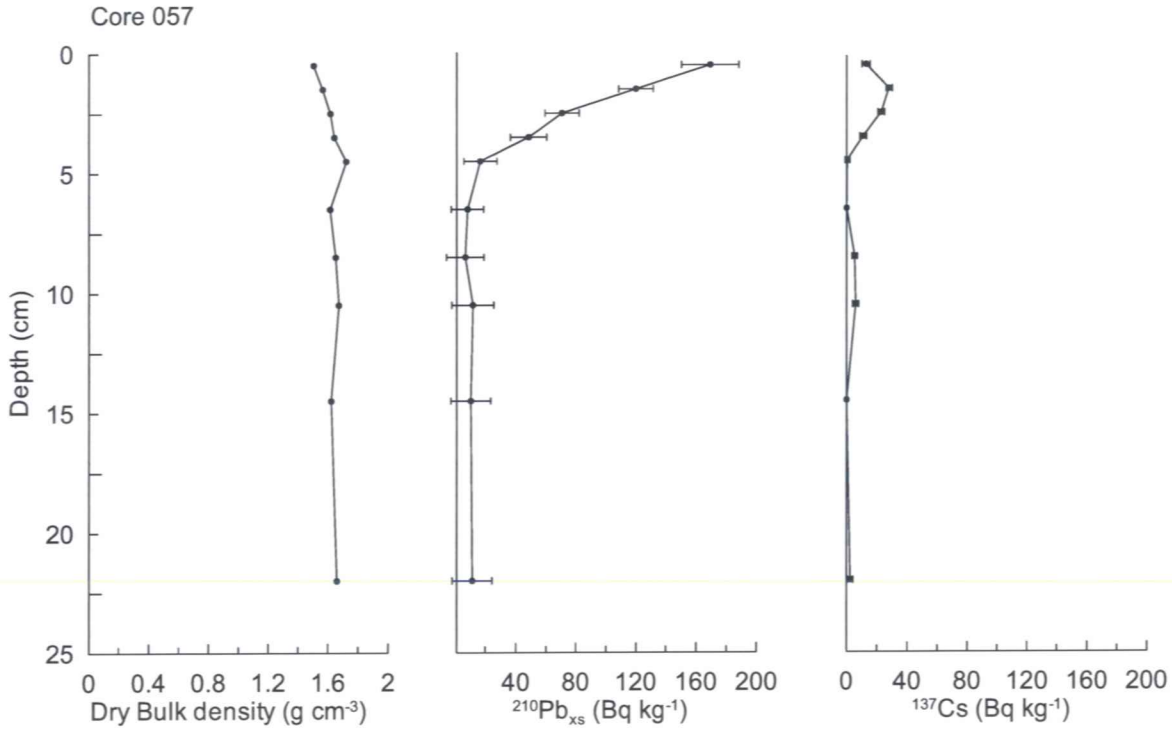
Core 057
Depth (cm)
0
5
10
15
20
25
0 0.4 0.8 1.2 1.6 2
Dry Bulk density (g cm-3)
40 80 120 160 200
210Pbxs (Bq kg-1)
0 40 80 120 160 200
137Cs (Bq kg-1)

Fig 1

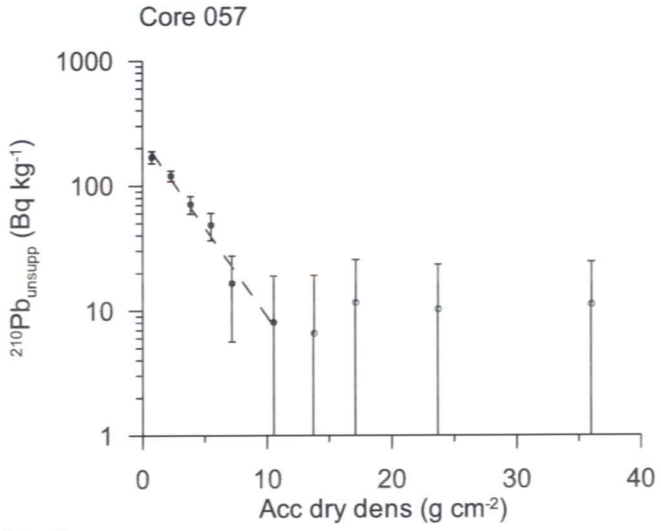
Core 057
1000
100
10
1
210Pbunsupp (Bq kg-1)
0 10 20 30 40
Acc dry dens (g cm-2)

Fig 2

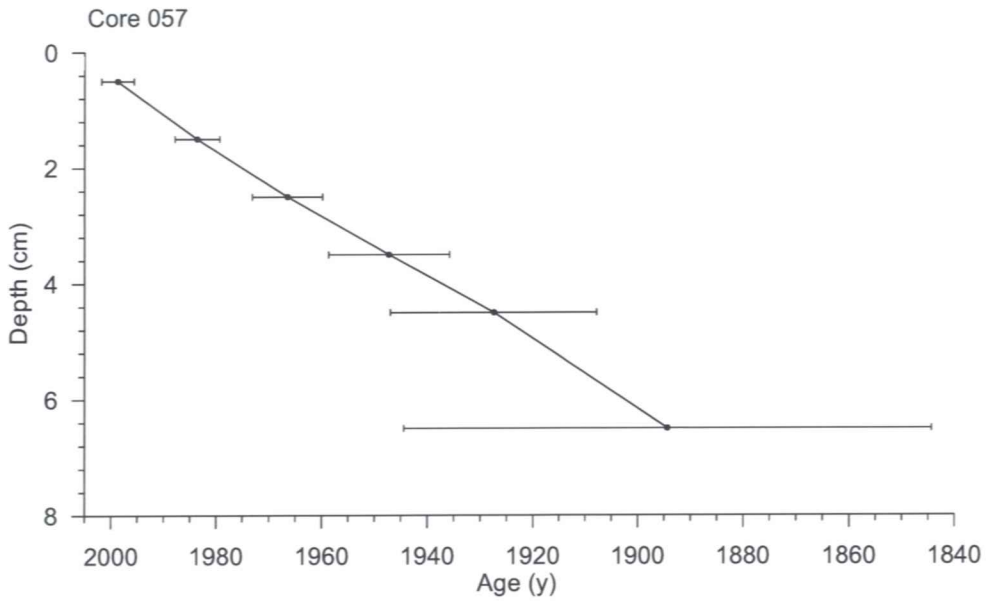
Core 057
0
2
4
6
8
Depth (cm)
2000
1980
1960
1940
1920
1900
1880
1860
1840
Age (y)

Fig 3

Dating of core 066

Methods

The samples have been analysed for the activity of ^{210}Pb, ^{226}Ra and ^{137}Cs via gammaspectrometry at the Gamma Dating Center, Institute of Geography, University of Copenhagen. The measurements were carried out on a Canberra low-background Ge-detector. ^{210}Pb was measured via its gamma-peak at 46,5 keV, ^{226}Ra via the granddaughter ^{214}Pb (peaks at 295 and 352 keV) and ^{137}Cs via its peak at 661 keV.

Results

The core showed high surface contents of unsupported ^{210}Pb and a tendency for an exponential decrease with depth, although with major irregularities. The inventory of unsupported ^{210}Pb is about 460 Bq m^{-2} y^{-1} which is about six times higher than the estimated atmospheric flux at the site. Low contents of ^{137}Cs were found in the upper 8 cm of the core.

CRS-modelling (Appleby, 2001) has been applied on the profile assuming that there is no activity of unsupported ^{210}Pb below 8.5 cm. The result is given in table 2 and fig 2.

The slightly elevated contents ^{137}Cs in the upper part of the core are dated to 1980´s and after, which is in agreement with the expected Chernobyl-origin (1986). However, low levels of ^{137}Cs are also found at levels dated to before the release of this isotope into the environment (around 1954). This shows that some bioturbation/mixing of the surface sediments takes place. Therefore, the ages given in table 2 should be regarded as minimum ages.

10 October 2006

Thorbjørn J Andersen

Reference:
Appleby, P.G. (2001): Chronostratigraphic techniques in recent sediments. In: Last, W.M & Smol, J.P. (eds) Tracking environmental change using lake sediments. Volume 1: Basin analysis, coring and chronological techniques. Kluwer Academic Publishers, the Netherlands.

Table 1. Core 066

Depth	Pb-210tot	error Pb-210 tot	Pb-210 supupp 210Pb	error pb-210 sup	Pb-210 unsup	error pb-210 unsup	Cs-137	error Cs-137
cm	Bq kg-1	Bq kg-1	Bq kg-1	Bq kg-1	Bq kg-1	Bq kg-1	Bq kg-1	Bq kg-1
0.50	419	33	22	21	398	33	17	2
1.50	198	16	12	18	180	18	20	2
2.50	90	9	11	15	75	11	22	3
3.50	171	16	65	60	111	17	10	3
4.50	149	13	21	21	128	13	18	2
6.50	59	5	28	26	33	6	5	1
8.50	7	1	27	26	0	1	0	2
10.50	27	4	23	20	6	5	0	0
12.50	27	4	16	20	7	7	0	2
14.50	15	3	20	23	0	5	0	2

Table 2, Core 066

Depth	acc dry mass	Age	error age	Date	acc rate	error rate
cm	g cm-3	y	y	y	(kg m-2 y-1)	(kg m-2 y-1)
0				2005		
0.5	0.3	3	2	2002	1.1	0.1
1.5	1.8	15	2	1990	1.2	0.1
2.5	3.5	23	2	1982	2.0	0.3
3.5	5.2	32	3	1973	2.1	0.3
4.5	7.0	47	3	1958	1.1	0.1
6.5	10.5	102	12	1903	0.6	0.2

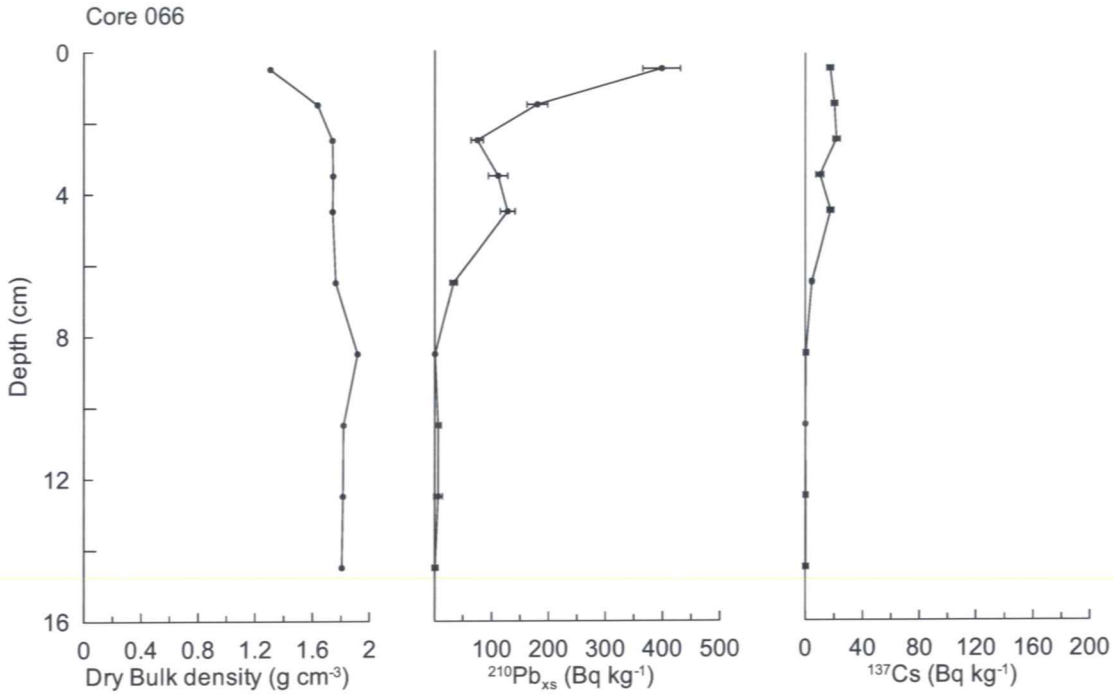
Core 066
Depth (cm)
0
4
8
12
16
0 0.4 0.8 1.2 1.6 2
Dry Bulk density (g cm-3)
100 200 300 400 500
210Pbxs (Bq kg-1)
0 40 80 120 160 200
137Cs (Bq kg-1)

Fig 1

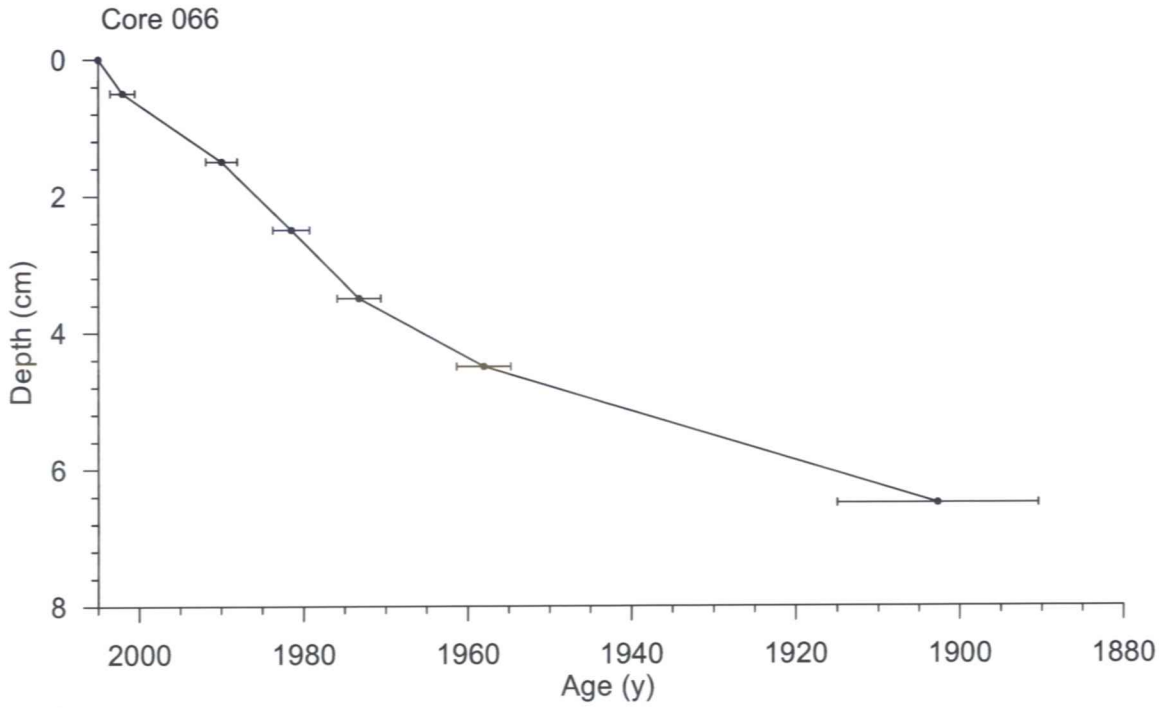
Core 066
Depth (cm)
0
2
4
6
8
2000
1980
1960
1940
1920
1900
1880
Age (y)

Fig 2

Dating of core 080

Methods

The samples have been analysed for the activity of ^{210}Pb, ^{226}Ra and ^{137}Cs via gammaspectrometry at the Gamma Dating Center, Institute of Geography, University of Copenhagen. The measurements were carried out on a Canberra low-background Ge-detector. ^{210}Pb was measured via its gamma-peak at 46,5 keV, ^{226}Ra via the granddaughter ^{214}Pb (peaks at 295 and 352 keV) and ^{137}Cs via its peak at 661 keV.

Results

The core showed moderate surface contents of unsupported ^{210}Pb and an irregular profile downcore. Samples at depths of 8.5 cm and below had contents close to zero. Assuming that the activity is zero at 8.5 cm, the inventory of unsupported ^{210}Pb is about 300 Bq m^{-2} y^{-1} which is about four times higher than the estimated atmospheric flux at the site.
Low contents of ^{137}Cs were found in the upper 5 cm of the core.

CRS-modelling (Appleby, 2001) has been applied on the profile assuming that there is no activity of unsupported ^{210}Pb below 8.5 cm. The result is given in table 2 and fig 2. The dating depends on where the level of zero activity is asumed to be, especially at the lower levels. Therefore, the dating at the lower levels has to be used with this in mind.

The irregular profile of unsupported ^{210}Pb, low levels of ^{137}Cs and possibility of sediment mixing makes dating of this core difficult and the result shown in table 2 and fig 2 is only indicative.

10 October 2006

Thorbjørn J Andersen

Reference:

Appleby, P.G. (2001): Chronostratigraphic techniques in recent sediments. In: Last, W.M & Smol, J.P. (eds) Tracking environmental change using lake sediments. Volume 1: Basin analysis, coring and chronological techniques. Kluwer Academic Publishers, the Netherlands.

Table 1. Core 080

Depth	Pb-210tot	error Pb-210 tot	Pb-210 supupp 210Pb	error pb-210 sup	Pb-210 unsup	error pb-210 unsup	Cs-137	error Cs-137
cm	Bq kg-1	Bq kg-1	Bq kg-1	Bq kg-1	Bq kg-1	Bq kg-1	Bq kg-1	Bq kg-1
0.5	243	13	22	2	222	14	13	2
1.5	116	13	26	0	89	13	8	2
2.5	113	8	19	1	94	8	18	1
3.5	114	11	27	8	87	14	17	2
4.5	40	12	23	9	17	15	5	2
6.5	38	11	24	2	14	11	1	2
8.5	33	11	34	4	0	12	0	0
10.5	22	10	32	5	0	11	0	1
14.5	9	13	35	8	0	15	0	0
24	48	12	39	7	9	14	2	2

Table 2, Core 080

Depth cm	acc dry mass g cm-3	Age y	error age y	Date y	acc rate (kg m-2 y-1)	error rate (kg m-2 y-1)
0				2005		
0.5	0.9	7	3	1998	1.2	0.1
1.5	2.7	21	4	1984	1.3	0.2
2.5	4.5	34	6	1971	1.4	0.3
3.5	6.3	55	12	1950	0.9	0.4
4.5	8.2	80	24	1925	0.7	0.7
6.5	11.8	118	74	1887	1.0	2.3

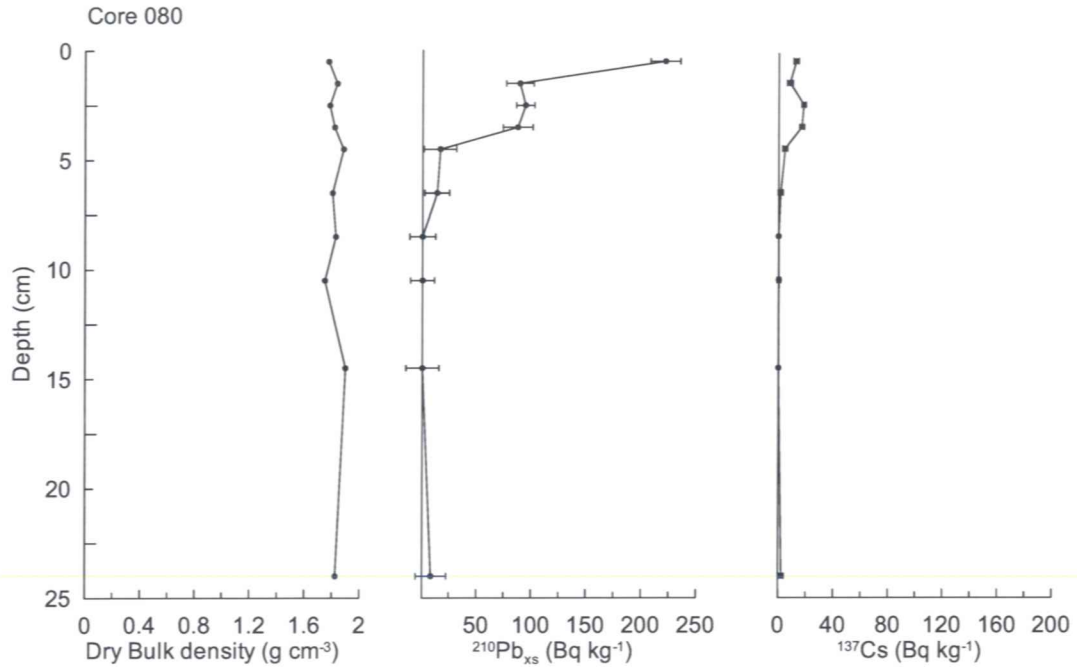
Core 080
Depth (cm)
0
5
10
15
20
25
0 0.4 0.8 1.2 1.6 2
Dry Bulk density (g cm-3)
50 100 150 200 250
210Pbxs (Bq kg-1)
0 40 80 120 160 200
137Cs (Bq kg-1)

Fig 1

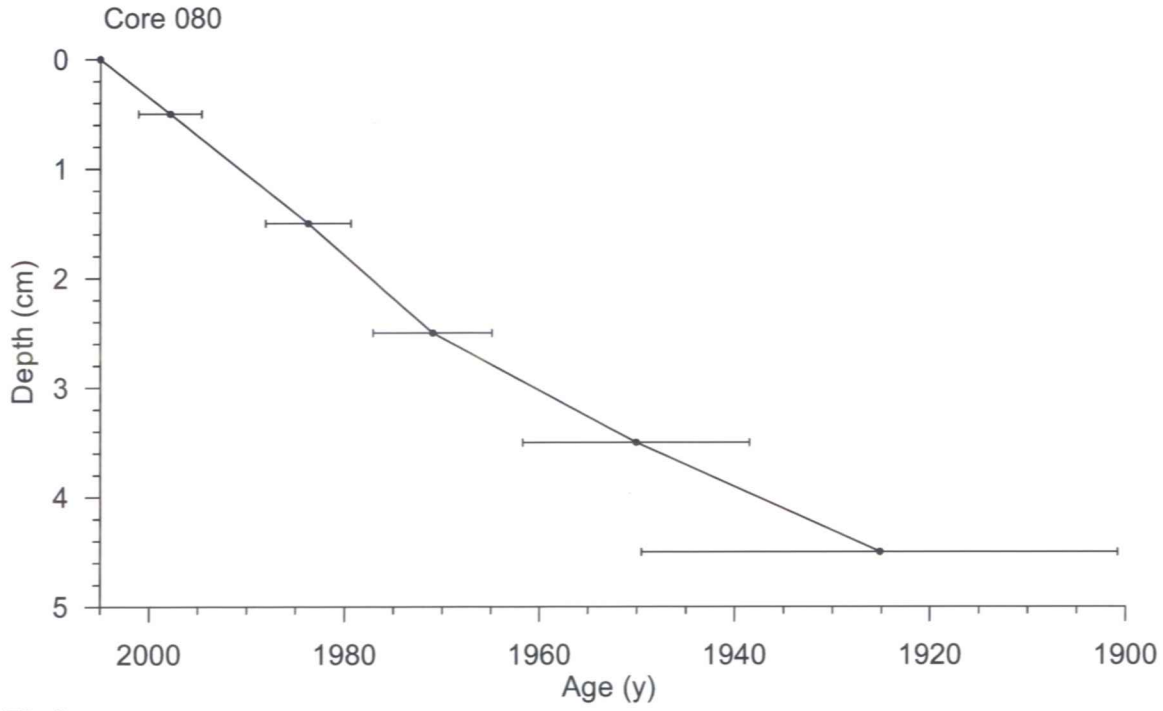
Core 080
Depth (cm)
0
1
2
3
4
5
2000
1980
1960
1940
1920
1900
Age (y)

Fig 2

Dating of core 085

Methods

The samples have been analysed for the activity of ^{210}Pb, ^{226}Ra and ^{137}Cs via gammaspectrometry at the Gamma Dating Center, Institute of Geography, University of Copenhagen. The measurements were carried out on a Canberra low-background Ge-detector. ^{210}Pb was measured via its gamma-peak at 46,5 keV, ^{226}Ra via the granddaughter ^{214}Pb (peaks at 295 and 352 keV) and ^{137}Cs via its peak at 661 keV.

Results

The core showed moderate surface contents of unsupported ^{210}Pb and a decrease downcore, although with major irregularities. Samples at depths of 6.5 cm and below had contents close to zero. Assuming that the activity is zero at 6.5 cm, the inventory of unsupported ^{210}Pb is about 190 Bq m^{-2} y^{-1} which is about two to three times higher than the estimated atmospheric flux at the site. Low contents of ^{137}Cs were found in the upper 4 cm of the core.

CRS-modelling (Appleby, 2001) has been applied on the profile assuming that there is no activity of unsupported ^{210}Pb below 6.5 cm. The result is given in table 2 and fig 2.

The dating should be treated with caution as it is only based on five slices with measurable contents of unsupported ^{210}Pb.

11 October 2006

Thorbjørn J Andersen

Reference:
Appleby, P.G. (2001): Chronostratigraphic techniques in recent sediments. In: Last, W.M & Smol, J.P. (eds) Tracking environmental change using lake sediments. Volume 1: Basin analysis, coring and chronological techniques. Kluwer Academic Publishers, the Netherlands.

Table 1. Core 085

Depth cm	Pb-210tot Bq kg-1	error Pb-210 tot Bq kg-1	Pb-210 supupp 210Pb Bq kg-1	error pb-210 sup Bq kg-1	Pb-210 unsup Bq kg-1	error pb-210 unsup Bq kg-1	Cs-137 Bq kg-1	error Cs-137 Bq kg-1
0.5	127	8	27	3	100	9	2	2
1.5	105	12	19	1	86	12	0	3
2.5	119	12	14	23	94	14	12	3
3.5	65	11	42	2	22	11	5	2
4.5	39	10	31	0	8	10	1	2
6.5	34	12	37	0	0	12	2	3
8.5	19	10	30	2	0	10	0	2
10.5	22	11	37	7	0	13	0	0
14.5	19	11	27	0	0	11	0	0
20	14	12	36	5	0	13	1	2

Table 2, Core 085

Depth cm	acc dry mass g cm-3	Age y	error age y	Date y	acc rate (kg m-2 y-1)	error rate (kg m-2 y-1)
0.0				2005		
0.5	0.9	6	4	1999	1.6	0.3
1.5	2.7	19	6	1986	1.3	0.3
2.5	4.6	43	11	1962	0.8	0.3
3.5	6.4	83	37	1922	0.5	0.6

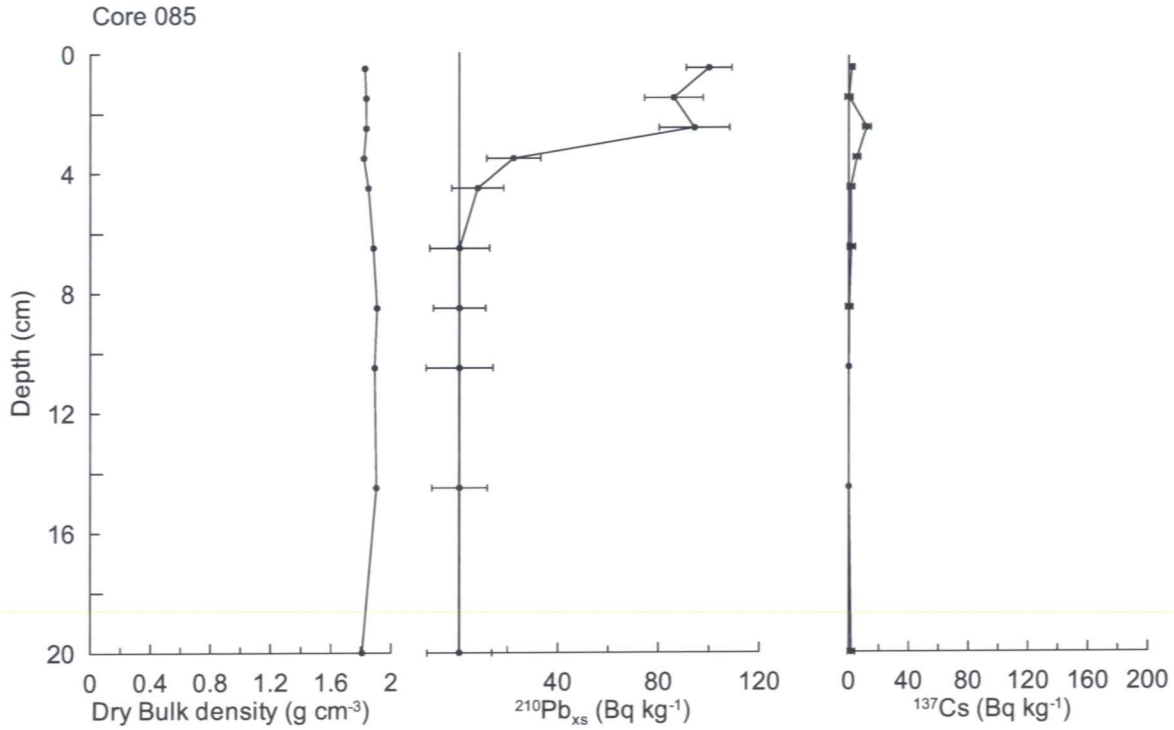
Core 085
Depth (cm)
0
4
8
12
16
20
0 0.4 0.8 1.2 1.6 2
Dry Bulk density (g cm-3)
40 80 120
210Pbxs (Bq kg-1)
0 40 80 120 160 200
137Cs (Bq kg-1)

Fig 1

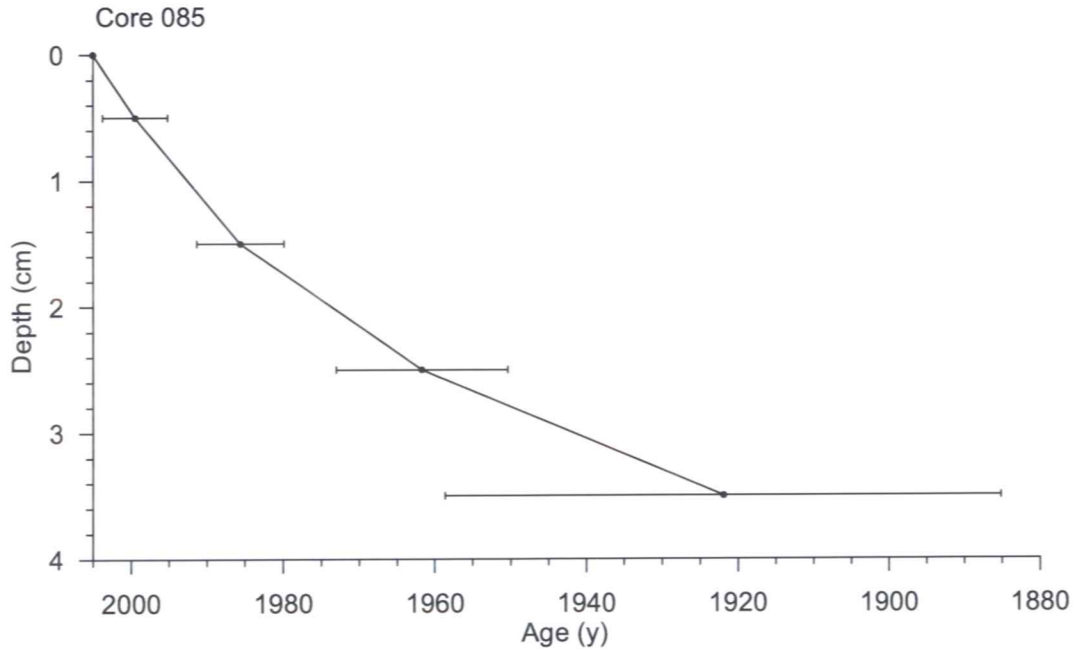
Core 085
Depth (cm)
0
1
2
3
4
2000
1980
1960
1940
1920
1900
1880
Age (y)

Fig 2

Dating of core 095

Methods

The samples have been analysed for the activity of ^{210}Pb, ^{226}Ra and ^{137}Cs via gammaspectrometry at the Gamma Dating Center, Institute of Geography, University of Copenhagen. The measurements were carried out on a Canberra low-background Ge-detector. ^{210}Pb was measured via its gamma-peak at 46,5 keV, ^{226}Ra via the granddaughter ^{214}Pb (peaks at 295 and 352 keV) and ^{137}Cs via its peak at 661 keV.

Results

The core showed moderate surface contents of unsupported ^{210}Pb and a decrease downcore. Samples at depths of 4.5 cm and below had contents close to zero. Assuming that the activity is zero at 4.5 cm, the inventory of unsupported ^{210}Pb is about 170 Bq m^{-2} y^{-1} which is about two to three times higher than the estimated atmospheric flux at the site.
Low contents of ^{137}Cs were found in the upper 4 cm of the core.

CRS-modelling (Appleby, 2001) has been applied on the profile assuming that there is no activity of unsupported ^{210}Pb below 4.5 cm. The result is given in table 2 and fig 2.

The dating should be treated with caution as it is only based on four slices with measurable contents of unsupported ^{210}Pb.

10 October 2006

Thorbjørn J Andersen

Reference:
Appleby, P.G. (2001): Chronostratigraphic techniques in recent sediments. In: Last, W.M & Smol, J.P. (eds) Tracking environmental change using lake sediments. Volume 1: Basin analysis, coring and chronological techniques. Kluwer Academic Publishers, the Netherlands.

Table 1. Core 095

Depth	Pb-210tot	error Pb-210 tot	Pb-210 supupp 210Pb	error pb-210 sup	Pb-210 unsup	error pb-210 unsup	Cs-137	error Cs-137
cm	Bq kg-1	Bq kg-1	Bq kg-1	Bq kg-1	Bq kg-1	Bq kg-1	Bq kg-1	Bq kg-1
0.5	177	16	28	2	149	16	6	2
1.5	125	11	24	1	100	11	9	2
2.5	94	9	27	2	66	9	11	2
3.5	31	4	26	2	5	5	5	2
4.5	19	3	19	8	0	8	0	2
6.5	22	3	22	0	0	3	0	1
8.5	13	2	31	6	0	6	1	2
10.5	22	3	30	1	0	4	1	2
14.5	30	4	29	3	1	5	2	2
18.5	29	4	28	4	1	6	0	0

Table 2, Core 095

Depth cm	acc dry mass g cm-3	Age y	error age y	Date y	acc rate (kg m-2 y-1)	error rate (kg m-2 y-1)
0.0				2005		
0.5	0.9	8	4	1997	1.0	0.2
1.5	2.6	31	8	1974	0.8	0.2
2.5	4.3	66	23	1939	0.5	0.4

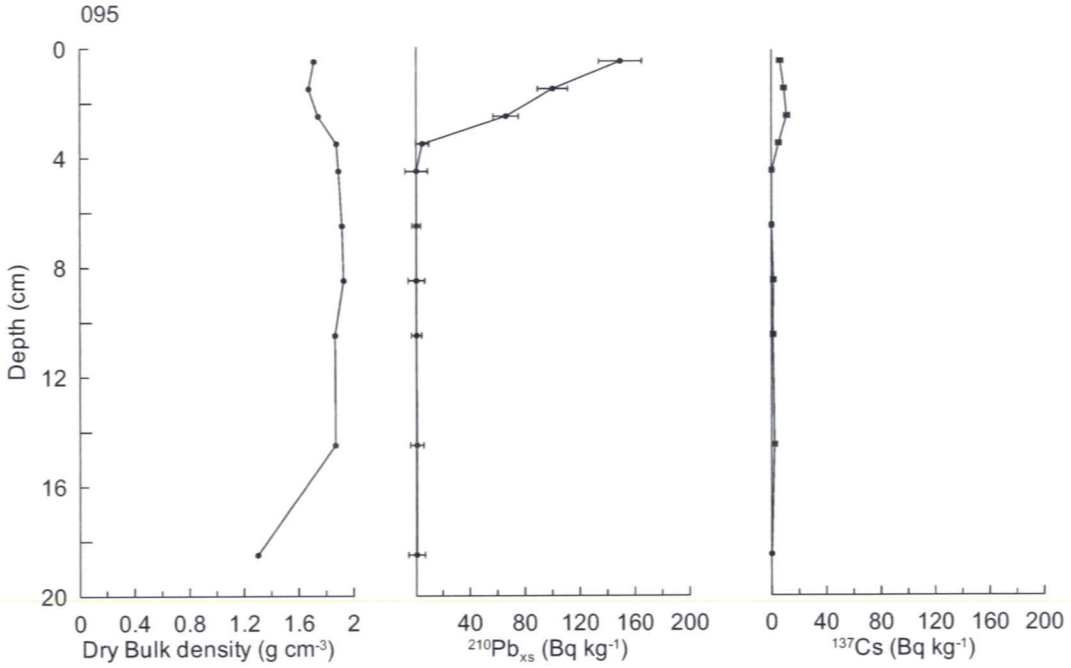
095
Depth (cm)
0
4
8
12
16
20
0 0.4 0.8 1.2 1.6 2
Dry Bulk density (g cm-3)
40 80 120 160 200
210Pbxs (Bq kg-1)
0 40 80 120 160 200
137Cs (Bq kg-1)

Fig 1

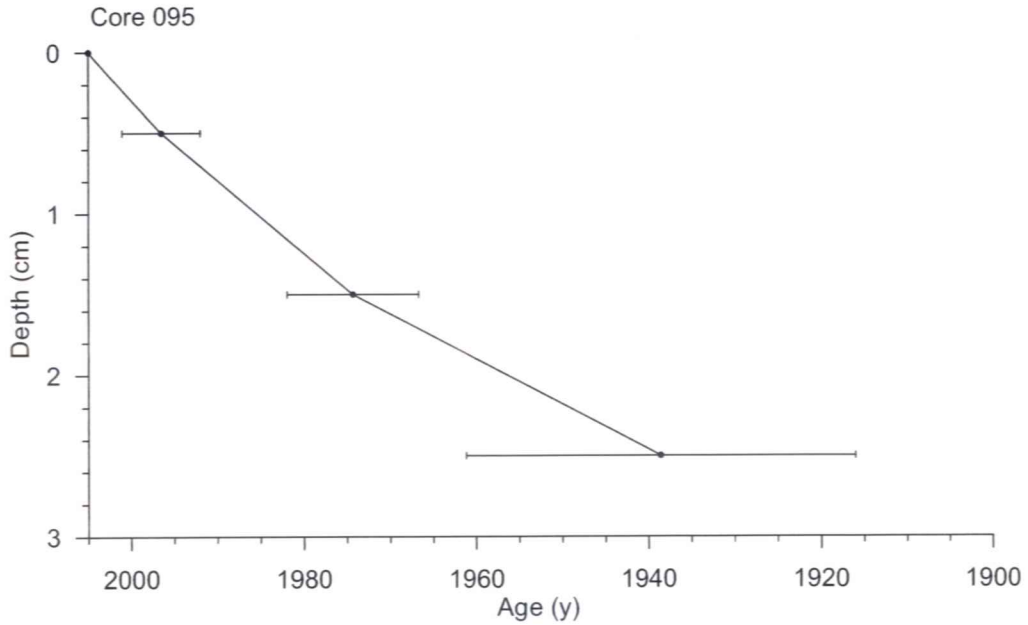
Core 095
Depth (cm)
0
1
2
3
2000
1980
1960
1940
1920
1900
Age (y)

Fig 2

Appendix 5. Lithologic descriptions, optical images, radiographs and stratigraphic profiles of selected major and trace elements obtained with the aid of XRF core logger.

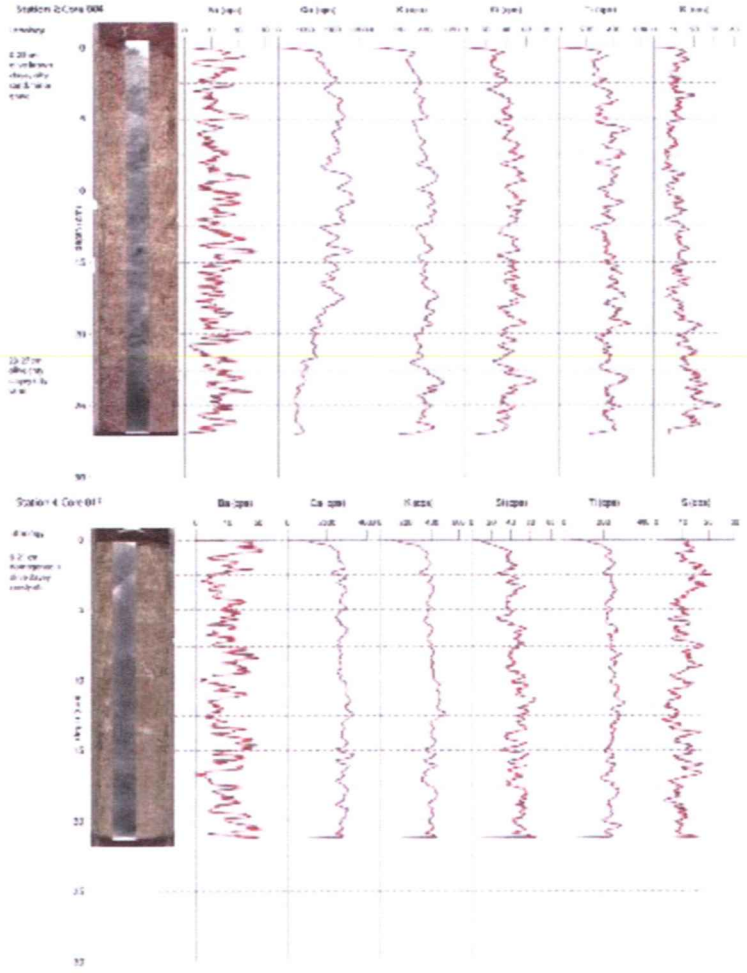

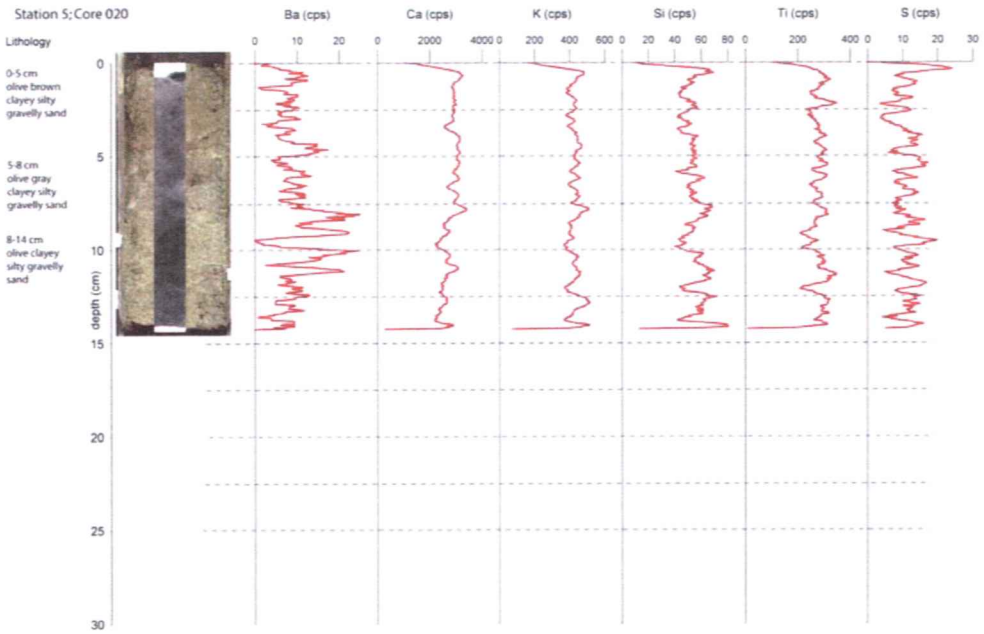
Station 5; Core 020
Lithology
0-5 cm
olive brown
clayey silty
gravelly sand
5-8 cm
olive gray
clayey silty
gravelly sand
8-14 cm
olive clayey
silty gravelly
sand
depth (cm)
Ba (cps)
Ca (cps)
K (cps)
Si (cps)
Ti (cps)
S (cps)

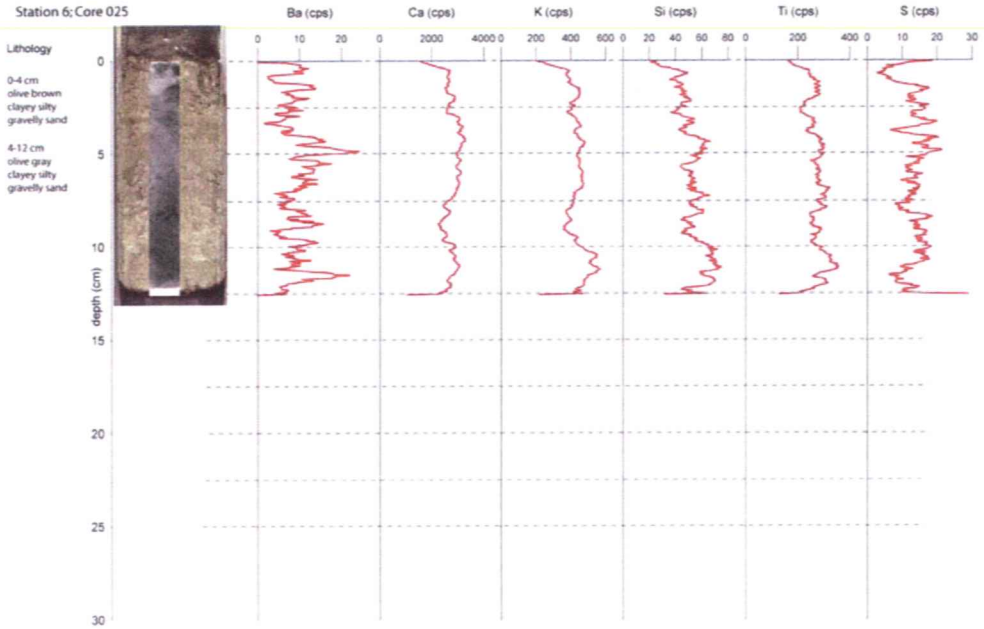
Station 6; Core 025
Lithology
0-4 cm
olive brown
clayey silty
gravelly sand
4-12 cm
olive gray
clayey silty
gravelly sand
depth (cm)
Ba (cps)
Ca (cps)
K (cps)
Si (cps)
Ti (cps)
S (cps)

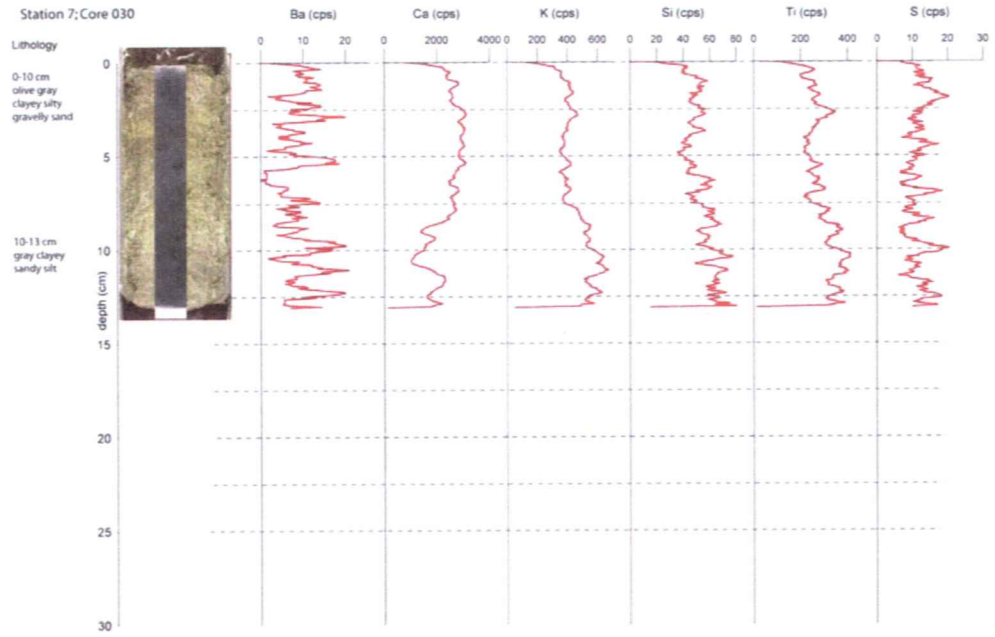
Station 7; Core 030
Lithology
0-10 cm
olive gray
clayey silty
gravelly sand
10-13 cm
gray clayey
sandy silt
depth (cm)
Ba (cps)
Ca (cps)
K (cps)
Si (cps)
Ti (cps)
S (cps)

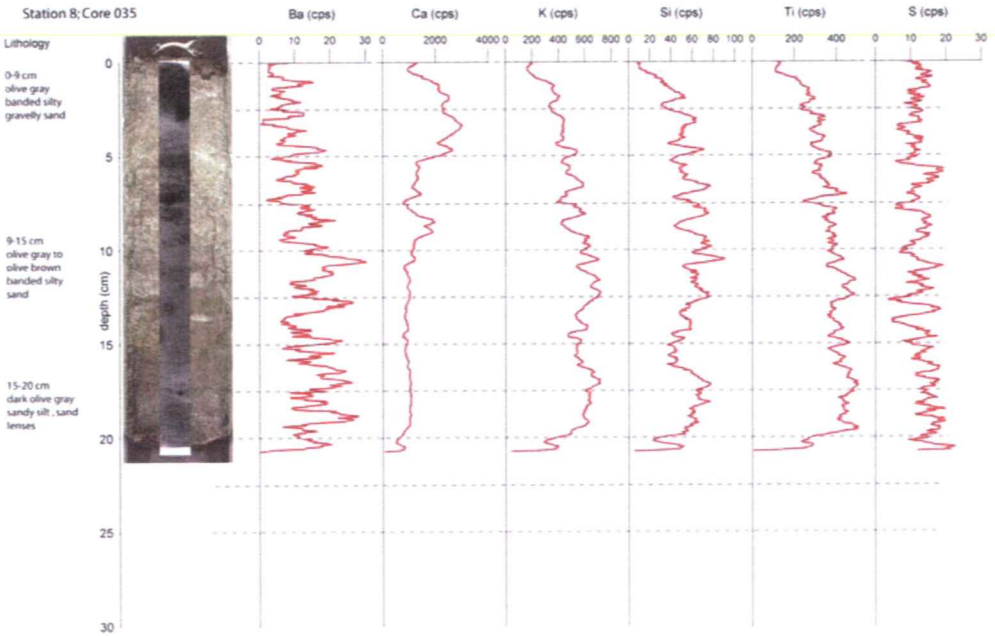
Station 8; Core 035
Lithology
0-9 cm
olive gray
banded silty
gravelly sand
9-15 cm
olive gray to
olive brown
banded silty
sand
15-20 cm
dark olive gray
sandy silt , sand
lenses
depth (cm)
Ba (cps)
Ca (cps)
K (cps)
Si (cps)
Ti (cps)
S (cps)

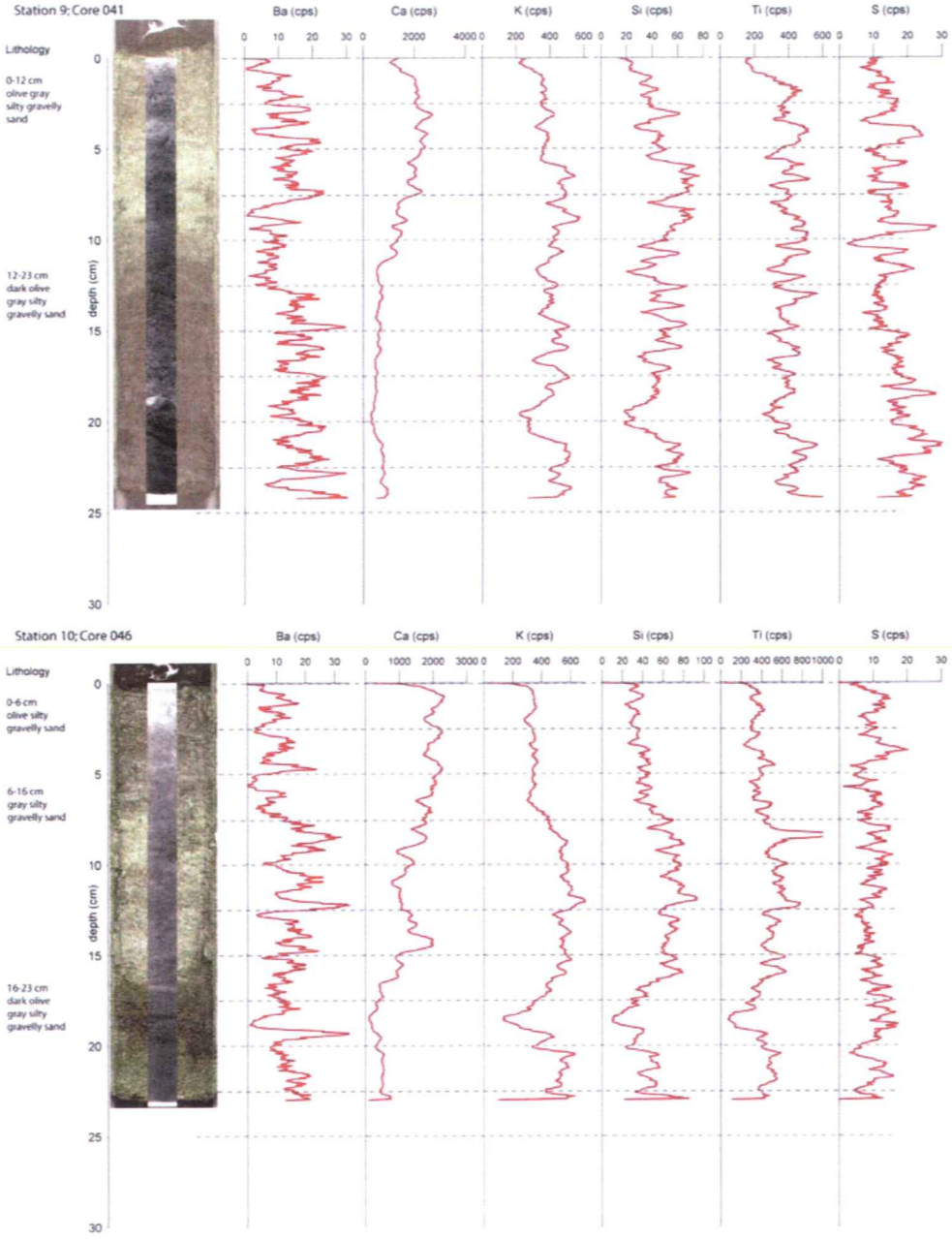
Station 9; Core 041
Lithology
0-12 cm
olive gray
silty gravelly
sand
12-23 cm
dark olive
gray silty
gravelly sand
depth (cm)
Ba (cps)
Ca (cps)
K (cps)
Si (cps)
Ti (cps)
S (cps)
Station 10; Core 046
Lithology
0-6 cm
olive silty
gravelly sand
6-16 cm
gray silty
gravelly sand
16-23 cm
dark olive
gray silty
gravelly sand
depth (cm)
Ba (cps)
Ca (cps)
K (cps)
Si (cps)
Ti (cps)
S (cps)

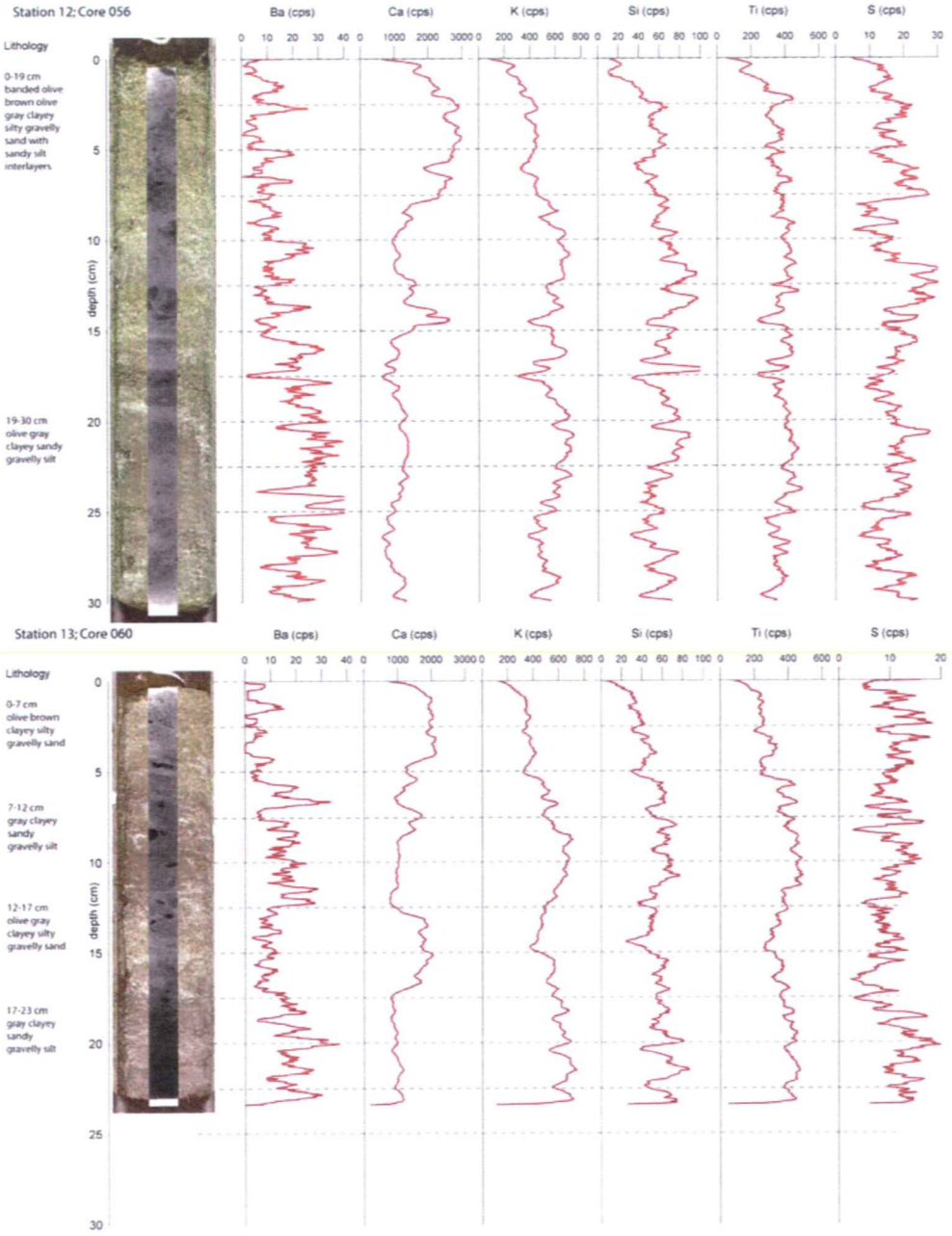
Station 12; Core 056
Lithology
0-19 cm
banded olive brown olive gray clayey silty gravelly sand with sandy silt interlayers
19-30 cm
olive gray clayey sandy gravelly silt
depth (cm)
Ba (cps)
Ca (cps)
K (cps)
Si (cps)
Ti (cps)
S (cps)
Station 13; Core 060
Lithology
0-7 cm
olive brown clayey silty gravelly sand
7-12 cm
gray clayey sandy gravelly silt
12-17 cm
olive gray clayey silty gravelly sand
17-23 cm
gray clayey sandy gravelly silt
depth (cm)
Ba (cps)
Ca (cps)
K (cps)
Si (cps)
Ti (cps)
S (cps)

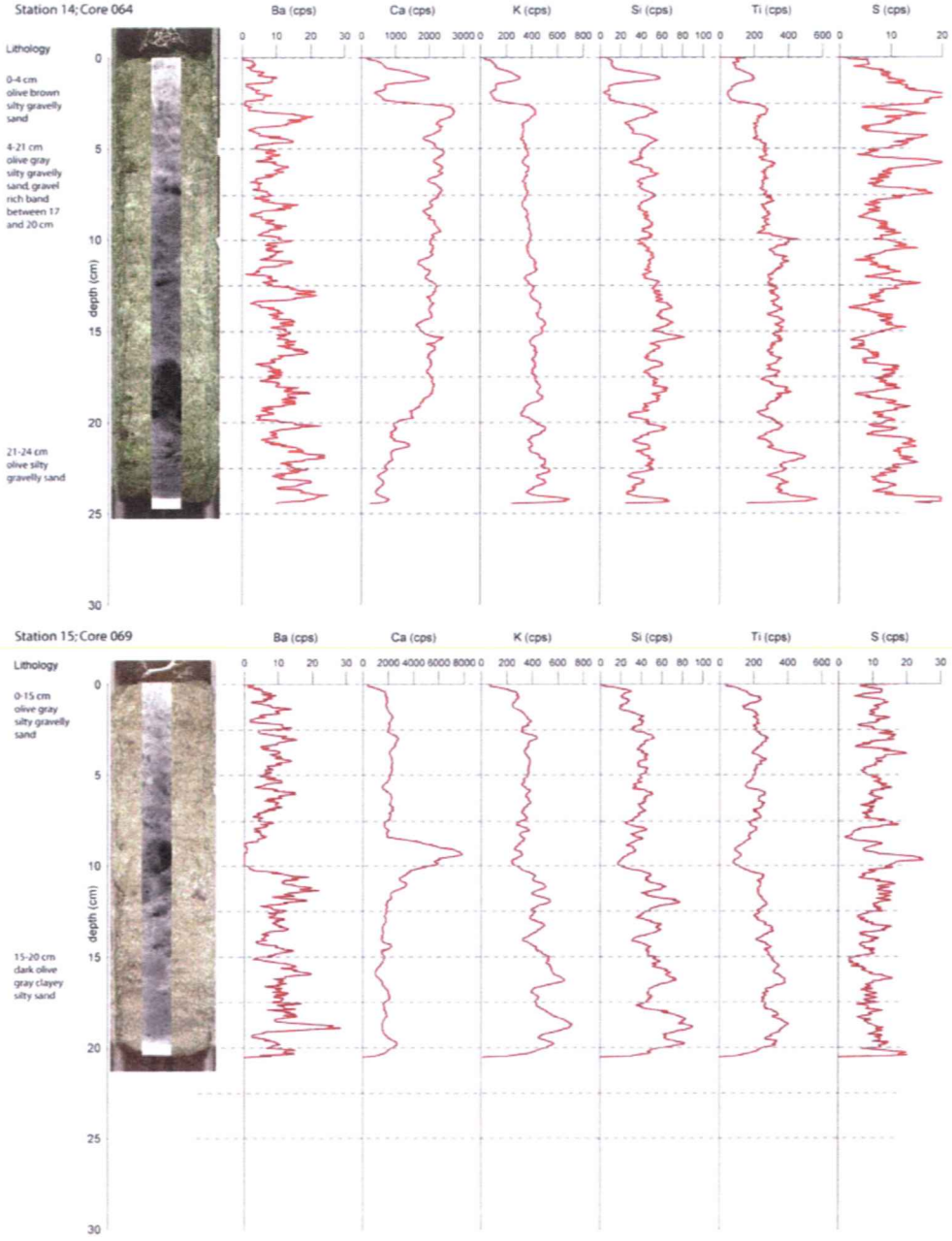
Station 14; Core 064
Lithology
0-4 cm olive brown silty gravelly sand
4-21 cm olive gray silty gravelly sand, gravel rich band between 17 and 20 cm
21-24 cm olive silty gravelly sand
depth (cm)
Ba (cps)
Ca (cps)
K (cps)
Si (cps)
Ti (cps)
S (cps)
Station 15; Core 069
Lithology
0-15 cm olive gray silty gravelly sand
15-20 cm dark olive gray clayey silty sand
depth (cm)
Ba (cps)
Ca (cps)
K (cps)
Si (cps)
Ti (cps)
S (cps)

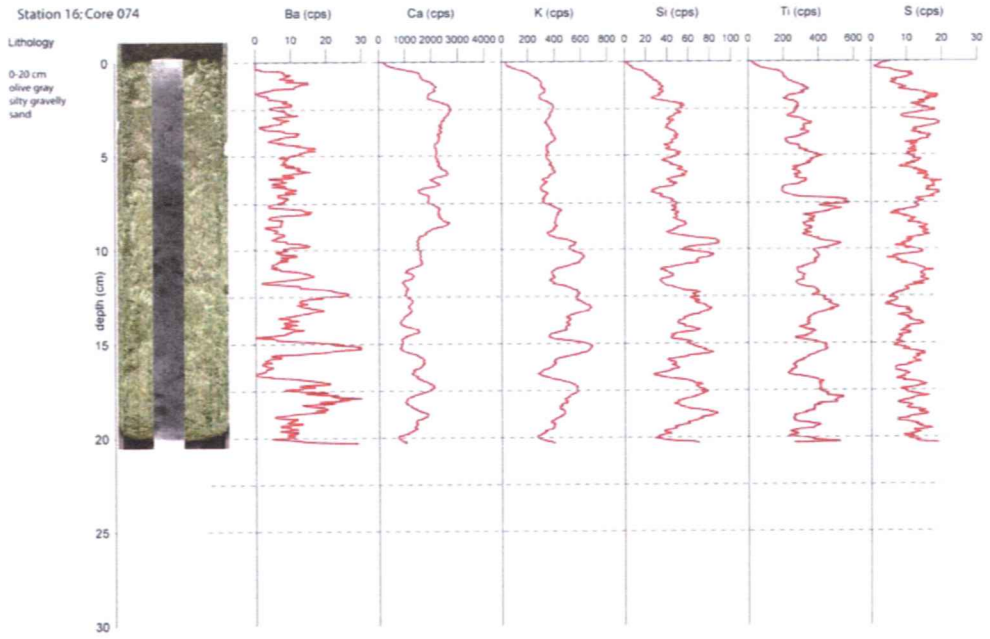
Station 16; Core 074
Lithology
0-20 cm
olive gray
silty gravelly
sand
depth (cm)
Ba (cps)
Ca (cps)
K (cps)
Si (cps)
Ti (cps)
S (cps)

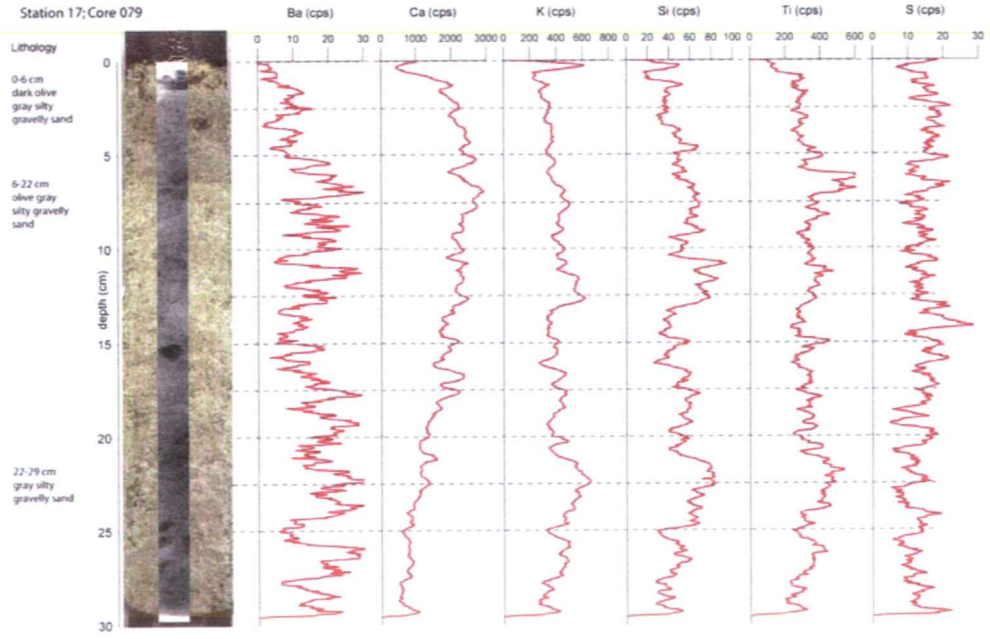
Station 17; Core 079
Lithology
0-6 cm
dark olive
gray silty
gravelly sand
6-22 cm
olive gray
silty gravelly
sand
22-29 cm
gray silty
gravelly sand
depth (cm)
Ba (cps)
Ca (cps)
K (cps)
Si (cps)
Ti (cps)
S (cps)

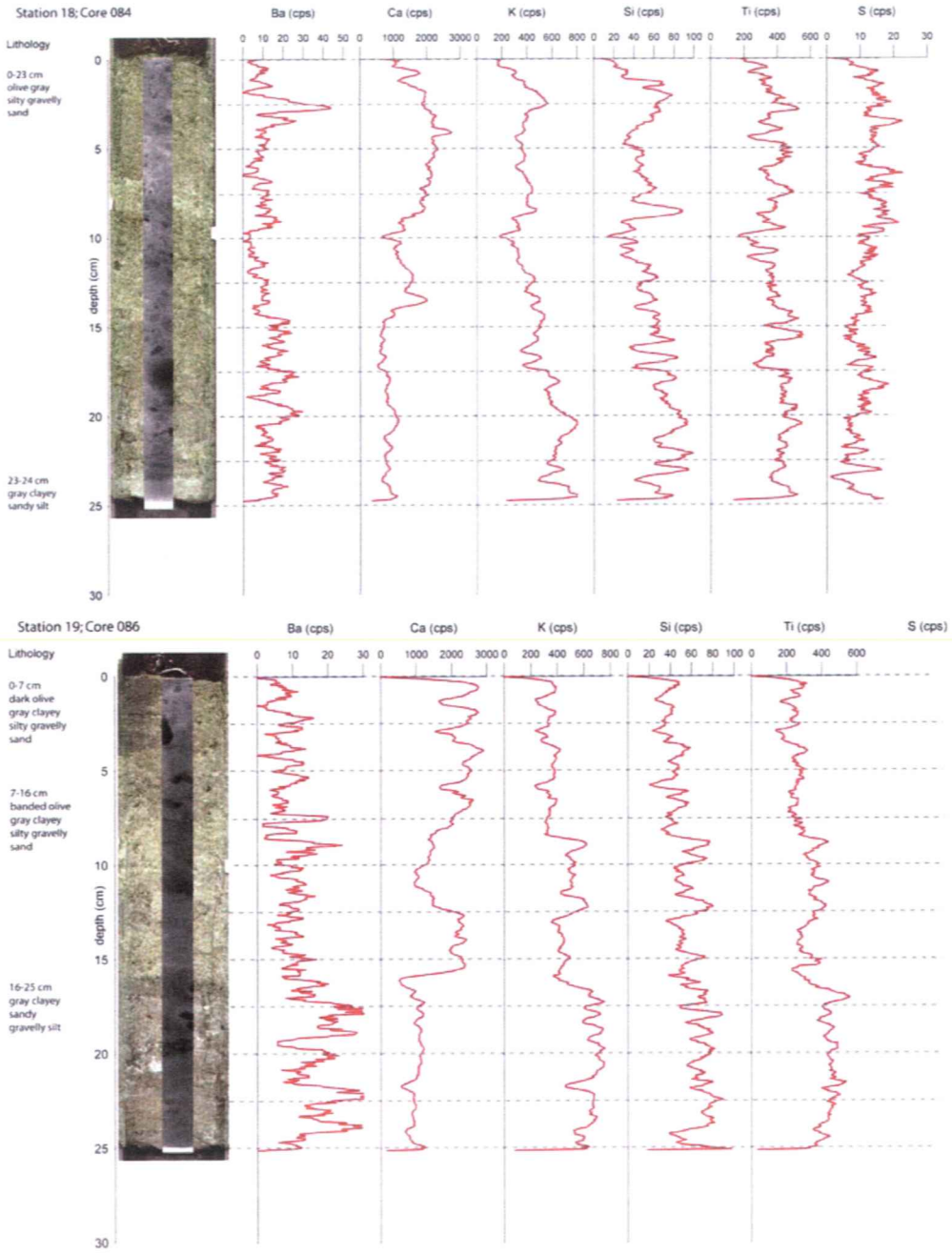
Station 18; Core 084
Lithology
0-23 cm
olive gray
silty gravelly
sand
23-24 cm
gray clayey
sandy silt
depth (cm)
Ba (cps)
Ca (cps)
K (cps)
Si (cps)
Ti (cps)
S (cps)
Station 19; Core 086
Lithology
0-7 cm
dark olive
gray clayey
silty gravelly
sand
7-16 cm
banded olive
gray clayey
silty gravelly
sand
16-25 cm
gray clayey
sandy
gravelly silt
depth (cm)
Ba (cps)
Ca (cps)
K (cps)
Si (cps)
Ti (cps)
S (cps)

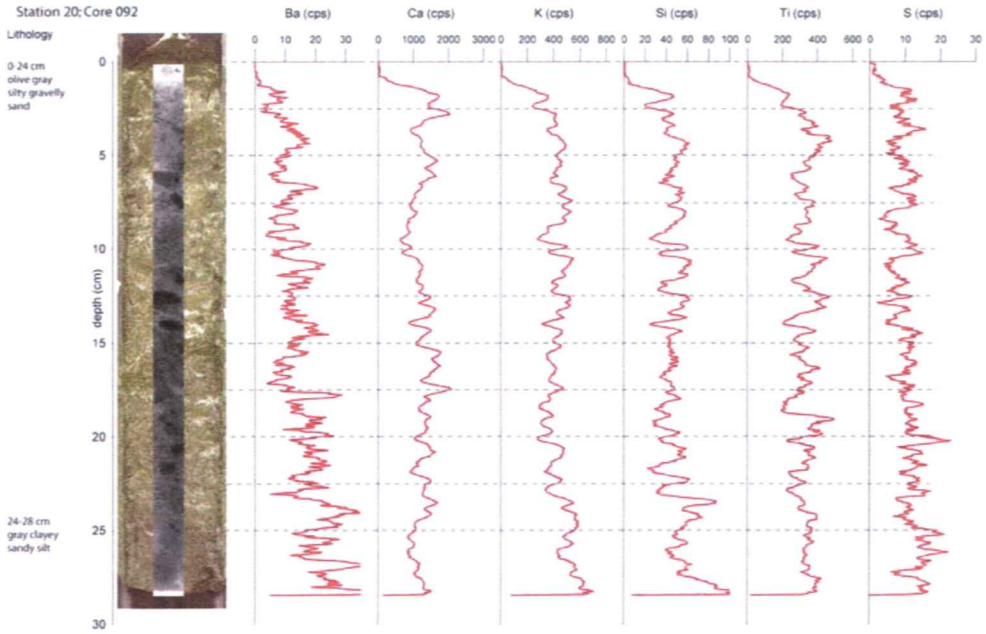
Station 20: Core 092
Lithology
0-24 cm
olive gray
silty gravelly
sand
24-28 cm
gray clayey
sandy silt
depth (cm)
0
5
10
15
20
25
30
Ba (cps)
0 10 20 30
Ca (cps)
0 1000 2000 3000
K (cps)
0 200 400 600 800
Si (cps)
0 20 40 60 80 100
Ti (cps)
0 200 400 600
S (cps)
0 10 20 30

Appendix 6. Lithologic descriptions, optical images, radiographs and stratigraphic profiles of selected major and trace elements obtained with the aid of XRF core logger.

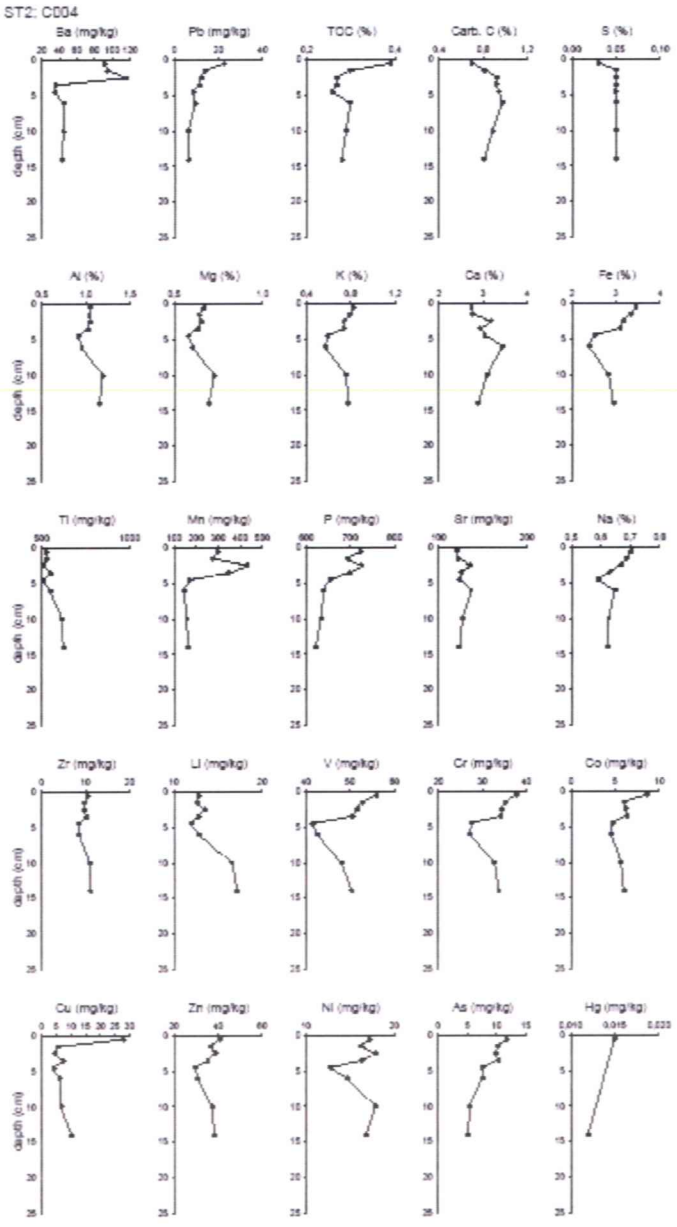

ST4; C017

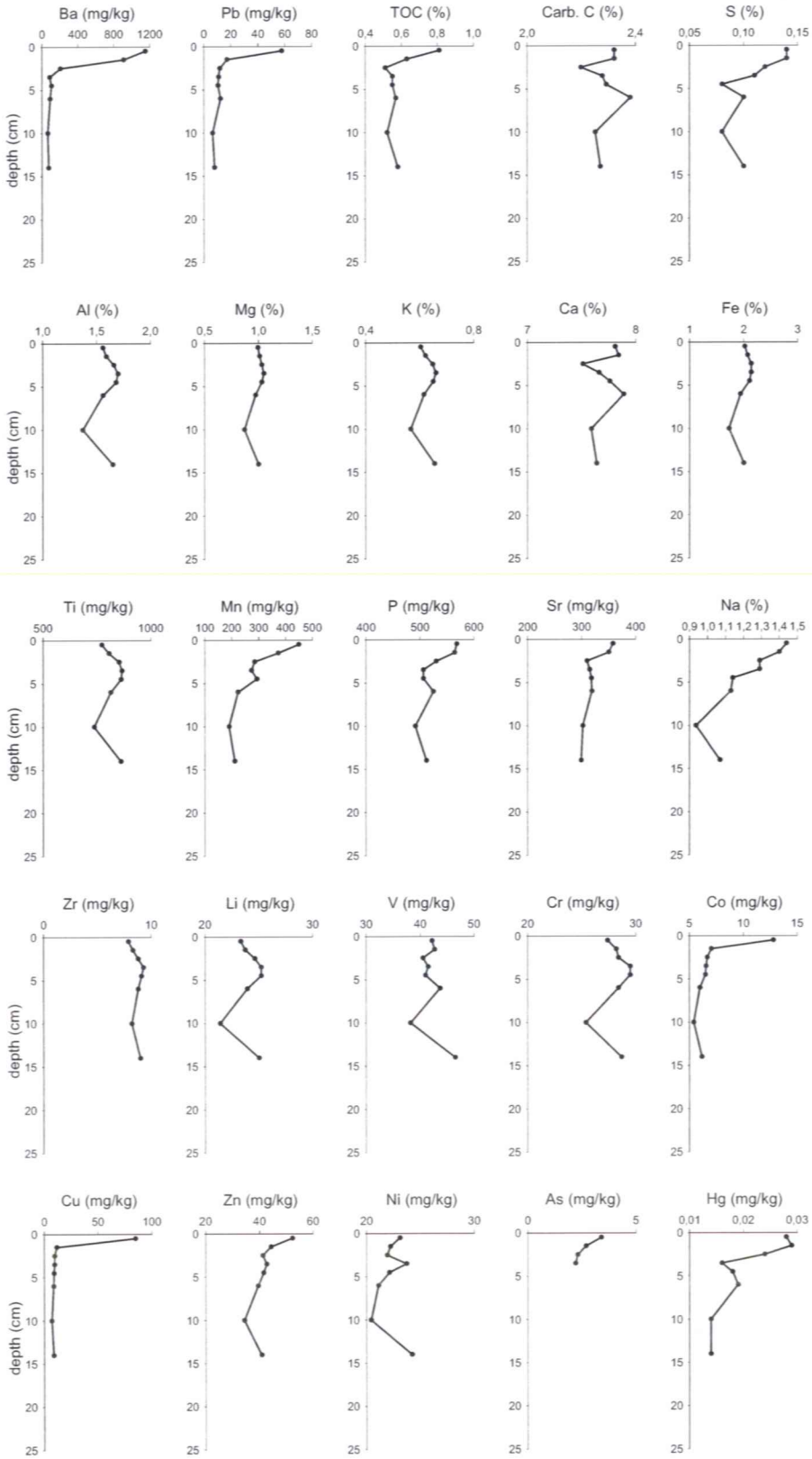
Ba (mg/kg)
0 400 800 1200
Pb (mg/kg)
0 20 40 60 80
TOC (%)
0,4 0,6 0,8 1,0
Carb. C (%)
2,0 2,4
S (%)
0,05 0,10 0,15
Al (%)
1,0 1,5 2,0
Mg (%)
0,5 1,0 1,5
K (%)
0,4 0,8
Ca (%)
7 8
Fe (%)
1 2 3
Ti (mg/kg)
500 1000
Mn (mg/kg)
100 200 300 400 500
P (mg/kg)
400 500 600
Sr (mg/kg)
200 300 400
Na (%)
0,9 1,0 1,1 1,2 1,3 1,4 1,5
Zr (mg/kg)
0 10
Li (mg/kg)
20 30
V (mg/kg)
30 40 50
Cr (mg/kg)
20 30
Co (mg/kg)
5 10 15
Cu (mg/kg)
0 50 100
Zn (mg/kg)
20 40 60
Ni (mg/kg)
20 30
As (mg/kg)
0 5
Hg (mg/kg)
0,01 0,02 0,03
depth (cm)
0 5 10 15 20 25

ST5; C020

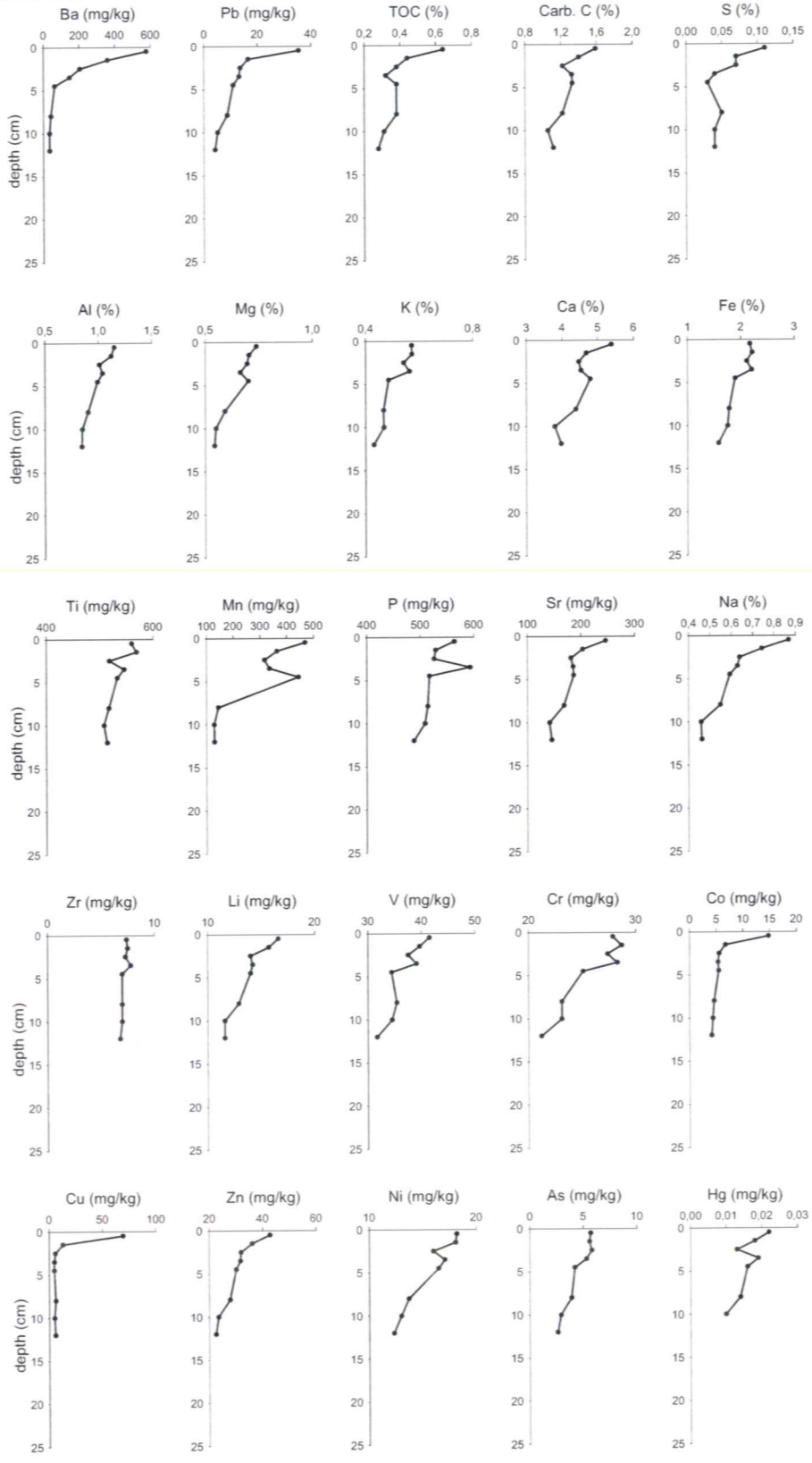
Ba (mg/kg)
Pb (mg/kg)
TOC (%)
Carb. C (%)
S (%)
Al (%)
Mg (%)
K (%)
Ca (%)
Fe (%)
Ti (mg/kg)
Mn (mg/kg)
P (mg/kg)
Sr (mg/kg)
Na (%)
Zr (mg/kg)
Li (mg/kg)
V (mg/kg)
Cr (mg/kg)
Co (mg/kg)
Cu (mg/kg)
Zn (mg/kg)
Ni (mg/kg)
As (mg/kg)
Hg (mg/kg)
depth (cm)

ST6; C025

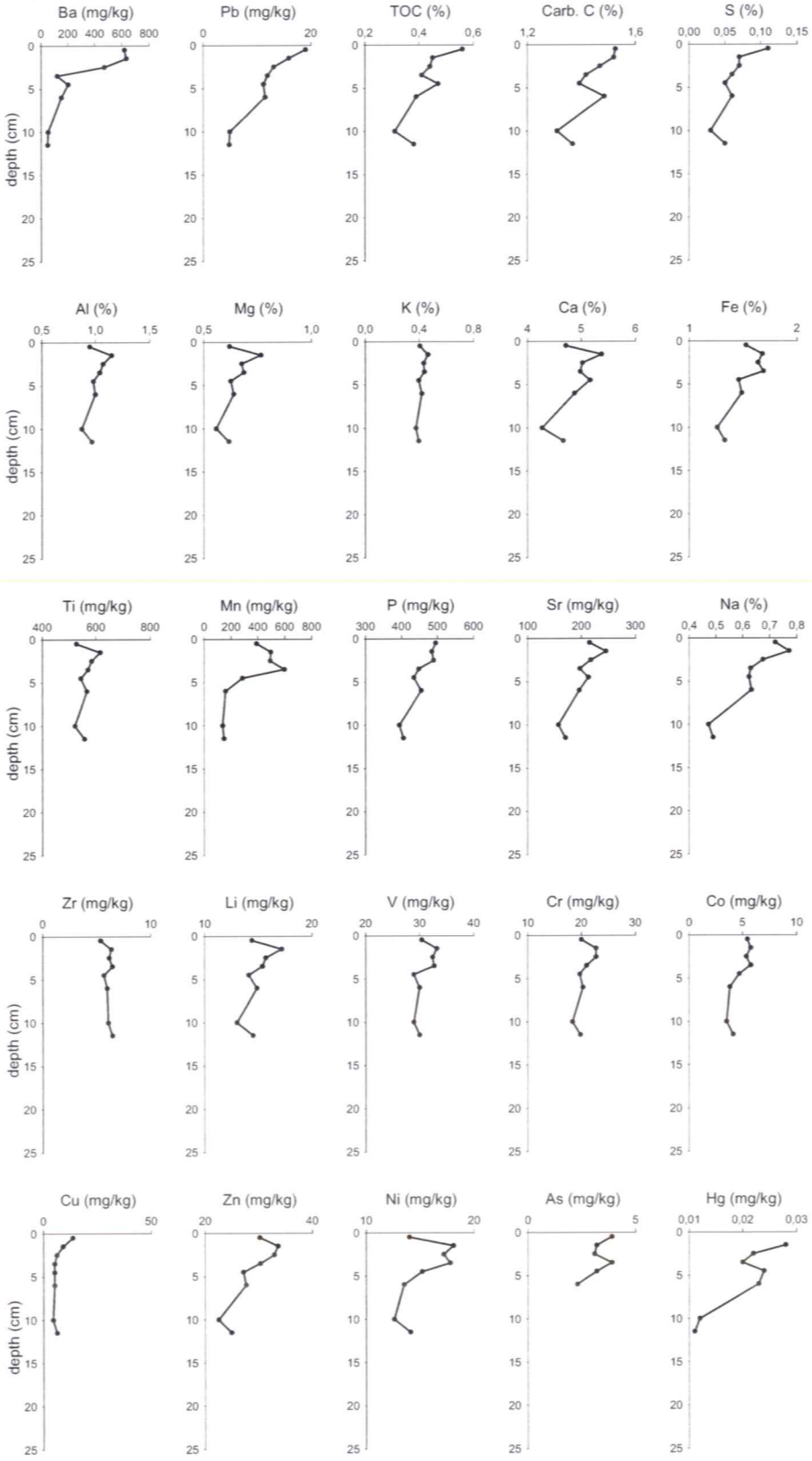
Ba (mg/kg)
Pb (mg/kg)
TOC (%)
Carb. C (%)
S (%)
Al (%)
Mg (%)
K (%)
Ca (%)
Fe (%)
Ti (mg/kg)
Mn (mg/kg)
P (mg/kg)
Sr (mg/kg)
Na (%)
Zr (mg/kg)
Li (mg/kg)
V (mg/kg)
Cr (mg/kg)
Co (mg/kg)
Cu (mg/kg)
Zn (mg/kg)
Ni (mg/kg)
As (mg/kg)
Hg (mg/kg)
depth (cm)

ST7; C030

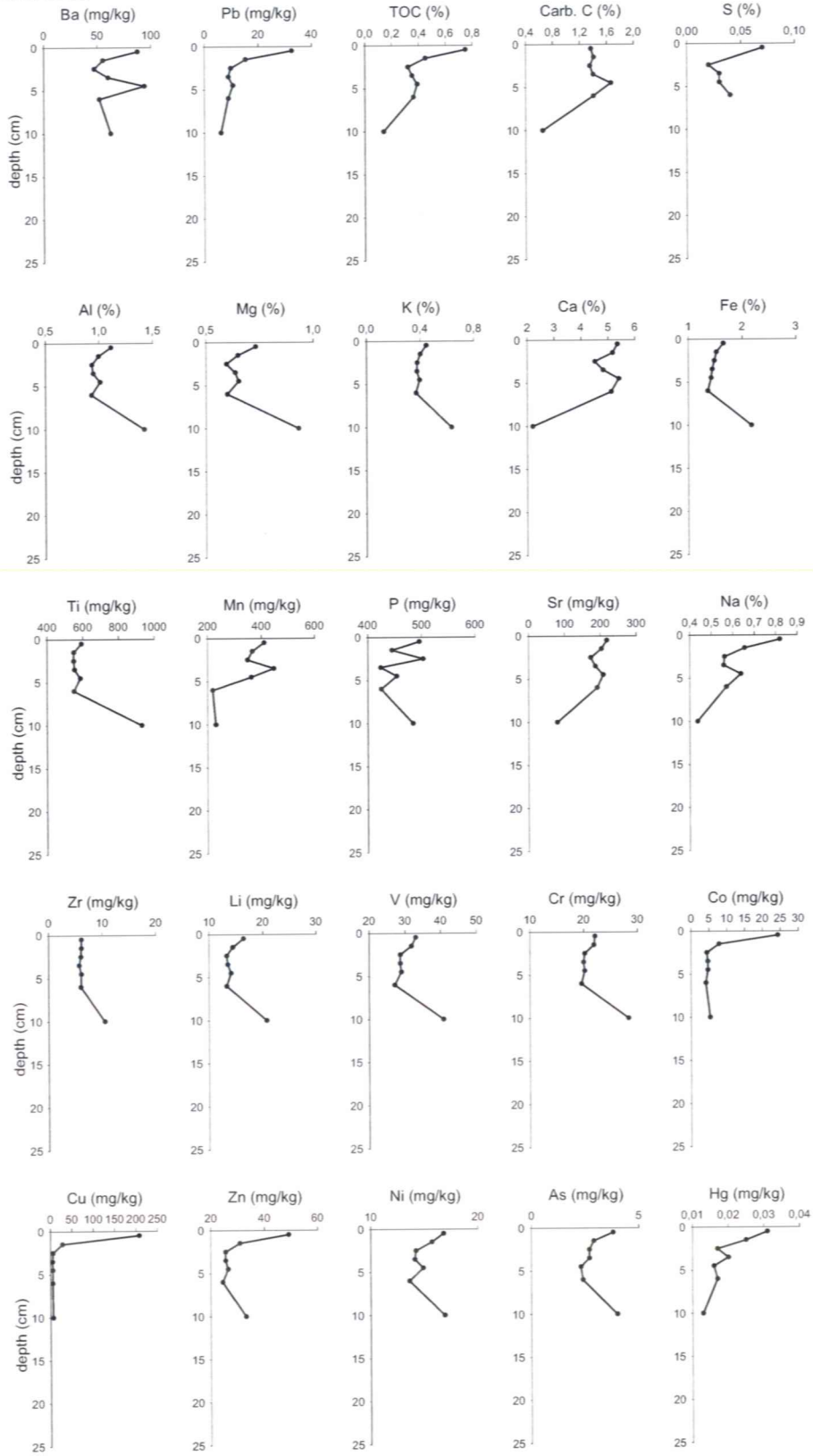
Ba (mg/kg)
Pb (mg/kg)
TOC (%)
Carb. C (%)
S (%)
Al (%)
Mg (%)
K (%)
Ca (%)
Fe (%)
Ti (mg/kg)
Mn (mg/kg)
P (mg/kg)
Sr (mg/kg)
Na (%)
Zr (mg/kg)
Li (mg/kg)
V (mg/kg)
Cr (mg/kg)
Co (mg/kg)
Cu (mg/kg)
Zn (mg/kg)
Ni (mg/kg)
As (mg/kg)
Hg (mg/kg)
depth (cm)

ST8; C035

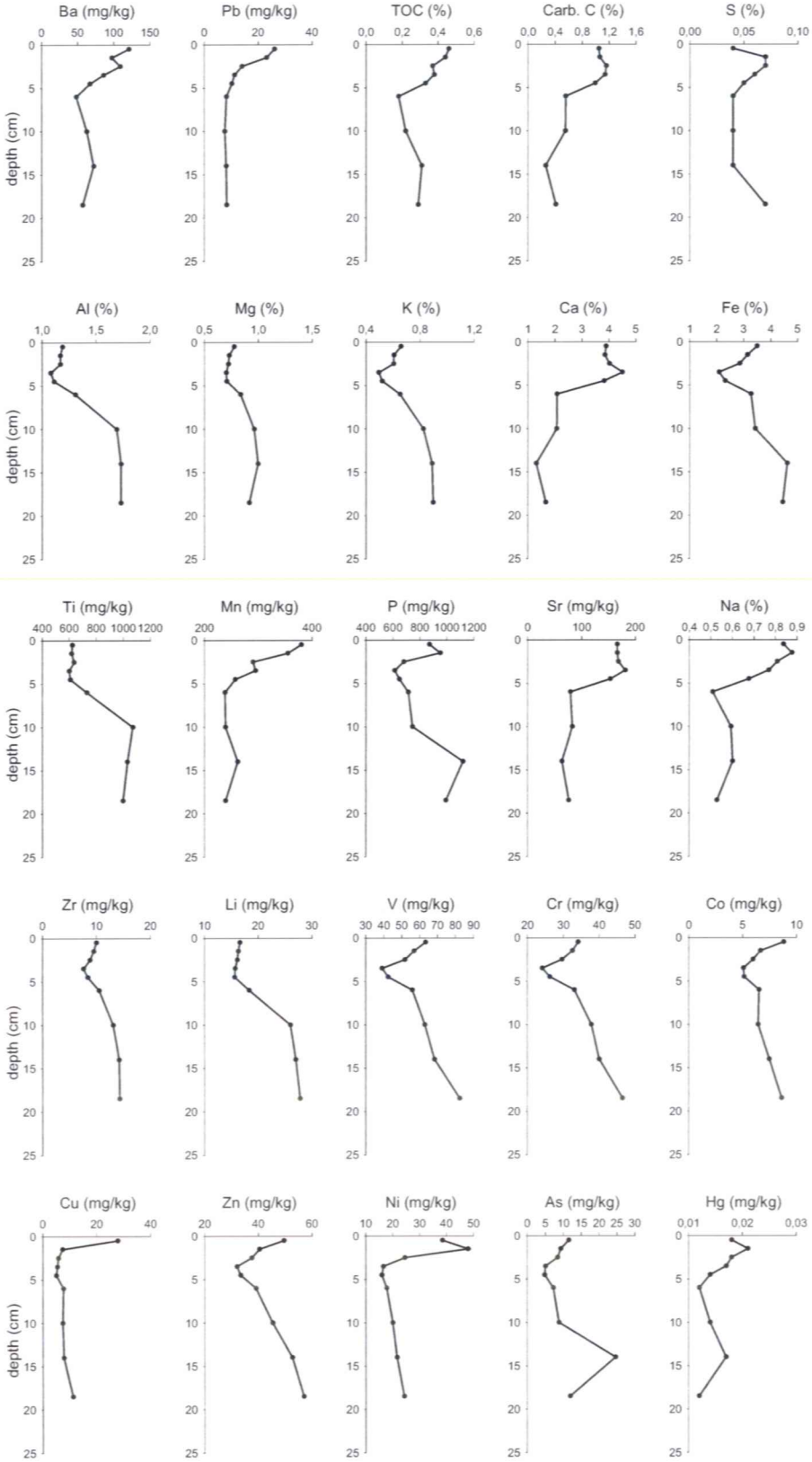
Ba (mg/kg)
Pb (mg/kg)
TOC (%)
Carb. C (%)
S (%)
Al (%)
Mg (%)
K (%)
Ca (%)
Fe (%)
Ti (mg/kg)
Mn (mg/kg)
P (mg/kg)
Sr (mg/kg)
Na (%)
Zr (mg/kg)
Li (mg/kg)
V (mg/kg)
Cr (mg/kg)
Co (mg/kg)
Cu (mg/kg)
Zn (mg/kg)
Ni (mg/kg)
As (mg/kg)
Hg (mg/kg)
depth (cm)

ST9; C041

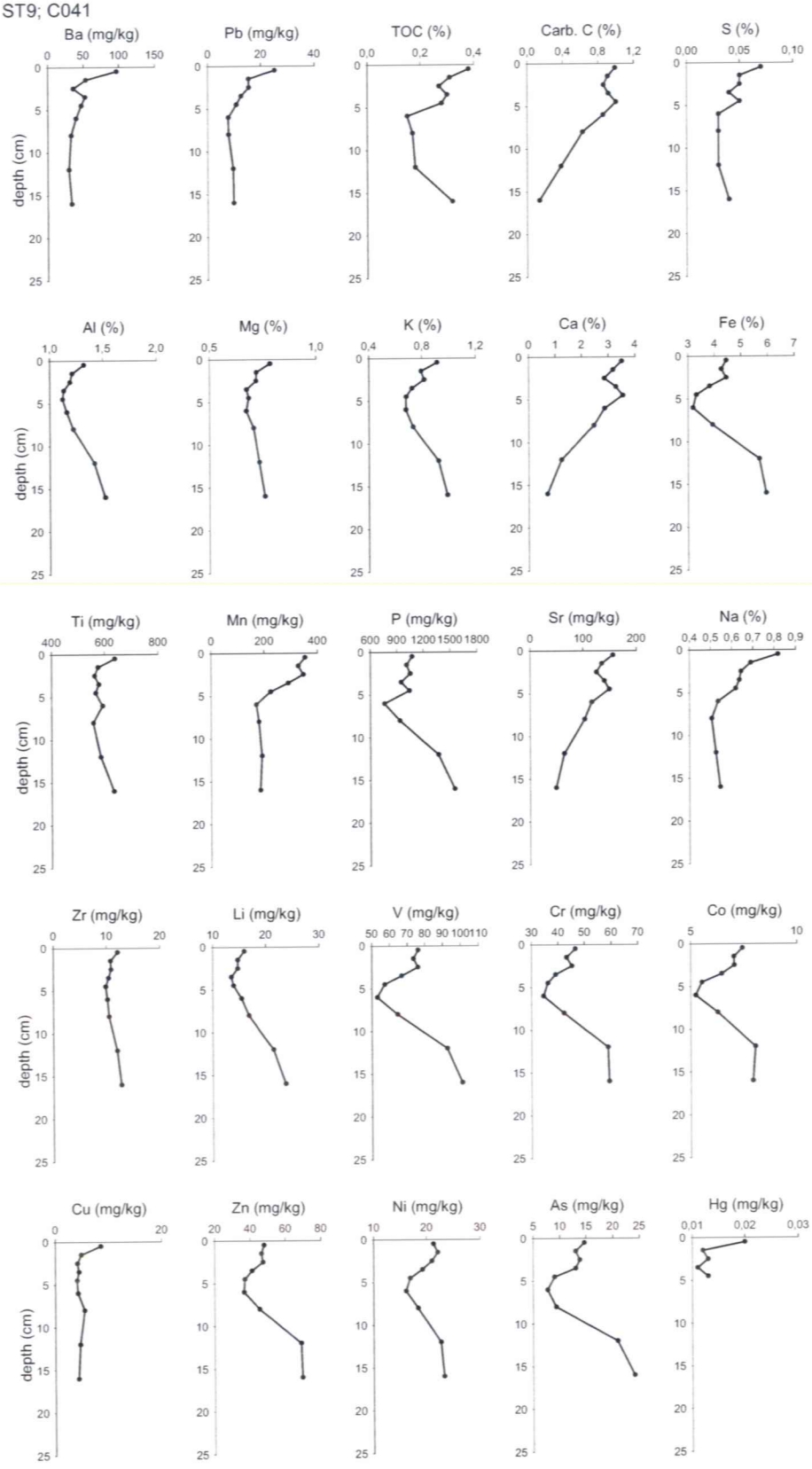
Ba (mg/kg)
Pb (mg/kg)
TOC (%)
Carb. C (%)
S (%)
Al (%)
Mg (%)
K (%)
Ca (%)
Fe (%)
Ti (mg/kg)
Mn (mg/kg)
P (mg/kg)
Sr (mg/kg)
Na (%)
Zr (mg/kg)
Li (mg/kg)
V (mg/kg)
Cr (mg/kg)
Co (mg/kg)
Cu (mg/kg)
Zn (mg/kg)
Ni (mg/kg)
As (mg/kg)
Hg (mg/kg)
depth (cm)

ST10; C046

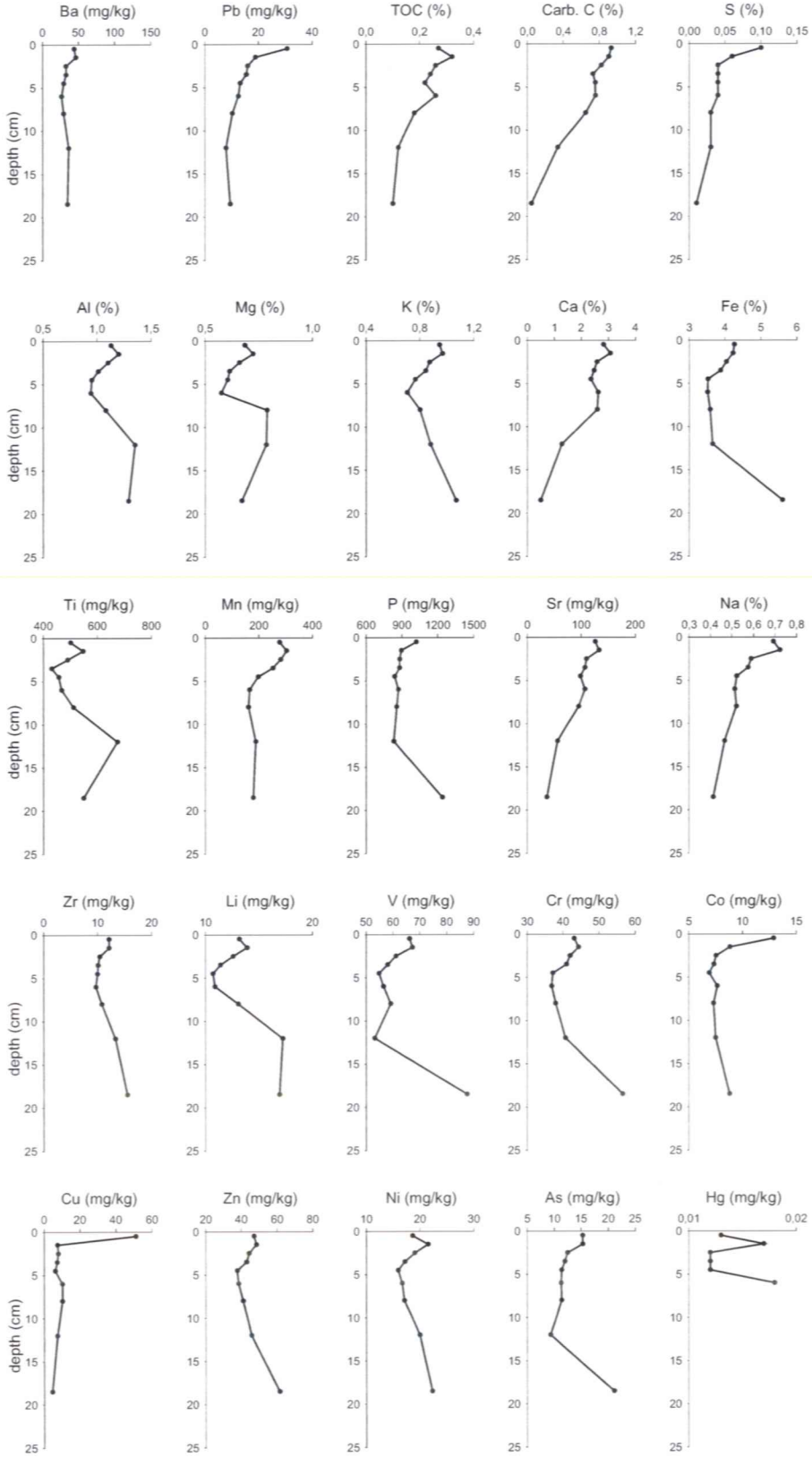
Ba (mg/kg)
Pb (mg/kg)
TOC (%)
Carb. C (%)
S (%)
Al (%)
Mg (%)
K (%)
Ca (%)
Fe (%)
Ti (mg/kg)
Mn (mg/kg)
P (mg/kg)
Sr (mg/kg)
Na (%)
Zr (mg/kg)
Li (mg/kg)
V (mg/kg)
Cr (mg/kg)
Co (mg/kg)
Cu (mg/kg)
Zn (mg/kg)
Ni (mg/kg)
As (mg/kg)
Hg (mg/kg)
depth (cm)

ST11; C049

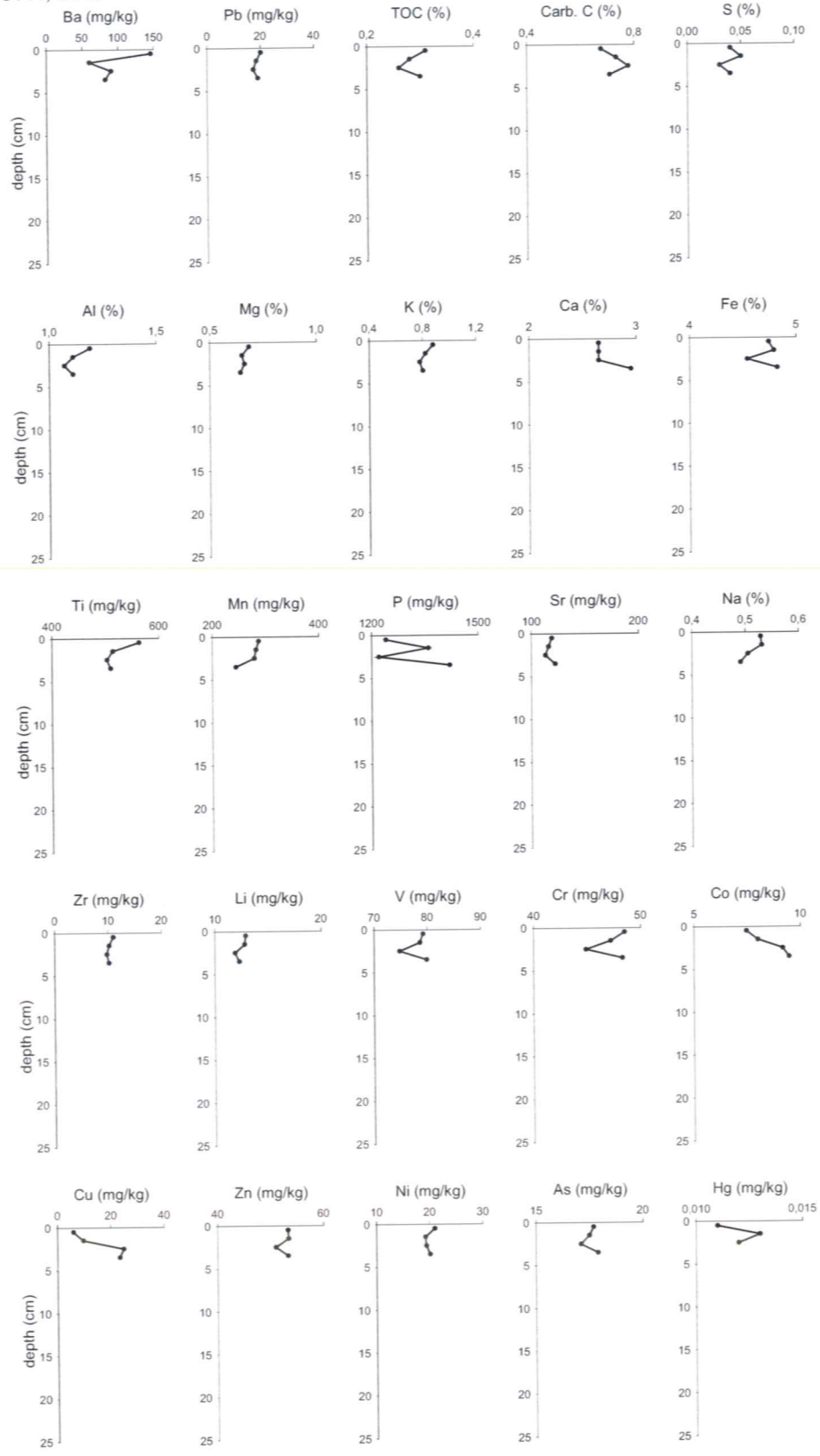
Ba (mg/kg)
Pb (mg/kg)
TOC (%)
Carb. C (%)
S (%)
Al (%)
Mg (%)
K (%)
Ca (%)
Fe (%)
Ti (mg/kg)
Mn (mg/kg)
P (mg/kg)
Sr (mg/kg)
Na (%)
Zr (mg/kg)
Li (mg/kg)
V (mg/kg)
Cr (mg/kg)
Co (mg/kg)
Cu (mg/kg)
Zn (mg/kg)
Ni (mg/kg)
As (mg/kg)
Hg (mg/kg)
depth (cm)

ST12; C056

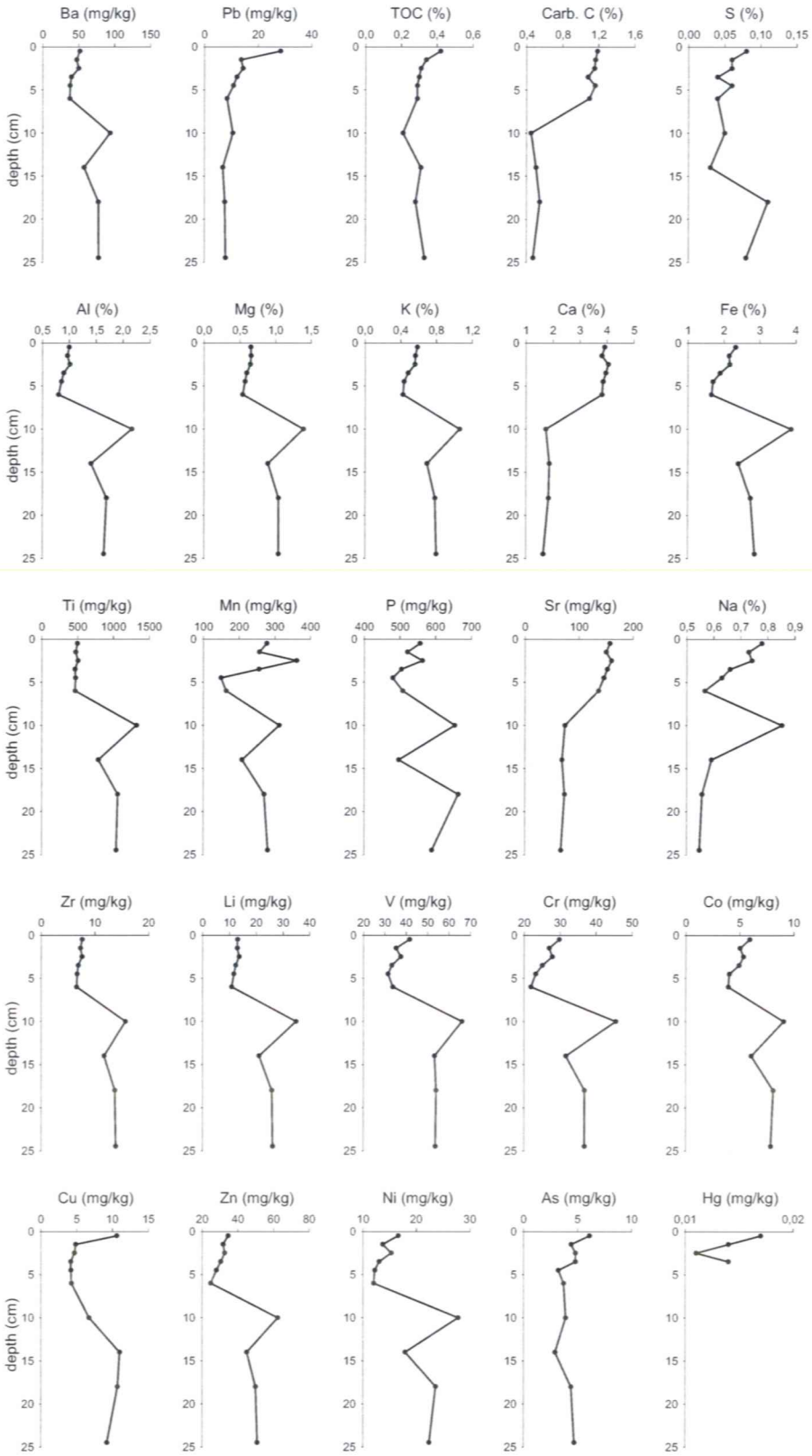
Ba (mg/kg)
Pb (mg/kg)
TOC (%)
Carb. C (%)
S (%)
Al (%)
Mg (%)
K (%)
Ca (%)
Fe (%)
Ti (mg/kg)
Mn (mg/kg)
P (mg/kg)
Sr (mg/kg)
Na (%)
Zr (mg/kg)
Li (mg/kg)
V (mg/kg)
Cr (mg/kg)
Co (mg/kg)
Cu (mg/kg)
Zn (mg/kg)
Ni (mg/kg)
As (mg/kg)
Hg (mg/kg)
depth (cm)

ST13; C060

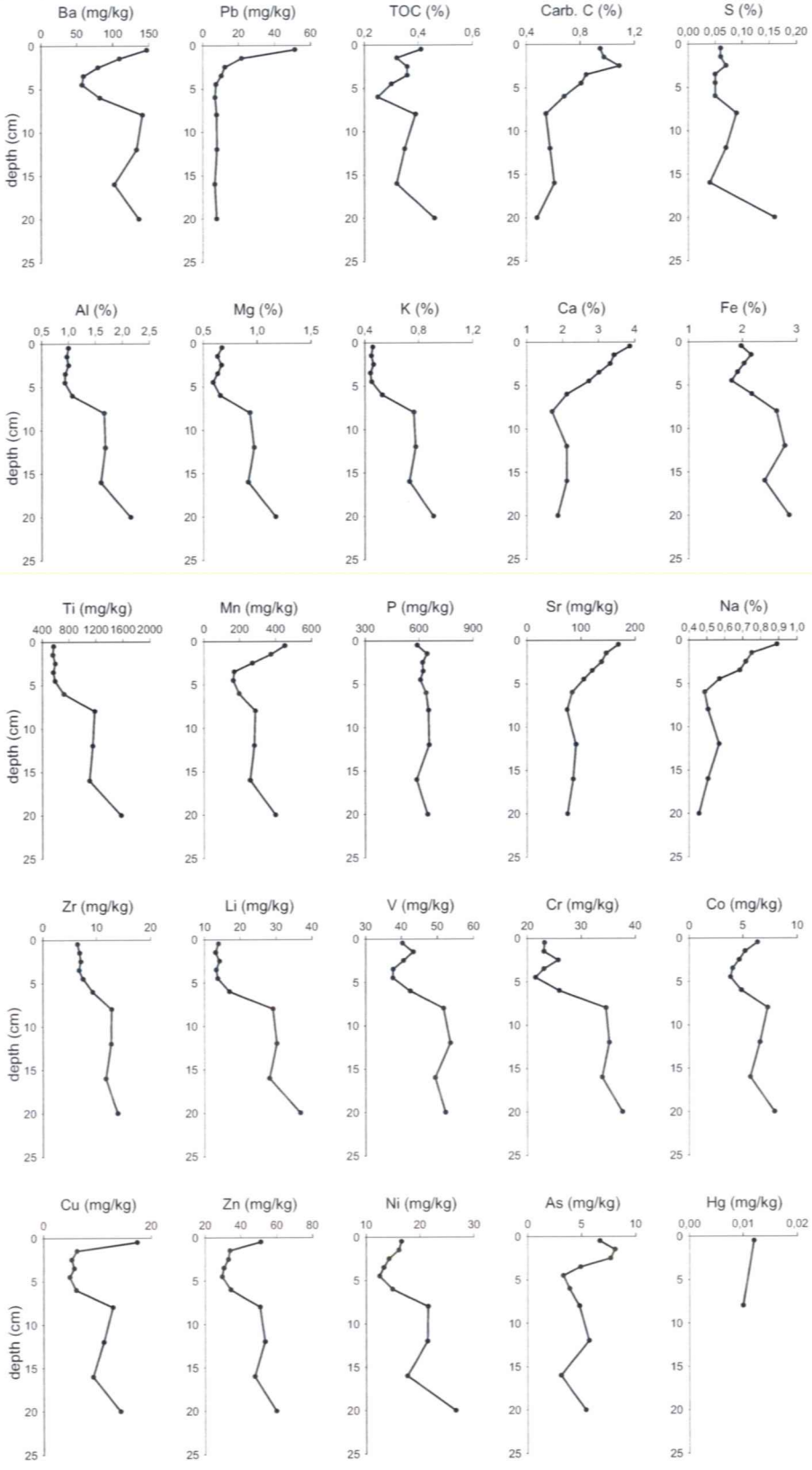
Ba (mg/kg)
Pb (mg/kg)
TOC (%)
Carb. C (%)
S (%)
Al (%)
Mg (%)
K (%)
Ca (%)
Fe (%)
Ti (mg/kg)
Mn (mg/kg)
P (mg/kg)
Sr (mg/kg)
Na (%)
Zr (mg/kg)
Li (mg/kg)
V (mg/kg)
Cr (mg/kg)
Co (mg/kg)
Cu (mg/kg)
Zn (mg/kg)
Ni (mg/kg)
As (mg/kg)
Hg (mg/kg)
depth (cm)

ST14; C064

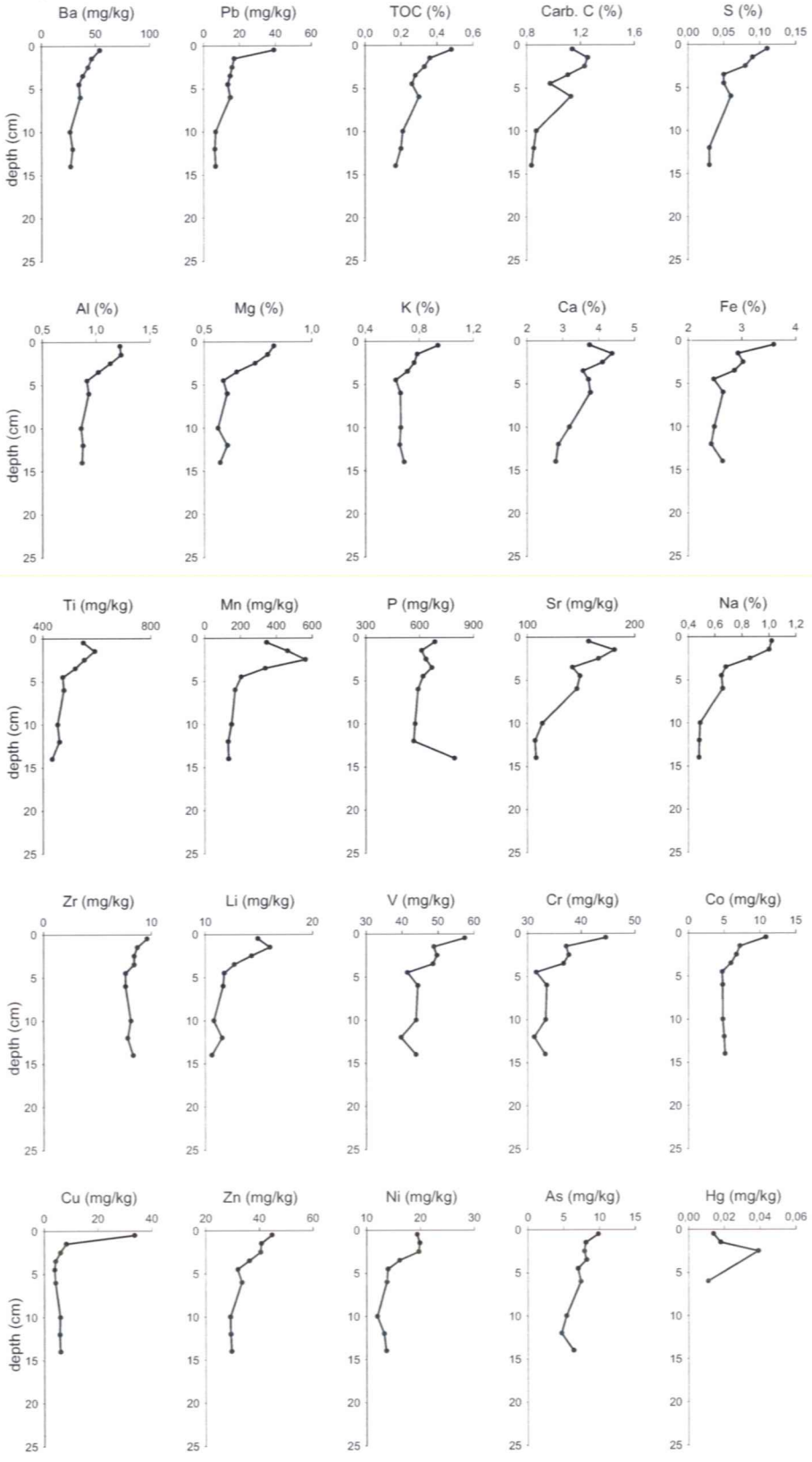
Ba (mg/kg)
Pb (mg/kg)
TOC (%)
Carb. C (%)
S (%)
Al (%)
Mg (%)
K (%)
Ca (%)
Fe (%)
Ti (mg/kg)
Mn (mg/kg)
P (mg/kg)
Sr (mg/kg)
Na (%)
Zr (mg/kg)
Li (mg/kg)
V (mg/kg)
Cr (mg/kg)
Co (mg/kg)
Cu (mg/kg)
Zn (mg/kg)
Ni (mg/kg)
As (mg/kg)
Hg (mg/kg)
depth (cm)

ST15; C069

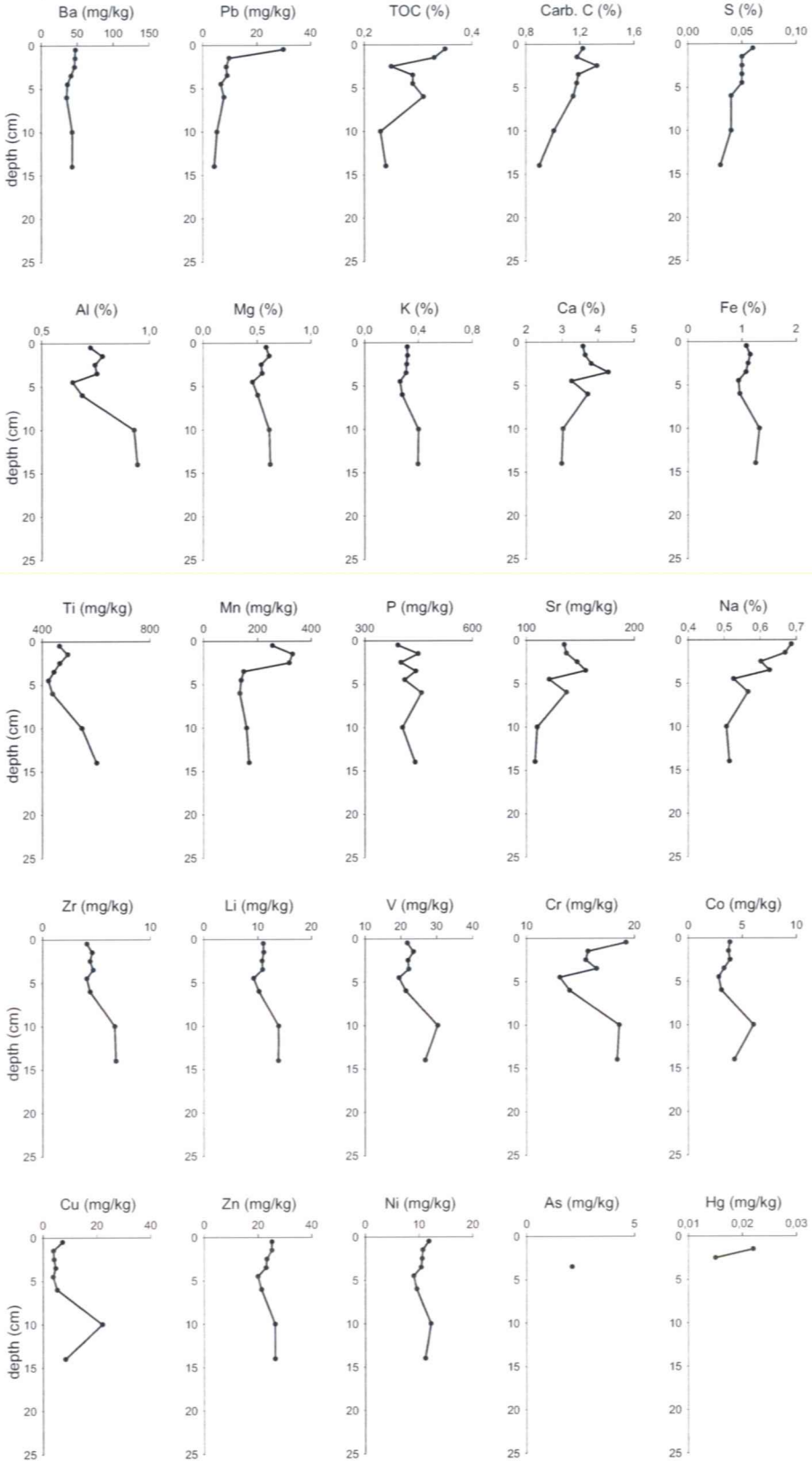
Ba (mg/kg)
Pb (mg/kg)
TOC (%)
Carb. C (%)
S (%)
Al (%)
Mg (%)
K (%)
Ca (%)
Fe (%)
Ti (mg/kg)
Mn (mg/kg)
P (mg/kg)
Sr (mg/kg)
Na (%)
Zr (mg/kg)
Li (mg/kg)
V (mg/kg)
Cr (mg/kg)
Co (mg/kg)
Cu (mg/kg)
Zn (mg/kg)
Ni (mg/kg)
As (mg/kg)
Hg (mg/kg)
depth (cm)

ST16; C074

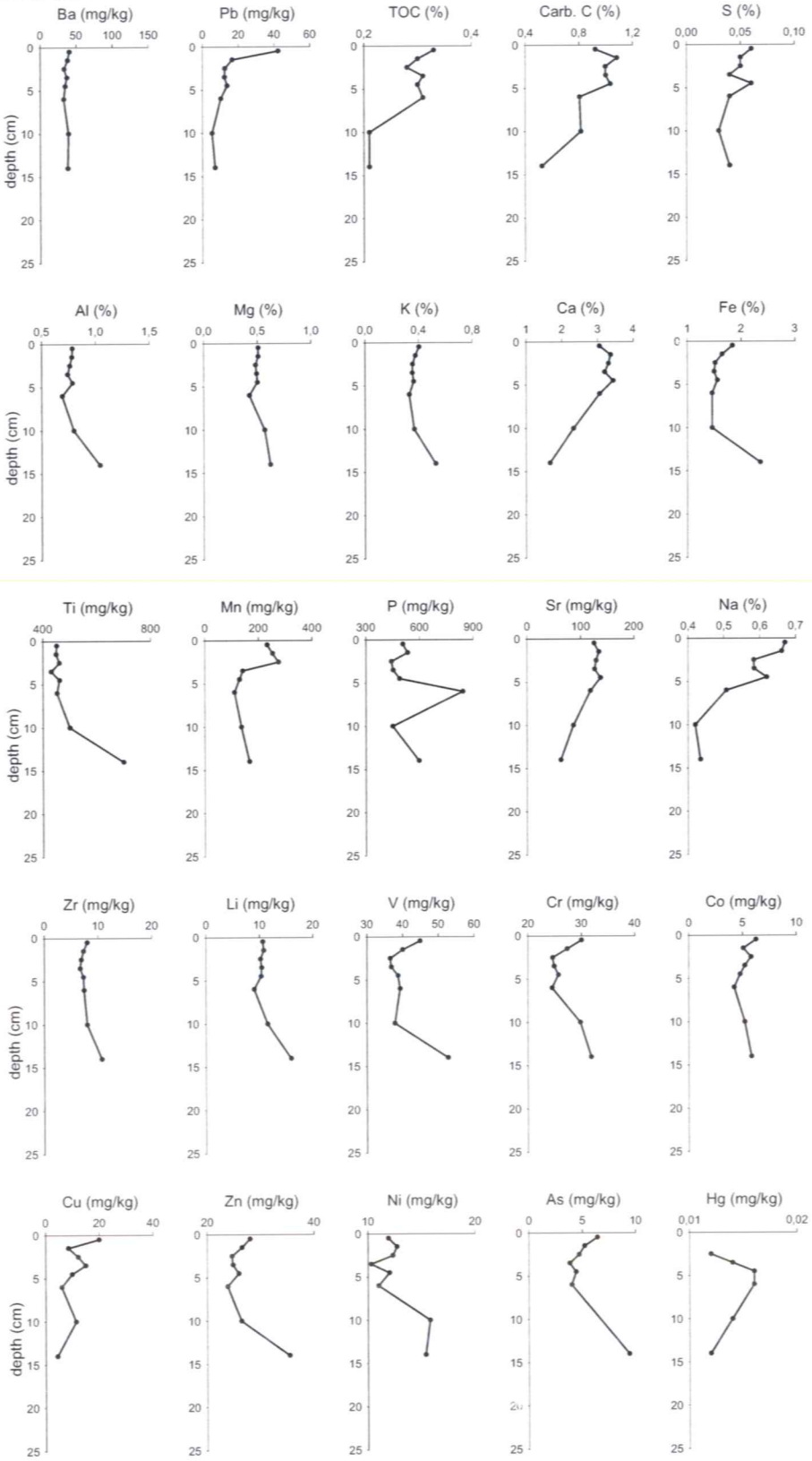
Ba (mg/kg)
Pb (mg/kg)
TOC (%)
Carb. C (%)
S (%)
Al (%)
Mg (%)
K (%)
Ca (%)
Fe (%)
Ti (mg/kg)
Mn (mg/kg)
P (mg/kg)
Sr (mg/kg)
Na (%)
Zr (mg/kg)
Li (mg/kg)
V (mg/kg)
Cr (mg/kg)
Co (mg/kg)
Cu (mg/kg)
Zn (mg/kg)
Ni (mg/kg)
As (mg/kg)
Hg (mg/kg)
depth (cm)

St17; C079

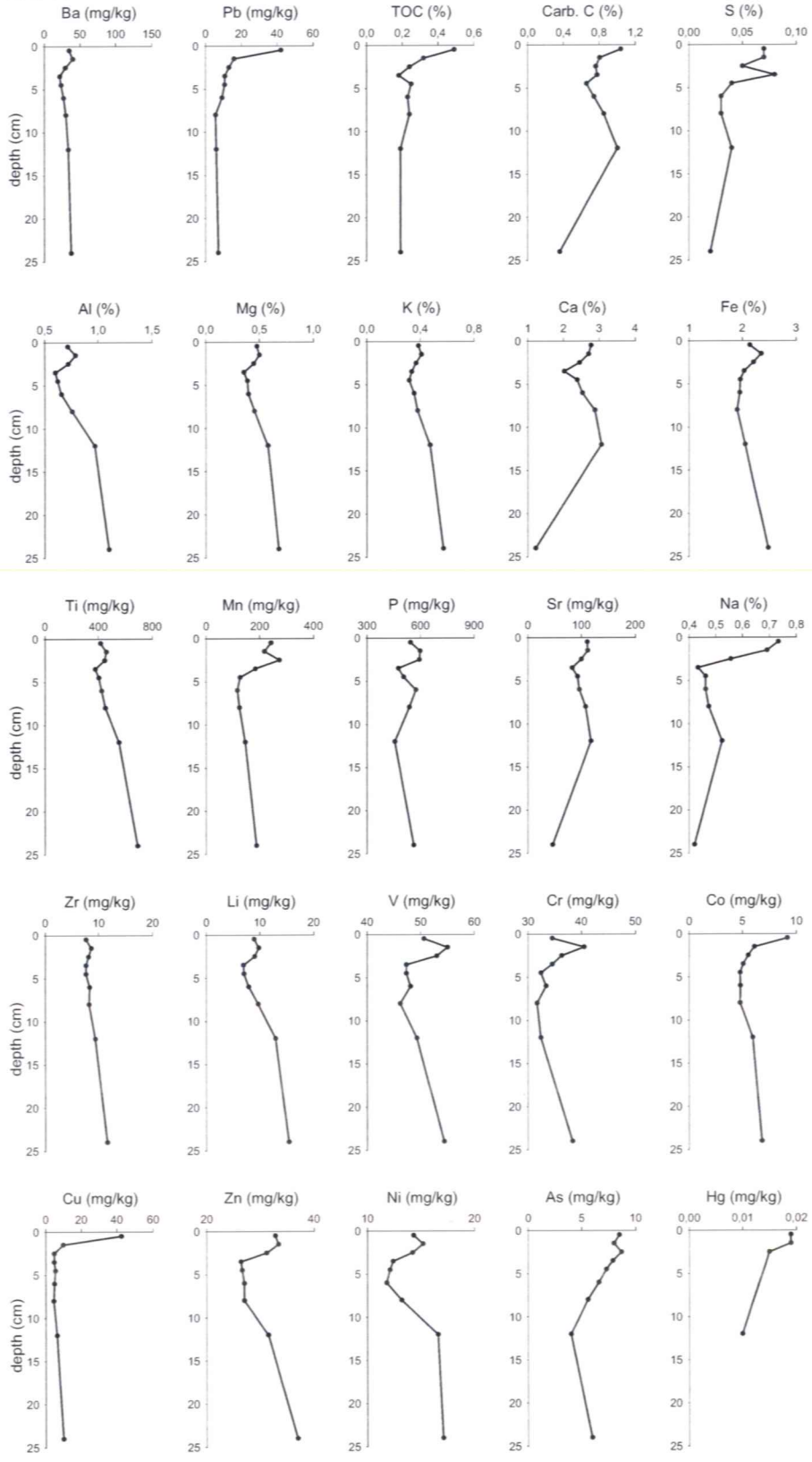
Ba (mg/kg)
Pb (mg/kg)
TOC (%)
Carb. C (%)
S (%)
Al (%)
Mg (%)
K (%)
Ca (%)
Fe (%)
Ti (mg/kg)
Mn (mg/kg)
P (mg/kg)
Sr (mg/kg)
Na (%)
Zr (mg/kg)
Li (mg/kg)
V (mg/kg)
Cr (mg/kg)
Co (mg/kg)
Cu (mg/kg)
Zn (mg/kg)
Ni (mg/kg)
As (mg/kg)
Hg (mg/kg)
depth (cm)

ST18; C084

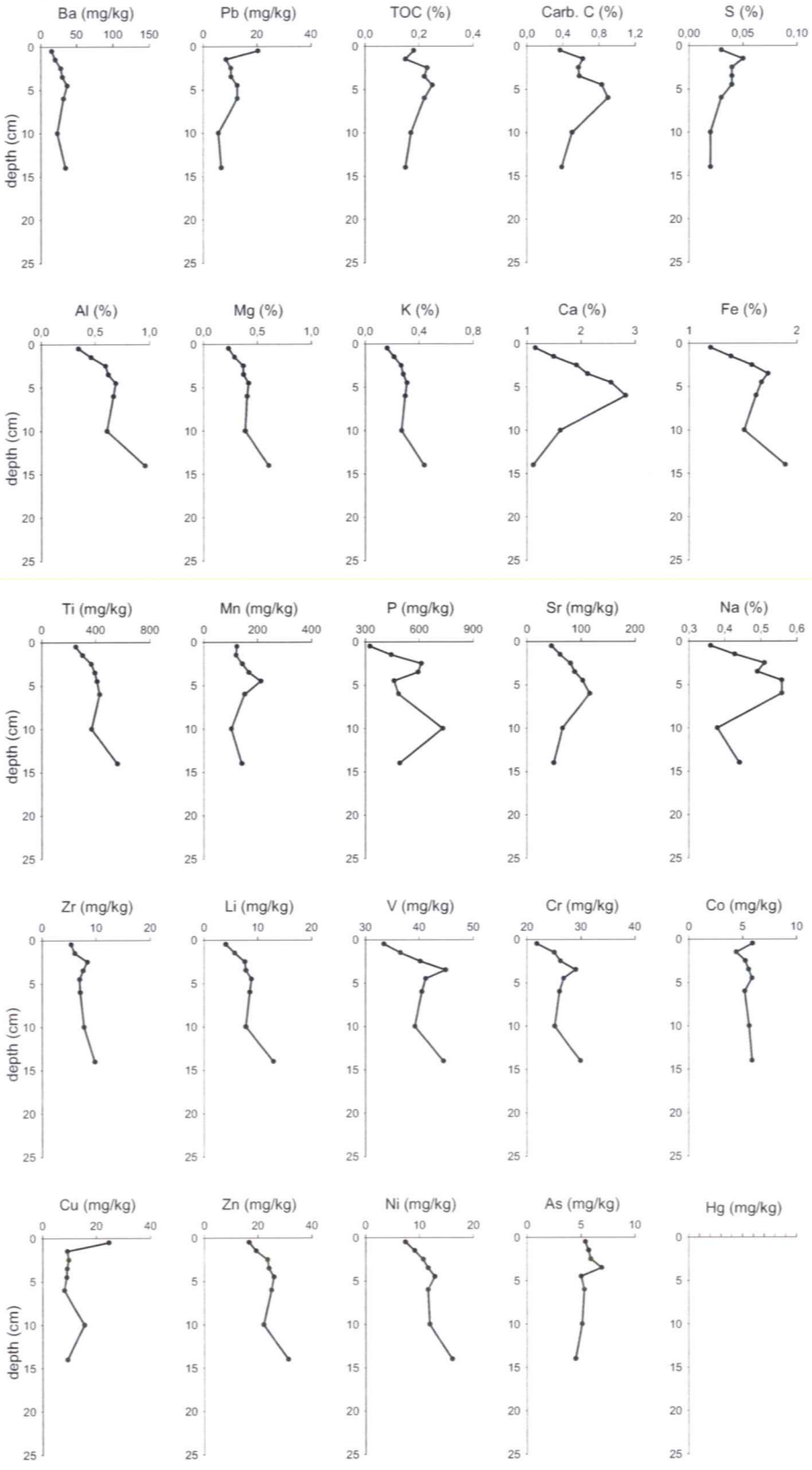
Ba (mg/kg)
Pb (mg/kg)
TOC (%)
Carb. C (%)
S (%)
Al (%)
Mg (%)
K (%)
Ca (%)
Fe (%)
Ti (mg/kg)
Mn (mg/kg)
P (mg/kg)
Sr (mg/kg)
Na (%)
Zr (mg/kg)
Li (mg/kg)
V (mg/kg)
Cr (mg/kg)
Co (mg/kg)
Cu (mg/kg)
Zn (mg/kg)
Ni (mg/kg)
As (mg/kg)
Hg (mg/kg)
depth (cm)

ST19; C086

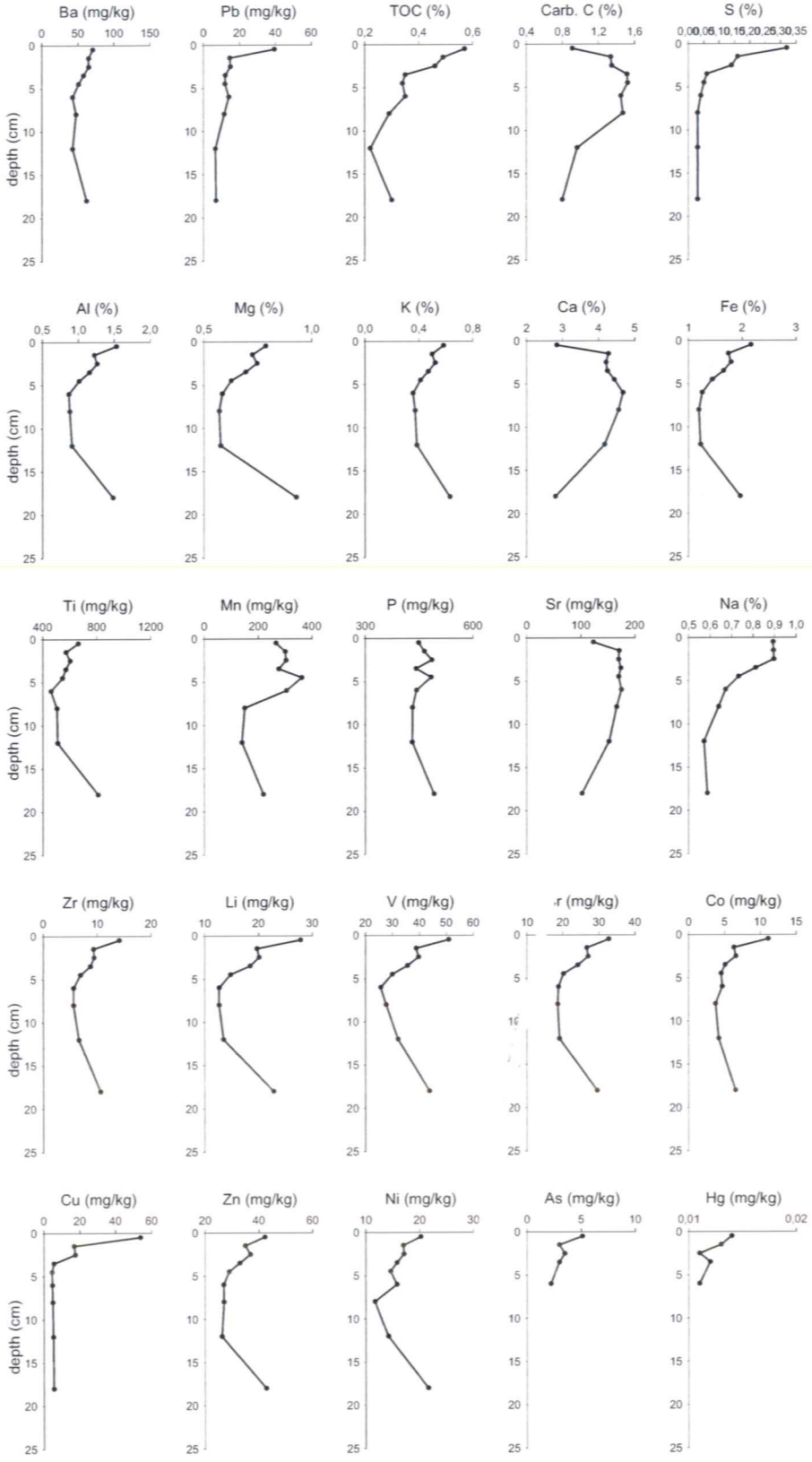
Ba (mg/kg)
Pb (mg/kg)
TOC (%)
Carb. C (%)
S (%)
Al (%)
Mg (%)
K (%)
Ca (%)
Fe (%)
Ti (mg/kg)
Mn (mg/kg)
P (mg/kg)
Sr (mg/kg)
Na (%)
Zr (mg/kg)
Li (mg/kg)
V (mg/kg)
Co (mg/kg)
Cu (mg/kg)
Zn (mg/kg)
Ni (mg/kg)
As (mg/kg)
Hg (mg/kg)
depth (cm)

ST20; C092

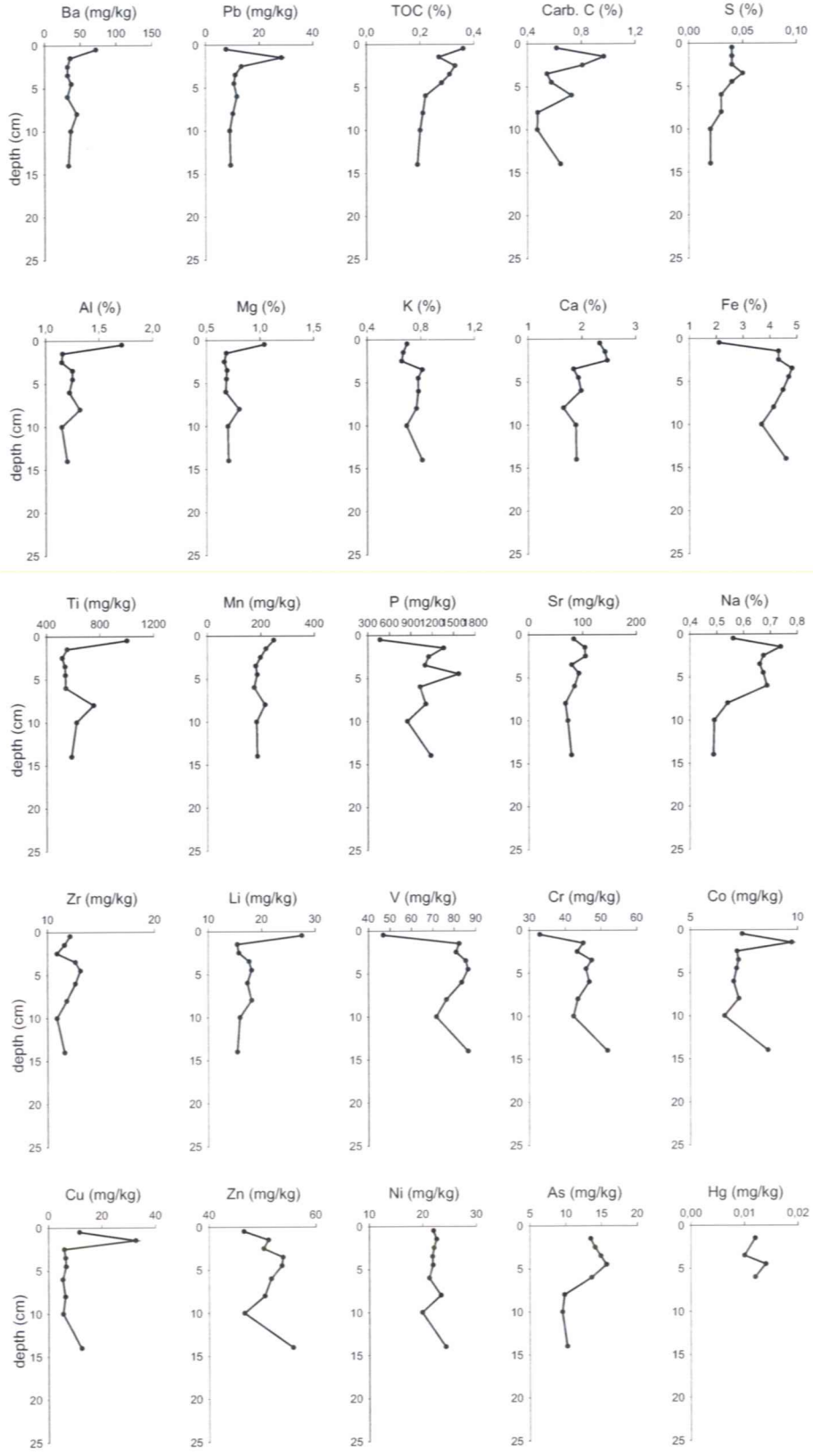
Ba (mg/kg)
Pb (mg/kg)
TOC (%)
Carb. C (%)
S (%)
Al (%)
Mg (%)
K (%)
Ca (%)
Fe (%)
Ti (mg/kg)
Mn (mg/kg)
P (mg/kg)
Sr (mg/kg)
Na (%)
Zr (mg/kg)
Li (mg/kg)
V (mg/kg)
Cr (mg/kg)
Co (mg/kg)
Cu (mg/kg)
Zn (mg/kg)
Ni (mg/kg)
As (mg/kg)
Hg (mg/kg)
depth (cm)

Retur: Havforskningsinstituttet v/ Informasjonen, Pb. 1870 Nordnes, NO-5817 Bergen

HAVFORSKNINGSINSTITUTTET
Institute of Marine Research
Nordnesgaten 50 - P.O. Box 1870 Nordnes
NO-5817 Bergen - Norway
Tel: +47 55 23 85 00 - Fax: +47 55 23 85 31

HAVFORSKNINGSINSTITUTTET
Sykehusveien 23, Postboks 6404
NO-9294 Tromsø - Norway
Tel: +47 55 23 85 00 - Fax: +47 77 60 97 01

HAVFORSKNINGSINSTITUTTET
NO-4817 His - Norway
Tel: +47 37 05 90 00 - Fax: +47 37 05 90 01

HAVFORSKNINGSINSTITUTTET
NO-5392 Storebø - Norway
Tel: +47 55 23 85 00 - Fax: +47 56 18 22 22

HAVFORSKNINGSINSTITUTTET
NO-5984 Matredal - Norway
Tel: +47 55 23 85 00 - Fax: +47 56 36 75 85

REDERIAVDELINGEN
Research Vessels Department
Tel: +47 55 23 85 00 - Fax: +47 55 23 85 32

INFORMASJONEN
Information
Tel: +47 55 23 85 00 - Fax: +47 55 23 85 55
E-mail: informasjonen@imr.no

www.imr.no

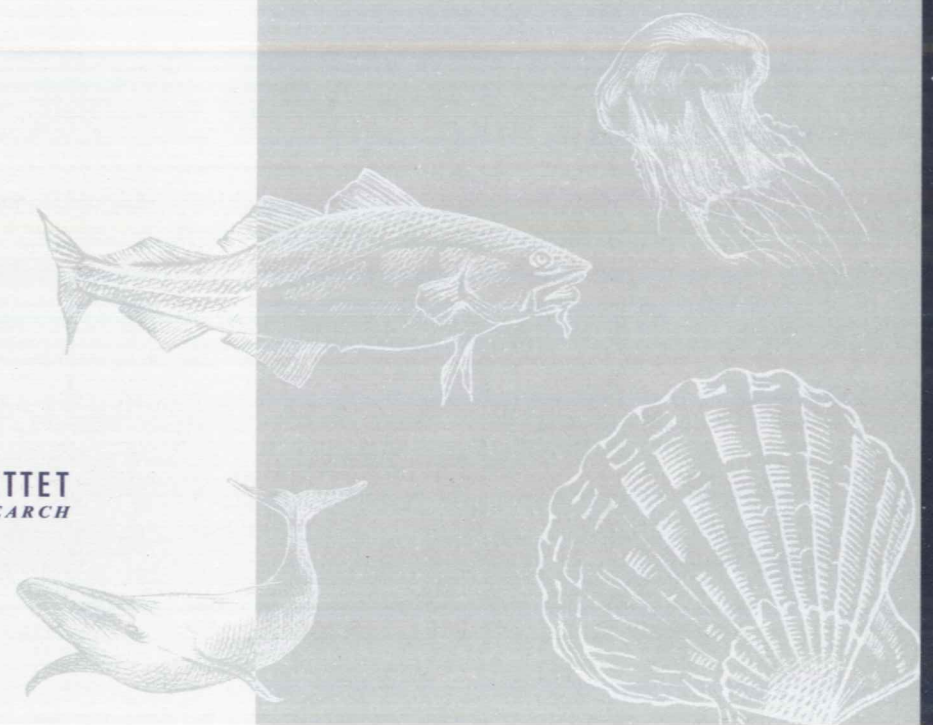

HAVFORSKNINGSINSTITUTTET
INSTITUTE OF MARINE RESEARCH